

This electronic thesis or dissertation has been downloaded from the King's Research Portal at <https://kclpure.kcl.ac.uk/portal/>



Accelerating Multi-Dimensional Magnetic Resonance Imaging of Blood Flow and Turbulence in the Cardiovascular System

Santelli, Claudio

Awarding institution:
King's College London

The copyright of this thesis rests with the author and no quotation from it or information derived from it may be published without proper acknowledgement.

END USER LICENCE AGREEMENT



Unless another licence is stated on the immediately following page this work is licensed

under a Creative Commons Attribution-NonCommercial-NoDerivatives 4.0 International

licence. <https://creativecommons.org/licenses/by-nc-nd/4.0/>

You are free to copy, distribute and transmit the work

Under the following conditions:

- Attribution: You must attribute the work in the manner specified by the author (but not in any way that suggests that they endorse you or your use of the work).
- Non Commercial: You may not use this work for commercial purposes.
- No Derivative Works - You may not alter, transform, or build upon this work.

Any of these conditions can be waived if you receive permission from the author. Your fair dealings and other rights are in no way affected by the above.

Take down policy

If you believe that this document breaches copyright please contact librarypure@kcl.ac.uk providing details, and we will remove access to the work immediately and investigate your claim.

Accelerating Multi-Dimensional Magnetic Resonance
Imaging of Blood Flow and Turbulence in the Cardiovascular
System

Claudio Santelli

A dissertation submitted for the degree of
Doctor of Philosophy
of the
University of London

Division of Imaging Sciences and Biomedical Engineering
King's College London, School of Medicine

Abstract

Disturbed hemodynamic conditions are often related to pathologies of the cardiovascular system. Phase-contrast Magnetic Resonance Imaging (MRI) provides a non-invasive technique for the assessment of time-resolved blood velocity vector fields within arbitrary imaging volumes. Besides velocity vector field information, parameters related to turbulence can be calculated with advanced multi-point velocity encoding schemes. However, long scan times are currently the main barrier for the acceptance of the method in a clinical setting.

The following work presents data-driven MRI reconstruction algorithms for undersampled measurements with the focus on accurate flow quantification and visualization.

An extension of an auto-calibrated parallel imaging reconstruction framework for arbitrary k -space trajectories is proposed. The exploitation of temporal correlations as present in time-resolved data demonstrates further advances of scan time reduction when assessing mean velocity and turbulent kinetic energy. While most prior knowledge imposed in advanced MR image reconstruction is designed to work on magnitude images or assumes smooth background phase behavior, dedicated provisions are required for image reconstruction of phase-contrast MRI data. To this end, it is proposed to incorporate the divergence-free condition of blood flow into a separate magnitude and phase reconstruction framework for improving the accuracy of image reconstruction of blood velocity vector fields. To address respiratory motion artifacts, retrospective non-rigid respiratory motion correction incorporated into an iterative parallel imaging reconstruction algorithm is proposed. Furthermore, optimized k - t sampling patterns are derived for combined parallel imaging- and compressed sensing-based scan acceleration. Finally, the dynamic parallel imaging technique is applied to study blood flow and turbulence patterns in a relevant patient population with congenital heart disease.

Keywords: Magnetic Resonance Imaging, blood flow, multi-point phase-contrast, turbulent kinetic energy, auto-calibration, parallel imaging, dynamic imaging, non-Cartesian sampling, motion correction, compressed sensing, phase regularization, vector field divergence

Acknowledgements

First of all, I would like to thank Sebastian Kozerke for picking me to do this PhD project in this exciting field of applied science, for his guidance and constant support during good and difficult times over the last four years.

I would like to thank Tobias Schaeffter for his expertise and support during my rather short time in London and for the nice welcome and start he provided me in his group.

I would like to thank Reza Razavi, Peter Boesiger and Klaas Pruessmann for giving me the opportunity to work in their outstanding divisions in London and Zurich, respectively.

I am grateful to Prof. M. Stuber and Prof. J. Wild for having agreed to review and examine this thesis.

Thank you to the following people I met and have worked with at the IBT's MR group in Zurich: Verena for smoothly introducing me to the art of pulse programming and measuring, Johannes for your recon and unofficial IT expertise, Kilian for your authority in the cardio office, Christian S. for being the only constant in the cardio office, Lukas for your chewing gums and copy card and Rudi for your every-day smile when I was passing by your office. Thanks to Christian B., Julia, Robert V., Carolin, Robert M., Tobi, Max H., Andreas, Berti, Georg, Max F., Patrick, Vlad, Dian, Adrian and Martin G. for their contributions to the nice working environment at the IBT. Thanks a lot to Martin B. and Gérard for your open door and cost-free software tools. Thanks to Bruno for fixing my laptop twice. Thanks Jan for becoming one of the very few reasonable citizens of Zurich supporting the first club in town. Thank you Georgios, Matteo and Benjamin for our formative trip in Australia.

Thanks to my friends and colleagues Daniel, Constantin, James, Andy, Jack, Markus, Ghislain, Christian, Claudia, Christoph and Usman I could work with at KCL in the heart of London.

I would like to thank Michael from the University of Wisconsin-Madison for his great contribution to our joint project.

Thank you Lea for being by my side, your unconditional support, your patience, your smile and your love.

Grösste Dankbarkeit empfinde ich gegenüber meiner Familie, insbesondere gegenüber meinen Eltern – Danke für eure bedingungslose Unterstützung und Liebe über all die Jahre.

Contents

Abstract	2
Acknowledgements	3
Chapter 1 Introduction.....	7
1.1 Motivation	8
1.2 Outline	9
1.3 Contribution of the Thesis.....	10
Chapter 2 MRI Basics.....	11
2.1 Nuclear Magnetic Resonance.....	11
2.1.1 Magnetization.....	11
2.1.2 Spin Dynamics.....	11
2.1.3 Spin Excitation – Producing Transverse Magnetization.....	13
2.2 Imaging	13
2.2.1 Spatial Encoding	14
2.2.2 Fourier Reconstruction.....	14
2.2.3 Radial Sampling	16
2.2.4 From Real- to Complex-Valued Signals	21
2.3 Flow Encoding.....	23
2.3.1 Fourier Velocity Encoding	24
2.3.2 Phase-Contrast MRI.....	25
2.3.3 Velocity-to-Noise Ratio.....	26
2.3.4 Concomitant Fields and Eddy Currents.....	27
Chapter 3 Image Reconstruction	31
3.1 Parallel Imaging	32
3.1.1 SENSE.....	32
3.1.2 GRAPPA.....	33

3.1.3	SPIRiT/ESPIRiT	35
3.2	Compressed Sensing	37
3.3	Dynamic Imaging	39
3.4	Motion	41
3.4.1	Affine Motion	41
3.4.2	Motion Compensation	41
3.4.3	Matrix Formalism for General Motion Model	43
Chapter 4	Radial k - t SPIRiT: Auto-Calibrated PI for Generalized PC MRI	45
4.1	Introduction	45
4.2	Theory	47
4.3	Methods.....	49
4.3.1	Data Acquisition	49
4.3.2	Image Reconstruction	50
4.3.3	Data Analysis.....	52
4.4	Results.....	53
4.5	Discussion	62
4.6	Appendix.....	64
Chapter 5	Accelerating 4D Flow MRI by Exploiting Vector Field Divergence Regularization	65
5.1	Introduction	65
5.2	Theory	66
5.2.1	Separate Magnitude and Phase Reconstruction	66
5.2.2	Phase Regularizers.....	67
5.2.3	Phase Difference Reconstruction Algorithms	68
5.3	Methods.....	70
5.3.1	Numerical Phantom.....	70
5.3.2	In Vivo Experiments.....	70
5.3.3	Image Reconstruction	71
5.3.4	Data Analysis.....	73

5.4	Results.....	74
5.5	Discussion	79
5.6	Appendix.....	84
5.6.1	Gradient and Hessian	84
5.6.2	Peak and Total Flow Bland-Altman Plots	85
Chapter 6	Optimized SPIRiT, Motion Correction and Sampling	89
6.1	Efficient SPIRiT Reconstruction	89
6.2	SPIRiT ^{mc} – Auto-Calibrating Parallel Imaging with Non-Rigid Motion Correction	93
6.3	Optimized <i>k-t</i> Sampling for Combined Parallel Imaging and Compressed Sensing	96
6.4	Discussion	100
Chapter 7	Radial 3D <i>k-t</i> SPIRiT Multi-Point PC MRI in CHD Patients	103
7.1	Introduction.....	103
7.2	Methods.....	104
7.2.1	Data Acquisition	104
7.2.2	Image Reconstruction	105
7.2.3	Flow Quantification	105
7.3	Results.....	106
7.4	Discussion	110
Chapter 8	Discussion and Outlook	114
	Bibliography	117
	List of Publications	128
	Curriculum Vitae	131

Chapter 1

Introduction

The heart supplies the body and itself with blood carrying oxygen and nutrients. The corresponding circulation during a cardiac cycle is illustrated in (Figure 1.1). Cardiovascular diseases (CVDs) are the major causes of death and disability worldwide and collectively describe pathological function of heart, brain vasculature and blood vessels [1]. The development of CVDs is often related to structural changes of the heart or vasculature altering blood flow dynamics which in turn can advance pathologies and/or increase the workload of the heart. Complex wall shear stress patterns due to disturbed blood transport are assumed to regulate biochemical responses in vessel walls and can cause arterial remodeling and the formation of atherosclerotic plaques [2, 3]. The resulting narrowing of the vessel lumen further affects hemodynamic conditions. Plaque formation modulates aortic stiffness and retrograde flow channels, respectively, and increases the risk of an embolic stroke [4]. Pathological aortic valves can promote pronounced helical flow patterns, retrograde flow jets and are associated with the formation of ascending aorta aneurysms [5]. Heart muscle pathologies lead to altered vortex patterns in the ventricles thereby reducing the efficiency of blood flow redirection (e.g. within the left ventricle from the left atrium through the aortic valve) [4]. These examples illustrate the importance of assessing parameters of cardiovascular fluid dynamics to serve diagnosis and therapy monitoring in CVDs.

Functional imaging modalities must provide tools to identify and quantify abnormal blood flow patterns related to the patient's pathogenesis, to guide, control and optimize corresponding therapies, surgical interventions or implant designs (e.g. stents, valve replacement). Echocardiography is a widespread imaging technique used in clinical routine for the assessment of 1D or 2D blood flow velocity fields. Besides its advantages of rapid planning, real-time visualization, good temporal resolution and low cost, ultrasound Doppler methods are inherently limited by acoustic access, spatial resolution, angle dependency of velocity quantification and operator dependency [6]. Flow in large vessels such as the aorta or pulmonary arteries can be assessed using transesophageal echocardiograms. Semi-quantitative information on blood

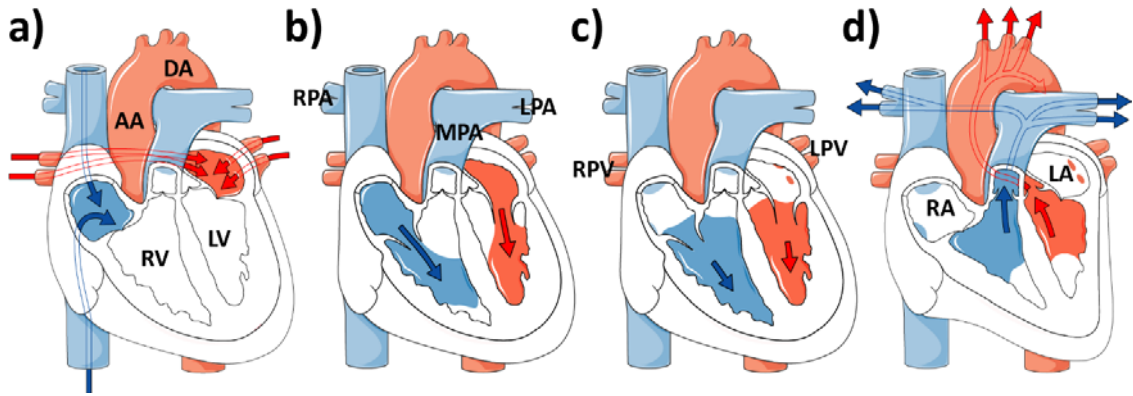


Figure 1.1 a) Venous or deoxygenated blood (blue) is collected in the right atrium (RA), while arterial or oxygenated blood (red) flows from the lungs through the right (RPVs) and left pulmonary veins (LPVs) into the left atrium (LA). b,c) With increasing pressure, the atrioventricular valves (tricuspid and mitral valve) are opened and blood is ejected into the right (RV) and left ventricle (LV). d) Due to muscle contraction, the displaced venous blood opens the semilunar valves (pulmonary and aortic valve) and is delivered to the lungs via main (MPA), right (RPA) and left pulmonary artery (LPA). Simultaneous LV contraction transports arterial blood through the aortic arch (composed of the ascending (AA) and descending aorta (DA)) where branching arteries distribute it throughout the body. This figure was produced using Servier Medical Art (www.servier.com, accessed 2014).

velocity patterns can also be obtained using invasive X-ray angiography procedures. Despite its high spatio-temporal resolution, flow quantification has several limitations [7].

1.1 Motivation

Phase-contrast (PC) MRI is a non-invasive imaging technique allowing for time-resolved multi-dimensional flow measurements in arbitrary positioned imaging volumes. Velocity component information along arbitrary directions is encoded into the signal phase [8]. Upon vector field calculation, complex flow patterns can be quantified using laws of fluid dynamics and illustrated with streamline or particle trace visualization [4]. Besides basic quantities such as flow volumes and rates, hemodynamic measures such as wall shear stress and relative pressure gradients can be derived [4].

Even though multi-dimensional PC MRI protocols are available on clinical scanners, widespread use in clinical routine has mainly been hampered by the long acquisition times. The assessment of 3D vector fields increases measurement time by at least a factor of four relative to a scan

protocol with the same imaging volume, spatial and temporal resolution, but without velocity encoding. For a standard 3D gradient-echo PC experiment with $3 \times 3 \times 3 \text{ mm}^3$ spatial and 50 ms temporal resolution, nominal scan time is on the order of one hour. Reduced data acquisition strategies in conjunction with reconstruction algorithms exploiting receiver coil weighting [9], spatio-temporal correlations [10] or transform-domain sparsity [11] have significantly decreased nominal scan times. However, the actual scan time is again increased by a factor of 2-3 due to free-breathing acquisitions employing respiratory gating. Acquiring multiple velocity encodes along a given direction increases the sensitivity to low and high velocities and enables the estimation of velocity distributions within each voxel. This concept of multi-point PC can be applied to quantify turbulent flow [12] which is not resolved by current PC vector field mapping. However, the gain in information about local flow distributions comes at the expense of further prolonged scan times. Velocity reconstruction accuracy may also be compromised by system imperfections, noise, misregistration effects between calibration and actual scan, residual motion, and inappropriate prior knowledge.

The objectives of this thesis are to accelerate multi-point PC MRI for velocity vector field and turbulence measurements and to develop corresponding acquisition protocols and reconstruction algorithms addressing the above limitations.

1.2 Outline

Chapter 2 gives an overview of the basic principles of MRI signal generation, spatial- and flow encoding, Fourier reconstruction and PC related correction methods.

In Chapter 3, the concept of image reconstruction formulated as an inverse problem is introduced. A review of parallel imaging (PI), compressed sensing (CS), dynamic imaging and motion-compensating methods is given.

A method for auto-calibrated PI exploiting temporal correlations in coil sensitivity weighting is introduced in Chapter 4. Measurements of mean velocity and turbulent kinetic energy (TKE) from highly undersampled radial multi-point PC data are presented.

Chapter 5 introduces novel algorithms directly incorporating physical prior knowledge about blood flow into the reconstruction from undersampled 3D PC data.

Motion correction combined with auto-calibrated PI is presented in Chapter 6 together with results from computationally accelerated image reconstruction. Optimized sampling patterns for dynamic imaging are also derived and validated.

The feasibility of the methodological developments in a relevant patient population with different congenital heart disease conditions is presented in Chapter 7.

1.3 Contribution of the Thesis

In this thesis, an undersampled radial multi-point PC acquisition scheme with auto-calibrated PI reconstruction is presented (Chapter 4). The approach is demonstrated to compare favourably with previous methods achieving up to 14-fold scan acceleration. Improved reconstruction accuracy is demonstrated for magnitude, phase and TKE maps by exploiting temporal correlations in signal space.

To correct for non-divergent velocity components in reconstructed velocity vector fields, a novel approach taking into account physical prior information on the divergence-free condition of incompressible fluids is proposed (Chapter 5). The concept is incorporated into a CS-based separate magnitude and phase reconstruction framework. Non-convex reconstruction algorithms regularizing phase difference maps using divergence-free Wavelets or finite difference-based divergence and curl operators are developed and compared to standard convex CS. Using reconstructions of dynamic 3D PC data, it is demonstrated that phase specific regularization efficiently reduces non-divergent field components and improves vector field visualization.

In Chapter 6, it is demonstrated that reconstruction times of iterative auto-calibrated reconstruction methods can be reduced by a factor between 1.5 to 2 using efficient mathematical formulations of the encoding and PI operators. Furthermore, data-driven non-rigid respiratory motion correction in conjunction with PI is presented for an effective combination of scan acceleration and time-efficient respiratory motion compensation. Moreover, optimized Cartesian undersampling patterns are derived for dynamic PI in combination with CS reconstruction.

A 3D variant of the auto-calibrated PI technique presented in Chapter 4 is implemented and applied to acquire prospectively undersampled radial multi-point PC data in a congenital heart disease patient cohort (Chapter 7). Reconstruction results and measurement times of around 15 minutes demonstrate the potential of concurrent velocity and turbulence mapping in a clinical setting.

Chapter 2

MRI Basics

2.1 Nuclear Magnetic Resonance

2.1.1 Magnetization

MR systems manipulate net magnetization aligned with a static magnetic field $\mathbf{B}_0 = B_0 \mathbf{e}_z$ along the z-direction $\mathbf{e}_z = (0,1,1)^T$ in a (x,y,z) coordinate system [13-17]. The measurable magnetization \mathbf{M} is defined as the macroscopic magnetic moment per unit volume resulting from the superimposing nuclear angular moments or spins $\boldsymbol{\mu}_i$: $\mathbf{M} = \sum_i \boldsymbol{\mu}_i$. For spin-1/2 isotopes (e.g. ^1H , ^{13}C or ^{31}P), quantum mechanics allows the magnetic moment's z-component to assume only two values/directions related to the magnetic quantum numbers $\pm 1/2$. In a magnetic field-free environment, the two quantum states are equally probable, and thus, add up to a zero magnetic moment. In the presence of \mathbf{B}_0 , the two quantum states are not energetically identical anymore and a net population of magnetic dipoles aligned with \mathbf{e}_z is produced. In the thermal equilibrium at spin temperature T_s , Boltzmann statistics approximates the net magnetization along z by

$$M_0 = \frac{n\gamma^2 \hbar^2 B_0}{4k_b T_s}, \quad (2.1)$$

with spin density n , gyromagnetic ratio γ , the Planck and Boltzmann constants \hbar and k_b , respectively.

2.1.2 Spin Dynamics

The dynamics of net-magnetization $\mathbf{M}(\mathbf{r},t)$ in a magnetic field $\mathbf{B}(\mathbf{r},t) = (B_x(\mathbf{r},t), B_y(\mathbf{r},t), B_0)^T$ at

position \mathbf{r} is described by classical physics laws using the Bloch equations:

$$\frac{d}{dt}\mathbf{M}(\mathbf{r},t) = \mathbf{M}(\mathbf{r},t) \times \gamma\mathbf{B}(\mathbf{r},t) - \begin{pmatrix} M_x(\mathbf{r},t)/T_2(\mathbf{r}) \\ M_y(\mathbf{r},t)/T_2(\mathbf{r}) \\ (M_z(\mathbf{r},t) - M_0(\mathbf{r}))/T_1(\mathbf{r}) \end{pmatrix}. \quad (2.2)$$

If $B_{x,y}(\mathbf{r},t) = 0$, the differential equations describe magnetization rotating around \mathbf{e}_z with Larmor frequency $\omega_0 = \gamma B_0$. Simultaneously, the longitudinal component M_z builds up to M_0 while transverse components $M_{x,y}$ decay with tissue dependent constants T_1 and T_2 , respectively. The relaxation time constants reflect spin-lattice and spin-spin interactions driving the spin ensembles back to thermal equilibrium state. A solution of (2.2) can be obtained by neglecting relaxation effects ($T_{1,2} \rightarrow +\infty$) yielding precessing magnetization (Figure 2.1a). Then, (2.2) is locally transformed into a coordinate system $(\hat{x}, \hat{y}, \hat{z} = z)$ rotating at position \mathbf{r} with ω_0 around \mathbf{e}_z leading to a new set of uncoupled differential equations,

$$\frac{d}{dt}\mathbf{M}(\mathbf{r},t)_{rot} = \begin{pmatrix} M_{\hat{x}}(\mathbf{r},t)/T_2(\mathbf{r}) \\ M_{\hat{y}}(\mathbf{r},t)/T_2(\mathbf{r}) \\ (M_{\hat{z}}(\mathbf{r},t) - M_0(\mathbf{r}))/T_1(\mathbf{r}) \end{pmatrix}, \quad (2.3)$$

with solutions $M_{\hat{x}}(\mathbf{r},t) = M_{\hat{x}}(\mathbf{r},0)\exp(-t/T_2(\mathbf{r}))$, $M_{\hat{y}}(\mathbf{r},t) = M_{\hat{y}}(\mathbf{r},0)\exp(-t/T_2(\mathbf{r}))$ and $M_{\hat{z}}(\mathbf{r},t) = (M_{\hat{z}}(\mathbf{r},0) - M_0(\mathbf{r}))\exp(-t/T_1(\mathbf{r})) + M_0(\mathbf{r})$.

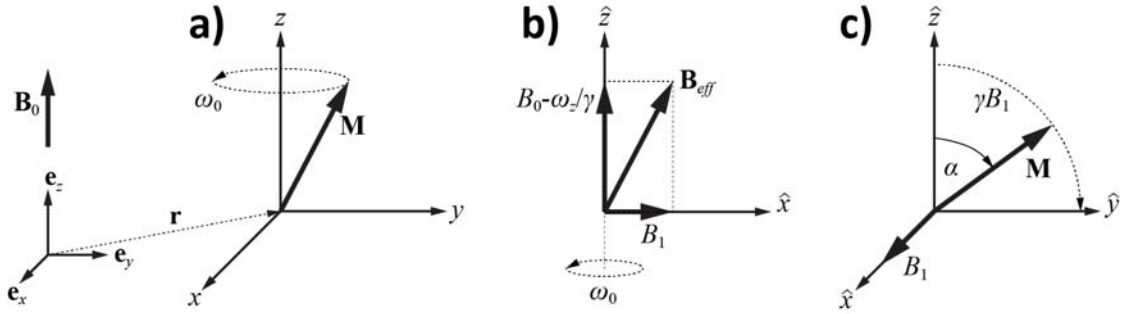


Figure 2.1 a) Precessing magnetization around the main magnetic field axis with angular velocity $\omega_0 = \gamma B_0$. b) Effective magnetization resulting from the superposition of the altered main field z-component and the RF field component in the rotating coordinate system. c) If the resonance condition ($\omega_z = \gamma B_0$) is met, transverse magnetization is built up by rotating \mathbf{M} around \mathbf{B}_1 with angular frequency γB_1 .

2.1.3 Spin Excitation – Producing Transverse Magnetization

Precessing transverse magnetization can be measured using the principle of Faraday induction, i.e. by detecting the induced voltage in a receiver coil tuned to the Larmor frequency. Transverse magnetization is generated by superimposing the main field \mathbf{B}_0 with a transverse radio-frequency (RF) field $\mathbf{B}_1(t) = (B_1(t), 0, 0)^T$ generated by a transmit coil-driven with a current oscillating at ω_z . The Bloch equations (neglecting relaxation effects) in the locally rotating frame ($\mathbf{e}_{\hat{x}}, \mathbf{e}_{\hat{y}}, \mathbf{e}_{\hat{z}} = \mathbf{e}_z$) then read

$$\begin{aligned} \frac{d}{dt} \mathbf{M}(\mathbf{r}, t)_{rot} &= \mathbf{M}(\mathbf{r}, t)_{rot} \times \gamma \left[\left(B_0 - \frac{\omega_z}{\gamma} \right) \mathbf{e}_{\hat{z}} + B_1(t) \mathbf{e}_{\hat{x}} \right] \\ &= \mathbf{M}(\mathbf{r}, t)_{rot} \times \gamma \mathbf{B}_{eff} \end{aligned} \quad (2.4)$$

describing precessing magnetization around \mathbf{B}_{eff} in the rotating frame (Figure 2.1b). Since $B_0 \gg B_1$, the z-component of \mathbf{B}_{eff} needs to disappear, i.e. the RF pulse needs to fulfil the resonance condition

$$\omega_z = \omega_0 = \gamma B_0. \quad (2.5)$$

Accordingly, magnetization is tipped around $\mathbf{e}_{\hat{x}}$ in the (\hat{y}, \hat{z}) -plane with the flip angle $\alpha(t) = \gamma \int_0^t B_1(\tau) d\tau$ (Figure 2.1c).

2.2 Imaging

Superimposing the main magnetic field with a gradient field $\mathbf{G}(t) = (G_x(t), G_y(t), G_z(t))^T$, $\mathbf{B}(\mathbf{r}, t) = (B_0 + \mathbf{G}(t) \cdot \mathbf{r}) \mathbf{e}_z$, enables spatially selective excitation and spatial encoding of the MR signal. The resonance condition of the RF pulse $\omega(\mathbf{r}) = \gamma(B_0 + \mathbf{G} \cdot \mathbf{r})$ becomes spatially dependent and, accordingly, a plane perpendicular to the gradient direction is excited.

Upon excitation, the initial transverse magnetization precessing with $\omega(\mathbf{r}, t) = \gamma(B_0 + \Delta B_0(\mathbf{r}) + \mathbf{G}(t) \cdot \mathbf{r})$ around the axis of the applied longitudinal field is denoted $\rho(\mathbf{r}) \equiv \rho(\mathbf{r}, t=0)$. The field map ΔB_0 incorporates deviations of the field strength from the nominal value B_0 . At time point $t > 0$, the rotating magnetization has accumulated a net phase of $\phi(\mathbf{r}, t) = \int_0^t \omega(\mathbf{r}, \tau) d\tau = \gamma \int_0^t B_z(\mathbf{r}, \tau) d\tau$. Consequently, the complex-valued signal $d(t)$ can be written as a superposition of the precessing magnetization from distinct infinitesimal small

compartments $d\mathbf{r}$ having accumulated a spatially dependent net phase:

$$d(t) = \int_V c(\mathbf{r}) \rho(\mathbf{r}) e^{-t/T_2^*(\mathbf{r})} e^{-i\phi(\mathbf{r},t)} d\mathbf{r} . \quad (2.6)$$

The excited volume is given as V , $c(\mathbf{r})$ denotes the complex receiver coil sensitivity, and $1/T_2^* = 1/T_2 + 1/T_{inhom}$ refers to the transverse relaxation time constant taking into account signal dephasing due to spin-spin interactions (T_2) and due to field inhomogeneities (T_{inhom}).

2.2.1 Spatial Encoding

Ignoring off-resonance (ΔB_0 , chemical shift, susceptibility variations) and relaxation terms, and by defining the spatial frequency vector

$$\mathbf{k}(t) = \gamma \int_0^t \mathbf{G}(\tau) d\tau , \quad (2.7)$$

a Fourier relation between acquired signal $d(\mathbf{k})$ and the sensitivity-weighted object $\rho(\mathbf{r})$ is obtained:

$$d(\mathbf{k}) = \int_V c(\mathbf{r}) \rho(\mathbf{r}) e^{-i\mathbf{k}\cdot\mathbf{r}} d\mathbf{r} . \quad (2.8)$$

The signal is now sampled in the so-called k-space by applying gradient waveforms. Figure 2.2 shows examples of standard 2D Cartesian gradient-echo (GRE) and spin-echo (SE) sequence. These sequences allow manipulation of the signal's echo time (TE), i.e. the time when $k_x = 0$ is traversed by prephasing gradients preceding the actual readout lobe on the frequency-encoding axis. The echo signal is generated by a readout gradient (GRE) reversing the direction of phase accumulation or a 180° RF refocusing pulse (SE) inverting the accumulated phase. While GRE is sensitive to off-resonance effects since phase is accumulated during the whole TE interval, SE employs 180° refocussing pulses rewinding field induced phases. Consequently, the echo signal is weighted by e^{-t/T_2^*} in GRE and by e^{-t/T_2} in SE sequences, respectively.

2.2.2 Fourier Reconstruction

By sampling the k-space signal at a finite number of positions \mathbf{k}_i , $i = 1, \dots, M$, a linear discretized version of (2.8) is obtained [18]:

$$\mathbf{d} = \mathbf{E}\rho , \quad (2.9)$$

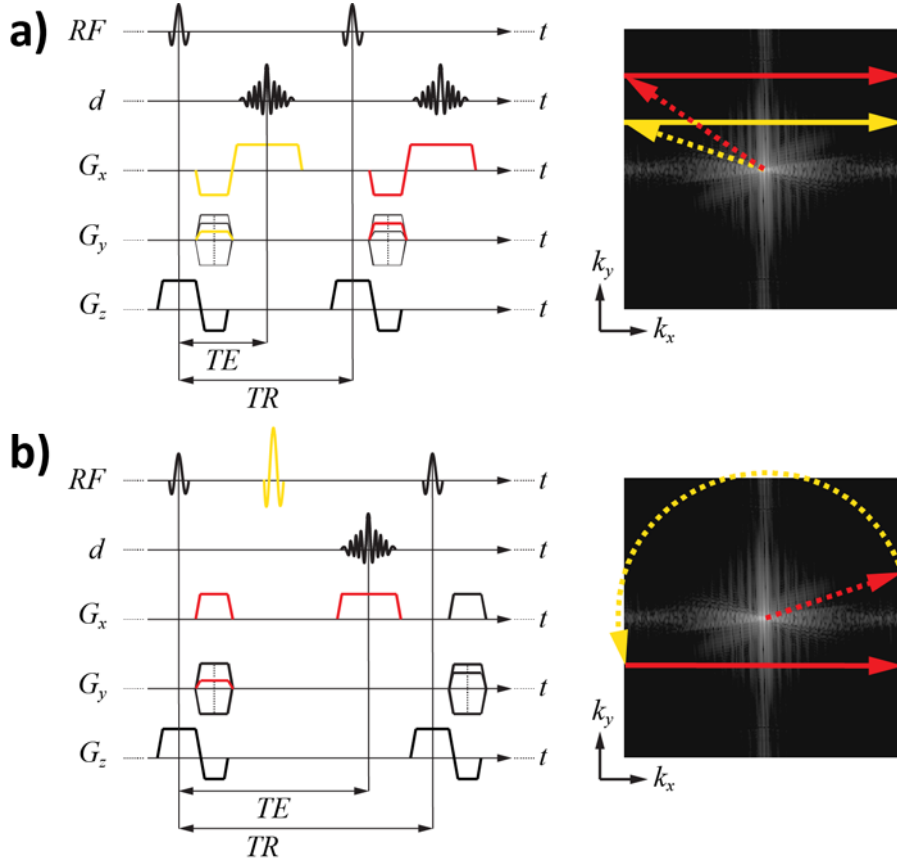


Figure 2.2 a) Illustration of a GRE sequence with $G_x(t)$ composed of a negative prephasing and a positive readout lobe. The corresponding k -space coverage is depicted on the right. Solid lines indicate the actual acquisition window during which signals are sampled. **b)** SE sequence with a positive prephasing and readout gradient separated by a 180° refocusing RF pulse. Both sequences depict full-echo acquisitions where readouts cover the whole k -space range $[-k_{x,max}, k_{x,max}]$ given by the spatial resolution. Partial-echo acquisitions consisting of smaller prephasing gradient areas sample intervals $[-k_{x,0}, k_{x,max}]$ with $0 \leq k_{x,0} < k_{x,max}$ enabling shorter TEs.

with the vectorized data samples $\mathbf{d} \in \mathbb{C}^M$, the discrete (sensitivity weighted) image $\mathbf{p} \in \mathbb{C}^N$ and the encoding matrix \mathbf{E} mapping the image to the acquired data. In case of Cartesian sampling, \mathbf{E} implements a concatenation of a (unitary) uniform Fourier transform (FT) $\mathbf{F} \in \mathbb{C}^{N \times N}$ and a sampling matrix $\mathbf{I}_u \in \{0,1\}^{M \times N}$: $\mathbf{E} = \mathbf{F}_u = \mathbf{I}_u \mathbf{F}$. Using N_c receiver coils, the encoding matrix reads

$$\mathbf{E} = (\mathbf{I}_{N_c} \otimes \mathbf{F}_u) \quad (2.10)$$

if the multi-coil images stacked in $\mathbf{p} = [\mathbf{p}_1^T, \dots, \mathbf{p}_{N_c}^T]^T$ are related to all channel's data $\mathbf{d} = [\mathbf{d}_1^T, \dots, \mathbf{d}_{N_c}^T]^T$, or

$$\mathbf{E} = (\mathbf{I}_{N_c} \otimes \mathbf{F}_u) \mathbf{S} \quad (2.11)$$

with $\mathbf{S} = [\mathbf{S}_1^T, \dots, \mathbf{S}_{N_c}^T]^T$ where the coil sensitivity diagonal matrices $\mathbf{S}_i \in \mathbb{C}^{N \times N}$ are known. For FT reconstruction, the data vector is pre-weighted with a diagonal matrix $\mathbf{W} \in \mathbb{R}^{N_c M \times N_c M}$, compensating for variable sampling density, followed by a multiplication with \mathbf{E}^H : $\mathbf{E}^H \mathbf{W} \mathbf{d}$. When the coil sensitivities are used, an additional diagonal weighting matrix multiplication with $\mathbf{W}_s \in \mathbb{R}^{N \times N}$, s.t. $\mathbf{W}_s \mathbf{S}^H \mathbf{S} = \mathbf{I}_N$, is added. An artifact-free image is obtained when $M = N$ and the k-space sampling distance Δk_i along the direction i fulfills the Nyquist sampling theorem with voxel size Δx_i ,

$$\Delta k_i \leq \frac{1}{N \Delta x_i} = \frac{1}{\text{FOV}_i}, \quad (2.12)$$

within a given field of view (FOV).

2.2.3 Radial Sampling

Radial imaging or projection acquisition where k-space is traversed along radial spokes (Figure 2.3) was the first sequence used in MRI [14, 19]. Radial imaging features a number of advantages relative to Cartesian imaging: 1) The absence of phase encoding gradients allows for short minimum echo times (TE). Partial-echo or ultra-short TE (UTE) sequences [20] with short or no prephasing gradients permit extremely short TEs, which are essential for imaging of short T_2 species. 2) The oversampled center of k-space provides a low-resolution image from undersampled data, which can be used as training, calibration or motion state data in advanced reconstruction algorithms [21-25]. 3) Motion leads to streak artifacts depending on the direction of object motion as opposed to rectilinear Fourier imaging where ghosting artifacts appear along the phase-encode direction regardless of the direction of motion [26]. In radial imaging, the oversampled low frequency components are averaged reducing motion-induced artifacts [26]. Each projection itself also contains information about movement enabling motion tracking and correction [27]. 4) Undersampling in the azimuthal direction generates streak artifacts, but the overall image structure is maintained (Figure 2.4) which is in contrast to Cartesian undersampling.

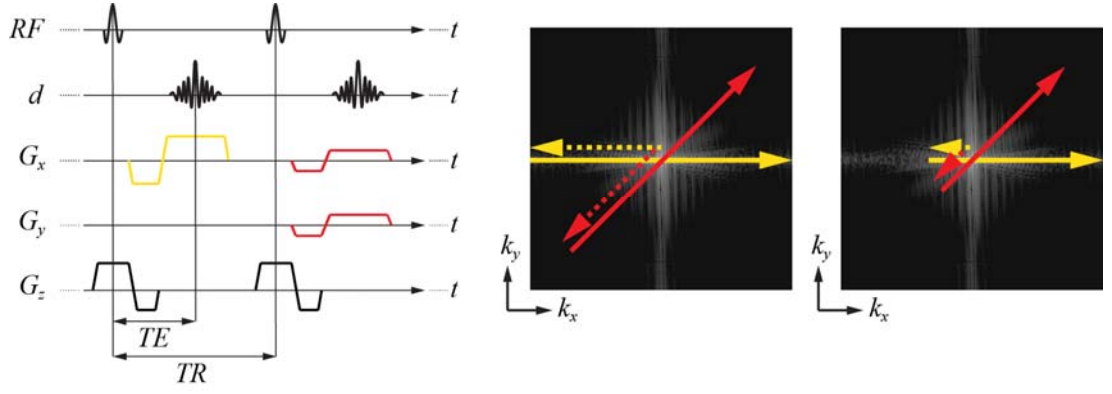


Figure 2.3 Full- and partial-echo radial GRE sequence. The prephasing and readout gradients are rotated about the center of k -space. Actual signal acquisition coinciding with the trajectory's solid lines is performed on the constant plateau of the readout lobe.

On the other hand, the Nyquist sampling criterion requires a larger set of measurements as compared to Cartesian imaging [17]:

$$P_{Nyquist} = \frac{\pi}{2} N_{PE}, \quad (2.13)$$

where N_{PE} is the number of phase encodes corresponding to a Cartesian scan with the same isotropic FOV and resolution.

Image reconstruction of radial data may be divided into three approaches:

Filtered backprojection The projection of an n -dimensional image is defined as the integral of the object function $\rho(\mathbf{r})$ over the $(n-1)$ -dimensional sub-planes perpendicular to the direction \mathbf{e}_r : $p(r, \mathbf{e}_r) = \int \rho(\mathbf{r}) \delta(r - \mathbf{r} \cdot \mathbf{e}_r) d\mathbf{r}$. Filtered backprojection algorithms are implementations of the inverse Radon transform which back-projects filtered projections [28]. The filtering is directly performed on the acquired profiles $d(k\mathbf{e}_r)$ which correspond to the FT of $p(r, \mathbf{e}_r)$. Images are then reconstructed according to:

$$\rho(\mathbf{r}) = \int_{S_{1/2}^n} \mathcal{F}_r^{-1} \{d(k\mathbf{e}_r)h(k)\} (\mathbf{r} \cdot \mathbf{e}_r, \mathbf{e}_r) d\mathbf{e}_r, \quad (2.14)$$

where integration is performed over the unit semi-circle $S_{1/2}^2$ or hemisphere $S_{1/2}^3$. Ideal filters $h(k)$ are $|k|$ and k^2 for 2D and 3D projections, respectively. However, to avoid noise amplification, band-limited filters are applied [28].

Gridding Gridding reconstruction implements a non-uniform inverse FT (IFT) from k - to image-space. The signal on the non-Cartesian sampling trajectory is interpolated onto a rectilinear grid

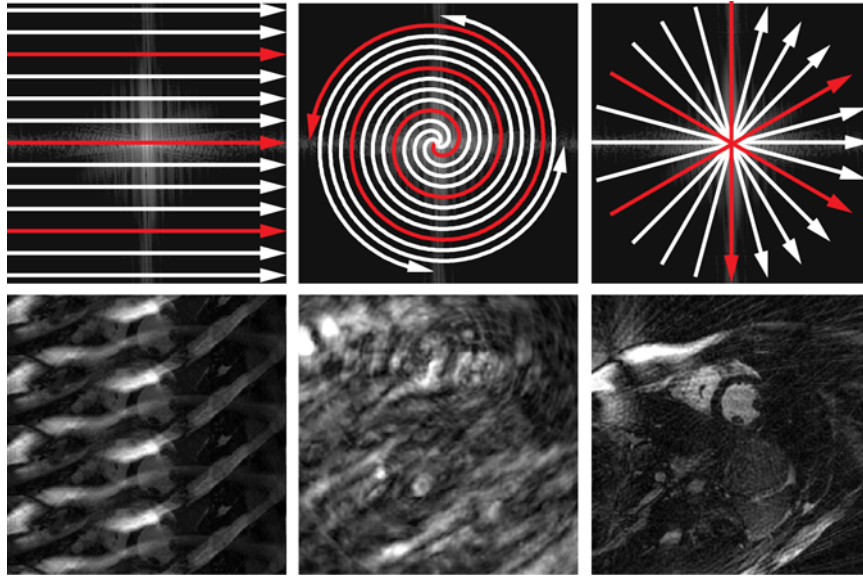


Figure 2.4 Cartesian (left column), spiral (middle) and radial (right column) undersampling artifacts from 4-fold undersampled short-axis view data. Regular Cartesian undersampling along the phase encoding direction leads to coherent aliasing along that direction while reduced spiral acquisition introduces severe streak- and swirl-like artifacts. Skipped radial profiles produce streaks but preserve the overall image structure.

via convolution interpolation, followed by a uniform inverse fast FT (IFFT) and a de-apodization step [29-31]. The block diagram in Figure 2.5 describes the general 3D interpolation process. The Cartesian signal after the convolution step,

$$d_c(\mathbf{k}) = \sum_i d(\mathbf{k}_i) h(\mathbf{k} - \mathbf{k}_i) w(\mathbf{k}_i), \quad (2.15)$$

reveals that gridding allows interpolation between any two trajectories, and thus, also from a rectilinear onto an arbitrary one. This is referred to as inverse gridding [32]. In this case, the 2D sampling density compensating weights are constant: $w(\mathbf{k}) = \Delta k_x \Delta k_y \Delta k_z$.

For equidistant 2D radial sampling, the i -th point's sampling weight in polar coordinates $(n_i \Delta k_r, \varphi_i)$ can be calculated analytically:

$$w(\mathbf{k}_i) = \begin{cases} \frac{\pi}{4P} (\Delta k_r)^2 & , n_i = 0 \\ \frac{\pi}{P} (\Delta k_r)^2 n_i & , n_i \neq 0 \end{cases}, \quad (2.16)$$

with the number of projections P , the radial sampling distance Δk_r , integer n_i , and

$0 \leq \varphi_i < 2\pi$. A widely used separable gridding kernel $h(\mathbf{k}) = f(k_x)f(k_y)f(k_z)$ is the Kaiser-Bessel (KB) window [33]:

$$f(k) = \frac{1}{W} I_0 \left(\beta \sqrt{1 - (2k/W)^2} \right), \quad (2.17)$$

where W denotes the kernel width, $I_0(\cdot)$ the zero-order modified Bessel function of the first kind, and β a shape parameter. [34] provides an optimal solution for a given kernel width and oversampling ratio α : $\beta = \pi ((W/\alpha)^2(\alpha - 0.5) - 0.8)^{1/2}$.

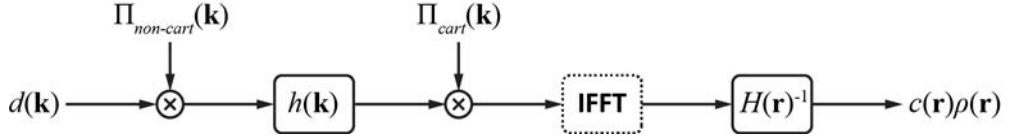


Figure 2.5 *Mathematical model of the image reconstruction process using gridding. The continuous k -space signal $d(\mathbf{k})$ is measured on a non-Cartesian trajectory. This is modeled by a multiplication with the sampling function $\Pi_{\text{non-cart}}(\mathbf{k}) = \sum_i \delta(\mathbf{k} - \mathbf{k}_i) w(\mathbf{k}_i)$ where $\{\mathbf{k}_i\}$ denotes the sample coordinates, $\delta(\cdot)$ the Dirac delta function and $w(\mathbf{k}_i)$ the corresponding sampling density compensating weights. The sampled signal is then convolved with the kernel $h(\mathbf{k})$ and resampled on a rectilinear grid by means of the delta comb $\Pi_{\text{cart}}(\mathbf{k}) = \sum_{m,n,l} \delta(k_x - m\Delta k_x, k_y - n\Delta k_y, k_z - l\Delta k_z) \Delta k_x \Delta k_y \Delta k_z$. Upon uniform IFFT, the coil image is filtered with the inverse of the kernel function's IFT, $H(\mathbf{r})$, to correct for potential attenuation of the image borders due to the convolution step.*

Non-uniform FFT (NUFFT) NUFFT implements a FT evaluated at non-uniformly spaced frequency locations. For the 1D case, this reads

$$X_m = X(\omega_m) = \sum_{n=0}^{N-1} x_n e^{-i\omega_m n} \quad m = 1, \dots, M, \quad (2.18)$$

with frequencies ω_m . Instead of directly evaluating (2.18), linear interpolation of an oversampled weighted K -point FFT, $Y_k = Y(2\pi k/K)$, of the equally spaced samples $\{x_n\}$ is used to approximate X_m :

$$X_m \approx \tilde{X}_m = \sum_{k=0}^{K-1} v_{mk}^* Y_k = \langle \mathbf{Y}, \mathbf{v}_m \rangle, \quad (2.19)$$

where \mathbf{v}_m is the interpolation coefficient vector for frequency ω_m . Reference [35] provides a solution for a min-max interpolator that minimizes the worst-case approximation error over all signals of unit norm:

$$\min_{\mathbf{v}_m} \max_{\mathbf{x} \in \mathbb{C}^N: \|\mathbf{x}\|_2 \leq 1} |\tilde{X}_m - X_m|. \quad (2.20)$$

The extension to higher-dimensional signals is outlined in [35]. The NUFFT operator actually implements an inverse gridding operation. Gridding in MRI, i.e. reconstructing an image from non-Cartesian trajectories is then formulated as an inverse problem:

$$\arg \min_{\boldsymbol{\rho}} \|\mathbf{d} - \mathbf{F}\boldsymbol{\rho}\|_2^2, \quad (2.21)$$

where \mathbf{F} implements the NUFFT matrix. Iterative solvers can then be used for the minimization problem (2.21) with the forward model \mathbf{F} and without sampling density compensation.

It can be shown that the sequence of points $\{x_0, x_1, \dots, x_m\}$ where $x_n = \{n\xi\}_{\text{mod } 1} = (1/F_i)\{nF_{i-1}\}_{\text{mod } F_i}$ ($i \rightarrow +\infty$) is distributed very evenly across the unit interval $[0, 1[$ (Figure 2.6a) [36, 37]. The Golden ratio ξ is the irrational number

$$\xi = \lim_{i \rightarrow +\infty} \frac{F_{i-1}}{F_i} = \frac{\sqrt{5}-1}{2}, \quad (2.22)$$

with $\{F_i\}$ being the integer Fibonacci sequence. Following this principle, a 2D radial Golden angle (GA) sampling scheme has been proposed for dynamic imaging providing a nearly uniform distribution of profiles over the interval $[0, 180^\circ[$ for each reconstruction window [38]. Adjacent projections are acquired with the fixed angular increment

$$\Delta\varphi = \xi 180^\circ \approx 111.25^\circ \quad (2.23)$$

allowing flexibility in temporal resolution and positioning of reconstructed image frames (Figure 2.6b). This concept has further been extended to 3D radial imaging with isotropic resolution and imaging volume, respectively [37], based on multi-dimensional Golden means ξ s.t. N -D points $\mathbf{x}_n = \{n\xi\}_{\text{mod } 1}$ provide near uniform coverage of $[0, 1]^N$ [36]. A near optimal coverage of the half unit sphere is then attained by approximately uniform sampling of a bounded 2D parameter space corresponding to sampled directions [37].

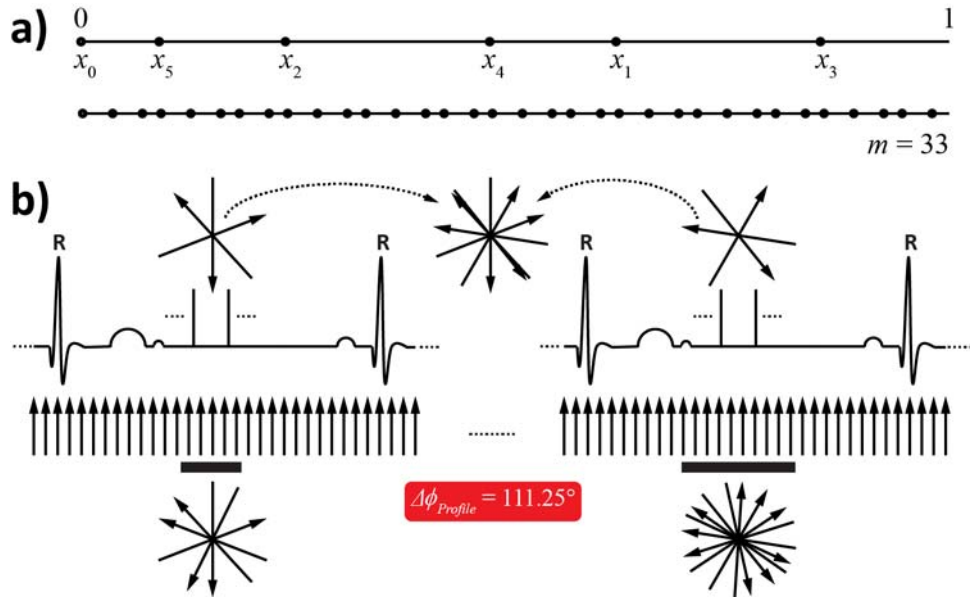


Figure 2.6 a) Illustration of subdividing the 1D unit interval using the Golden mean for a 6- (top) and 33 point (bottom) sequence. Each point x_n ($n > 0$) in the sequence is positioned s.t. it subdivides an interval into two segments whose lengths' ratio is the Golden mean ξ . **b)** The radial GA acquisition scheme allows arbitrary temporal resolution and positioning of reconstructed heart phases. Profiles acquired over multiple R-R intervals for a given reconstruction window can be pooled together without congruent projection. Figure a) is adapted from [37].

2.2.4 From Real- to Complex-Valued Signals

A receiver design must convert an analog real- into a complex-valued discrete signal agreeing with the models (2.8) and (2.9) for FT-based reconstruction. A classical quadrature receiver design is illustrated in (Figure 2.7a) [17]. The continuous time-frequency representation of a real valued MR signal during readout (neglecting relaxation effects),

$$s(t) \propto \int_V |\rho(\mathbf{r})| |c(\mathbf{r})| \sin(\omega_0 t + \mathbf{k}(t) \cdot \mathbf{r} + \phi_{\rho(\mathbf{r})} - \phi_{c(\mathbf{r})}) d\mathbf{r}, \quad (2.24)$$

is a band-pass signal with a carrier frequency of ω_0 and a bandwidth dependent on object size and readout gradient strength. $\phi_{\rho(\mathbf{r})}$ denotes the phase of transverse magnetization at the beginning of sampling and $\phi_{c(\mathbf{r})}$ the phase of the coil sensitivity. After low-pass filtering, the so called in-phase and quadrature component are centered at the zero frequency, i.e. the B_0 component has been removed. Upon discrete sampling, discrete in-phase and quadrature

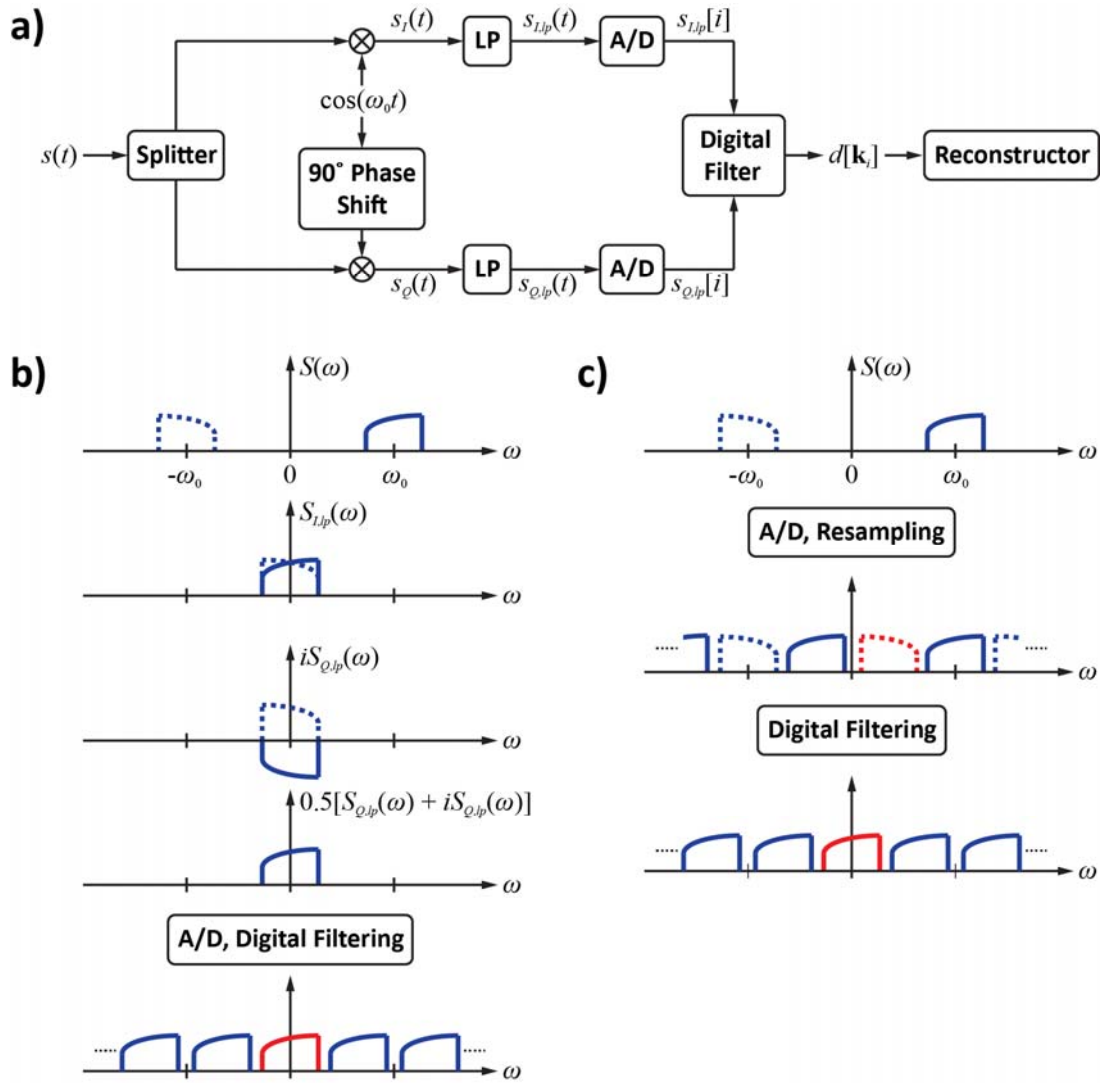


Figure 2.7 a) Illustration of a quadrature detection scheme transforming a real-valued signal $s(t)$ into a complex-valued $d[k_i]$ conforming with the k -space models (2.8) and (2.9). Before passing to the reconstructor, bandlimiting and resampling filters may be applied to the signal $s_{I,lp}[i] - is_{Q,lp}[i]$. **b)** Corresponding spectra of the bandpass signal within the quadrature scheme. **c)** Spectra within current direct digital receiver path without any demodulation. Upon high oversampling of $s(t)$, a resampling filter shifts the bandpass supports closer to the zero frequency. Proper centering is then achieved using digital filtering.

component are combined according to $s_{I,lp}[i] - is_{Q,lp}[i]$ leaving the spectrum of the complex valued signal corresponding to the readout k -space samples (Figure 2.7b).

New receiver designs do not transform precessing magnetization to the rotating coordinate system using analog demodulation. After digitization, the signal is bandlimited around a frequency > 0 and centered to zero with digital filtering (Figure 2.7c).

2.3 Flow Encoding

The signal model (2.8) can be extended to additionally encode information about flow by investigating the phase accumulation of moving spins in the presence of bipolar flow encoding gradients.

The precession frequency $\omega(\mathbf{x}, t) = \gamma(B_0 + \Delta B_0(\mathbf{x}(t)) + \mathbf{G}(t) \cdot \mathbf{x}(t))$ of a spin travelling on the trajectory $\mathbf{x}(t)$ leads to a phase accumulation after time t :

$$\phi(\mathbf{x}, t) = \gamma B_0 t + \gamma \int_0^t \Delta B_0(\mathbf{x}(\tau)) d\tau + \gamma \int_0^t \mathbf{G}(\tau) \cdot \mathbf{x}(\tau) d\tau. \quad (2.25)$$

Expanding $\mathbf{x}(t)$ in the right-hand term using a Taylor series about t_0 yields:

$$\mathbf{x}(t) = \mathbf{x}(t_0) + \frac{d\mathbf{x}(t_0)}{dt}(t - t_0) + \frac{1}{2} \frac{d^2\mathbf{x}(t_0)}{dt^2}(t - t_0)^2 + \dots \quad (2.26)$$

The applied gradient's first moment vector reads:

$$\mathbf{k}_v(t) = \gamma \int_0^t \mathbf{G}(\tau) \tau d\tau. \quad (2.27)$$

Bipolar waveforms of zero net area allow encoding velocity component along the direction of \mathbf{k}_v if terms after second order in (2.26) are neglected and $t_0 = t_m$ is assumed to be the center of gravity of the bipolar waveform. Upon combining (2.25)-(2.26), the velocity encoding signal model becomes [8, 39]:

$$d(\mathbf{k}, \mathbf{k}_v) = \int_{\mathbb{R}^3} \int_V c(\mathbf{r}) \rho(\mathbf{r}, \mathbf{v}) e^{-i(\mathbf{k} \cdot \mathbf{r} + \mathbf{k}_v \cdot \mathbf{v})} d\mathbf{r} d\mathbf{v}, \quad (2.28)$$

where $\rho(\mathbf{r}, \mathbf{v})$ is proportional to the spin density at location \mathbf{r} with velocity $\mathbf{v} = \mathbf{v}(t_m)$. These bipolar gradients are then combined with spatial encoding waveforms [17, 40] (Figure 2.8). In practice, orthogonal velocity components are acquired separately, and therefore, velocity is only encoded along the corresponding directions. In this case, the signal model can be modified by replacing the vectors \mathbf{k}_v and \mathbf{v} with the scalars k_v and v .

However, since spatial and functional encoding do not temporally match, i.e. $t_m \neq TE$, spatial misregistration of the velocity can occur. The resulting artefacts can be minimized by designing sequences with short TEs.

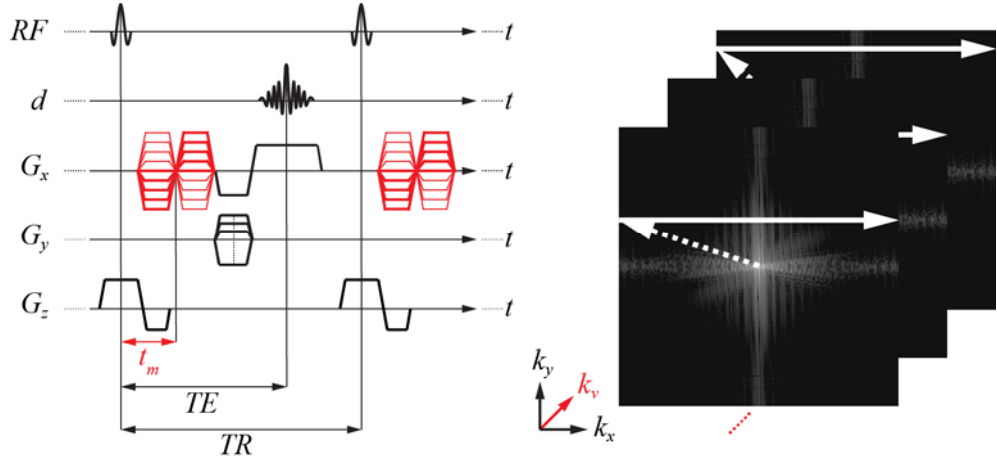


Figure 2.8 Schematic of a GRE sequence with bipolar waveforms and velocity sensitivity in readout direction (left). The amplitude of a bipolar gradient is incremented according to Δk_v . The velocity encoding first moment then defines a new axis in signal acquisition space (right).

2.3.1 Fourier Velocity Encoding

Fourier velocity encoding (FVE) allows reconstructing the velocity distribution or spectrum, $\rho(\mathbf{r}, v)$, in each voxel by acquiring a range of k_v -points (Figures 2.8 and 2.9) followed by an IFT of the signal $d(\mathbf{k}, k_v)$ along the spatial and velocity encoding axes. The Nyquist sampling distance for the k_v -axis then becomes:

$$\Delta k_v = \frac{1}{N_v \Delta v} = \frac{1}{FOS} = \frac{1}{2V_{enc}}, \quad (2.29)$$

with the number of samples N_v , the velocity resolution Δv , the field of speed FOS , and the highest detectable velocity V_{enc} (encoding velocity). However, the ability to resolve velocity distributions comes at the expense of scan time which is proportional to N_v and the increase in minimum TE due to higher gradient first moments required. With the assumption of Gaussian distributed velocities [12], i.e. velocity spectra fully characterized by mean v_m and standard deviation σ ,

$$\rho(\mathbf{r}, v) = \rho_0(\mathbf{r}) \frac{1}{\sqrt{2\pi}\sigma(\mathbf{r})} e^{-\frac{(v-v_m(\mathbf{r}))^2}{2\sigma(\mathbf{r})^2}}, \quad (2.30)$$

an analytical expression for the signal upon IFT along the spatial encodes is obtained:

$$d(\mathbf{r}, k_v) = \int_{\mathbb{R}} c(\mathbf{r}) \rho(\mathbf{r}, v) e^{-ik_v v} dv = c(\mathbf{r}) \rho_0(\mathbf{r}) e^{-\frac{k_v^2 \sigma(\mathbf{r})^2}{2} - ik_v v_m(\mathbf{r})}, \quad (2.31)$$

where $\rho_0(\mathbf{r})$ denotes the spatial spin density. Theoretically, from any two velocity encoded segments with $k_{v,1} \neq k_{v,2}$, mean velocity and standard deviation can be derived according to:

$$\frac{d(\mathbf{r}, k_{v,1})}{d(\mathbf{r}, k_{v,2})} = e^{-\frac{(k_{v,1}^2 - k_{v,2}^2)\sigma(\mathbf{r})^2}{2} - i(k_{v,1} - k_{v,2})v_m(\mathbf{r})}. \quad (2.32)$$

However, noise in the measurements requires an estimation of σ for a reliable quality of the fit in practice. Furthermore, the distance $k_{v,1} - k_{v,2}$ needs to be restricted to avoid wrapped mean velocity estimations.

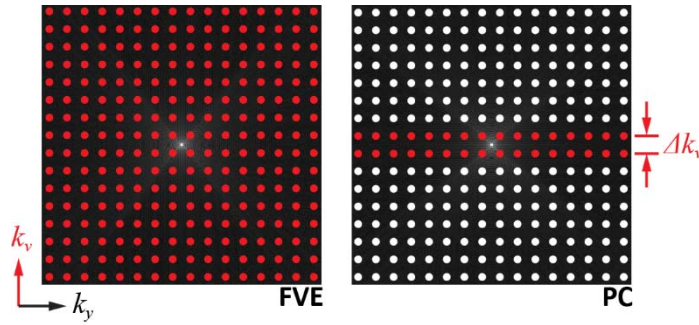


Figure 2.9 Illustration of the sampling pattern in the k_y - k_v plane in FVE and standard PC. For simplicity, the frequency encoding component k_x is omitted.

2.3.2 Phase-Contrast MRI

Phase-contrast (PC) velocity mapping assigns one velocity value $v(\mathbf{r})$ to each voxel [41],

$$\rho(\mathbf{r}, v) = \rho_0(\mathbf{r})\delta(v - v(\mathbf{r})), \quad (2.33)$$

with the Dirac delta function $\delta(\cdot)$, such that the phase modulated and sensitivity weighted spin density ρ_0 becomes $\rho(\mathbf{r}, k_v) \equiv c(\mathbf{r})\rho_0(\mathbf{r})e^{-ik_v v(\mathbf{r})}$ after IFT. Practically, measuring the phase difference $\Delta\phi(\mathbf{r})$ between two velocity-encoded measurements with different first gradient moments, $k_{v,1}$ and $k_{v,2}$, allows to calculate $v(\mathbf{r})$ by simultaneously eliminating field inhomogeneities and background phases:

$$\Delta\phi(\mathbf{r}) = \angle \left\{ \frac{\rho(\mathbf{r}, k_{v,1})}{\rho(\mathbf{r}, k_{v,2})} \right\} = \Delta k_v v(\mathbf{r}) = \frac{\pi}{V_{enc}} v(\mathbf{r}), \quad (2.34)$$

with V_{enc} corresponding to the maximum detectable velocity without phase wrapping. Figure 2.9 points out that PC can be seen as a special case of FVE where only two velocity-encodes are acquired.

Four-point PC encoding [42] is a 3D velocity vector field acquisition scheme where the phase of a reference segment ($k_v = 0$) is subtracted from the phase of three segments acquired with first moments applied along three orthogonal directions (x,y,z). The velocity vector $\mathbf{v} = (v_x, v_y, v_z)^T$ at position \mathbf{r} is then linearly related to the corresponding phase vector $\boldsymbol{\phi} = (\phi_0, \phi_x, \phi_y, \phi_z)^T$: $\mathbf{v} = \mathbf{A}\boldsymbol{\phi}$ with

$$\mathbf{A} = \begin{pmatrix} k_{v,x} & 0 & 0 \\ 0 & k_{v,y} & 0 \\ 0 & 0 & k_{v,z} \end{pmatrix}^{-1} \begin{pmatrix} -1 & 1 & 0 & 0 \\ -1 & 0 & 1 & 0 \\ -1 & 0 & 0 & 1 \end{pmatrix}. \quad (2.35)$$

2.3.3 Velocity-to-Noise Ratio

If the real and imaginary part of the noise in a receiver channel are uncorrelated and of equal amplitude, the variance of a complex-valued image phase σ_ϕ is given by [43]:

$$\sigma_\phi^2 = \frac{\sigma_m^2}{S_m^2} = \frac{1}{SNR_m^2}, \quad (2.36)$$

with standard deviation σ_m , signal strength S_m , and signal-to-noise ratio SNR_m of the corresponding magnitude image. After phase subtraction (2.34) of two images with approximately equal magnitude, the variance in the estimated velocity component v becomes [43]:

$$\sigma_v^2 = \frac{2V_{enc}^2}{\pi^2} \sigma_\phi^2, \quad (2.37)$$

resulting in a velocity-to-noise ratio (VNR) which is inversely proportional to the encoding velocity and proportional to signal SNR:

$$VNR = \frac{v}{\sigma_v} = \frac{\pi v}{\sqrt{2}V_{enc} \sigma_\phi} \propto \frac{v}{V_{enc}} SNR_m. \quad (2.38)$$

The SNR of the image magnitude itself is proportional to the voxel size and the square root of the total acquisition time T_{acq} [44]:

$$SNR_m \propto \Delta x \Delta y \Delta z \sqrt{T_{acq}} = \Delta x \Delta y \Delta z \sqrt{\frac{N_{readout} N_{sample}}{BW}}, \quad (2.39)$$

with the total number of encoding profiles $N_{readout}$, samples N_{sample} along each profile and the receiver bandwidth BW .

The relation (2.39) holds only for uniform k-space sampling like equidistant Cartesian sampling. If a variable sampling density is used, density compensation needs to be accounted for. Maintaining spatial resolution and total acquisition time, the loss in SNR relative to constant density sampling may be described by the SNR efficiency factor [45]:

$$\eta = \frac{A_k}{\sqrt{\int w(\mathbf{k})d\mathbf{k} \int w(\mathbf{k})^{-1}d\mathbf{k}}} \leq 1, \quad (2.40)$$

where A_k denotes the k-space area covered by the trajectory and $w(\mathbf{k})$ the sampling density weights. For 2D projection reconstruction, the efficiency factor is given by $\eta = 3^{1/2} / 2 = 0.866$ revealing a loss of 13.4% in SNR.

2.3.4 Concomitant Fields and Eddy Currents

Fundamental laws of physics and MR system imperfections introduce image artifacts related to the linear encoding model (2.28). These errors affect the phase accumulation and can be modeled as spatially dependent phase offsets $\phi_e(\mathbf{r}, \mathbf{k}_v)$:

$$d(\mathbf{k}, \mathbf{k}_v) = \int_{\mathbb{R}^3} \int_V c(\mathbf{r}) \rho(\mathbf{r}, \mathbf{v}) e^{i\phi_e(\mathbf{r}, \mathbf{k}_v)} e^{-i(\mathbf{k} \cdot \mathbf{r} + \mathbf{k}_v \cdot \mathbf{v})} d\mathbf{r} d\mathbf{v}. \quad (2.41)$$

The additional phase term includes field inhomogeneities, concomitant gradient field and eddy current induced errors. While time-invariant field effects can be removed by the phase subtraction in PC MRI, gradient non-linearities lead to deviations from the nominal gradient strength and direction resulting in spatially dependent gradient first moments, respectively. This error in V_{enc} and encoding direction can be corrected for if the gradient coil model parameters generating the field imperfections are known [46].

Assuming a divergence- and curl-free magnetic field in the scanner bore, a spatially varying field $\mathbf{B}(\mathbf{r})$ has to obey $\nabla \cdot \mathbf{B} = \text{div } \mathbf{B} = 0$ and $\nabla \times \mathbf{B} = \text{curl } \mathbf{B} = \mathbf{0}$. The linear encoding field purely aligned with the z-axis, $\mathbf{B}(\mathbf{r}) = B_0 \mathbf{e}_z + \mathbf{G} \cdot \mathbf{r}$, fulfils the divergence- but not the curl-free condition. In consequence, it can be shown that components B_x and B_y perpendicular to the longitudinal axis are introduced, and thus, the net field is increased resulting in spatially dependent differences in precession frequencies (Figure 2.10). With current MRI systems, the altered magnetic field magnitude is approximated by $\|\mathbf{B}(x,y,z,t)\|_2 = B_0 + \mathbf{G}(t) \cdot \mathbf{r} + B_t(x,y,z,t)$ with the non-negative

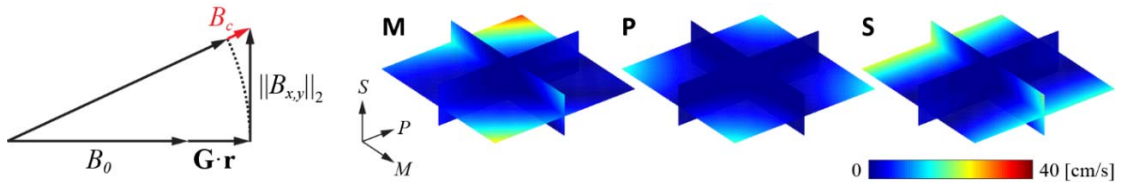


Figure 2.10 Illustration of the altered net magnetic field resulting from transverse components arising due to the field gradients. The concomitant field B_c exceeding the nominal field leads to phase offsets which cannot be removed by the phase subtraction in PC imaging. Remaining velocity offsets (in a 4-point PC experiment) along three orthogonal directions M-P-S are also shown.

concomitant field term revealing non-linear spatial dependencies [17, 47]:

$$B_c(x, y, z, t) = \frac{1}{2B_0} [G_x(t)^2 z^2 + G_y(t)^2 z^2 + \dots \dots G_z(t)^2 \frac{x^2 + y^2}{4} - G_x(t)G_z(t)xz - G_y(t)G_z(t)yz] . \quad (2.42)$$

This adds a phase accumulation according to $\phi_c(\mathbf{r}, \mathbf{k}_v) = \gamma \int_0^t B_c(x, y, z, B_0, G_x(\tau), G_y(\tau), G_z(\tau)) d\tau$. Since different gradient first moments have different concomitant field phase offsets, they are not removed by the phase subtraction in PC imaging. However, from the nominal gradient waveforms, coefficients (a, b, c, d) related to the concomitant gradient cross- and self-squared terms can be calculated and the corresponding phase offset contribution in $\phi_e(\mathbf{r}, \mathbf{k}_v)$ is eliminated by voxel-wise subtraction prior to phase difference calculations:

$$\rho(\mathbf{r}, \mathbf{k}_v) \leftarrow \rho(\mathbf{r}, \mathbf{k}_v) e^{-i\phi_c(\mathbf{r}, \mathbf{k}_v)} = \rho(\mathbf{r}, \mathbf{k}_v) e^{-i(a z^2 + b(x^2 + y^2) + c x z + d y z)} , \quad (2.43)$$

with $a = (\gamma / 2B_0) \int [G_x(\tau)^2 + G_y(\tau)^2] d\tau$, $b = (\gamma / 8B_0) \int G_z(\tau)^2 d\tau$, $c = (-\gamma / 2B_0) \int G_x(\tau)G_z(\tau) d\tau$ and $d = (-\gamma / 2B_0) \int G_y(\tau)G_z(\tau) d\tau$.

Another source of deviation of the actual from the nominal gradient waveform is related to eddy currents. According to Faraday's law, time-varying magnetic fields produced by gradient coils induce currents in conductive structures within the scanner system. These eddy currents themselves build up magnetic fields counteracting the nominal pulse shapes resulting in distorted gradient functions, temporally shifted and biased in strength, which translates into k-space trajectory misalignment and phase fluctuations [17]. To correct for these error sources, MRI systems are equipped with gradient shield coils cancelling induction effects of the imaging gradients to some extent [48]. These are placed around the gradient coils and are driven by input

currents such that the magnetic flux is minimized outside the shield. In addition, gradient pre-emphasis modulates the imaging gradient's input currents to prospectively compensate for the eddy current disturbances. The induced eddy currents in conductive structures are approximated by a series of LR-circuits inductively coupled to a gradient coil [49]. The total gradient waveform $\mathbf{g}(t)$ generated by a gradient coil is then given by the superposition of the input current $\mathbf{i}(t)$ and eddy currents $\mathbf{i}_k(t)$:

$$\mathbf{g}(t) = a\mathbf{i}(t) + \sum_k \mathbf{a}_k \mathbf{i}_k(t). \quad (2.44)$$

Linear time-invariant system (LTI) theory directly relates the input current to the resulting gradient shape in the Laplace transform domain:

$$\mathbf{G}(s) = a \left(1 - \sum_k c_k \frac{s}{s + w_k} \right) \mathbf{I}(s) = \mathbf{H}(s) \mathbf{I}(s). \quad (2.45)$$

Coefficients c_k and w_k collect model parameters and $\mathbf{H}(s)$ is the impulse response function of the LTI system. Using an ideally switching gradient and a step function input current $\mathbf{I}(s) = 1/s$, respectively, the eddy current gradients become exponentially decaying distortions:

$$\mathbf{g}(t) = a \left(1 - \sum_k c_k e^{-w_k t} \right). \quad (2.46)$$

Gradient waveform pre-emphasis then corresponds to finding an input current $\mathbf{i}(t)/\mathbf{I}(s)$ for a desired waveform $\mathbf{g}(t)/\mathbf{G}(s)$. However, eddy currents induced by a gradient coil do not only disturb the field along the direction of the gradient, they can also generate temporally decaying components along the other two orthogonal directions which have to be compensated for:

$$\begin{pmatrix} G_x(s) \\ G_y(s) \\ G_z(s) \end{pmatrix} = \begin{pmatrix} H_{xx}(s) & H_{xy}(s) & H_{xz}(s) \\ H_{yx}(s) & H_{yy}(s) & H_{yz}(s) \\ H_{zx}(s) & H_{zy}(s) & H_{zz}(s) \end{pmatrix} \begin{pmatrix} I_x(s) \\ I_y(s) \\ I_z(s) \end{pmatrix}, \quad (2.47)$$

where e.g. $H_{xy}(s)$ accounts for the eddy current effects in the x-channel when the y-gradient is activated by $I_y(s)$. Since the model parameters in (2.44) and (2.45) are not known, they are measured using free induction decay (FID) experiments where phase evolutions of field probes at different spatial locations are recorded after a gradient pulse followed by a non-selective RF excitation [17]. The time derivative of the phase then allows deriving the gradient fields at the corresponding locations.

The combination of shielded imaging gradients and eddy current pre-emphasis is sufficient for most MRI applications. However, in flow-encoded MRI where different images are acquired with

different encoding gradients, remaining eddy current related phase offsets are not nulled in velocity field reconstructions. Image-based methods typically employ a polynomial phase correction function derived from static tissue voxels which is then subtracted from the phase differences maps [50, 51]. Therefore, the success of these methods depends on the availability of static tissue voxels with sufficient VNR. Phase offsets can also be derived from phantom calibration scans where the measurement is repeated, and thus, scan time doubled [52]. Recent advances in spatio-temporal magnetic field monitoring [53] allow to directly measure velocity offsets in PC experiments in short calibration scans. Further improvement can be expected from progress in gradient waveform pre-emphasis composed of more comprehensive error models including field monitoring [54].

Chapter 3

Image Reconstruction

A realistic discrete signal model incorporates additive zero-mean complex-valued Gaussian noise with independent real and imaginary part [55]:

$$\mathbf{d} = \mathbf{E}\boldsymbol{\rho} + \boldsymbol{\eta}, \quad (3.1)$$

where the elements of the noise vector $\boldsymbol{\eta} \in \mathbb{C}^{N_c M}$ are uncorrelated over time and k-space, respectively, but may be correlated among receiver channels [56].

MR image reconstruction aims to invert the linear system of equations (3.1). Solutions minimizing the data fidelity least squares term $\|\mathbf{d} - \mathbf{E}\boldsymbol{\rho}\|_2^2$ fulfill the normal equation $\mathbf{E}^H \mathbf{E} \boldsymbol{\rho} = \mathbf{E}^H \mathbf{d}$. The corresponding minimum-norm solution for underdetermined ($N_c M < N$) and the projection onto the range space of \mathbf{E} for overdetermined ($N_c M > N$) linear systems with full rank encoding matrices is given by the Moore-Penrose pseudo-inverse, $\mathbf{E}^\dagger \mathbf{d}$, which reads $\mathbf{E}^\dagger = \mathbf{E}^H (\mathbf{E} \mathbf{E}^H)^{-1}$ and $\mathbf{E}^\dagger = (\mathbf{E}^H \mathbf{E})^{-1} \mathbf{E}^H$, respectively [57]. Depending on the existence, uniqueness and stability of the inversion, additional prior knowledge can be incorporated via regularization terms $R_i(\cdot)$ to restrict the solution space or guarantee a stable inversion. Further generalization of the data consistency term by a positive definite matrix \mathbf{W} leads then to the following formulation of the image reconstruction problem:

$$\arg \min_{\boldsymbol{\rho}} (\mathbf{d} - \mathbf{E}\boldsymbol{\rho})^H \mathbf{W} (\mathbf{d} - \mathbf{E}\boldsymbol{\rho}) + \sum_i \lambda_i^2 R_i(\boldsymbol{\rho}), \quad (3.2)$$

with the regularization parameters λ_i trading data fidelity and regularization. When the R_i 's implement quadratic cost functions of the form $R_i(\boldsymbol{\rho}) = \boldsymbol{\rho}^H \mathbf{R}_i \boldsymbol{\rho}$ with positive definite matrices \mathbf{R}_i , the solution minimizing (3.2) becomes linear in \mathbf{d} by setting the gradient of the error functional to zero. For an overdetermined system, the solution then reads $(\mathbf{E}^H \mathbf{W} \mathbf{E} + \sum_i \lambda_i^2 \mathbf{R}_i)^{-1} \mathbf{E}^H \mathbf{W} \mathbf{d}$, while for an underdetermined problem $(\sum_i \lambda_i^2 \mathbf{R}_i)^{-1} \mathbf{E}^H (\mathbf{E} (\sum_i \lambda_i^2 \mathbf{R}_i)^{-1} \mathbf{E}^H + \mathbf{W}^{-1})^{-1} \mathbf{d}$ results. The two

solutions are analytically equivalent and connected via a variant the Woodbury matrix identity* [58]. However, the second expression provides a numerically more stable inversion when \mathbf{E} has more columns than rows. For the function $R_i(\boldsymbol{\rho}) = \|\mathbf{A}_i \boldsymbol{\rho}\|_2^2$, \mathbf{R}_i becomes $\mathbf{A}_i^H \mathbf{A}_i$.

3.1 Parallel Imaging

Parallel imaging (PI) reconstructs images from undersampled data by exploiting redundancy in the encoding process due to coil sensitivity weighting. Knowing the coil sensitivities, this redundancy is reflected by the tall matrix structure (more rows than columns) of the encoding operator. When skipping k-space profiles, aliasing artifacts are then composed of superpositions of sensitivity weighted voxels which can be mapped back to the unfolded object using linear algebra [56, 59]. However, the estimation of accurate sensitivity maps is essential for good reconstruction quality and prone to different sources of errors, e.g. spatial misregistration between calibration and actual scan, field of view (FOV) limitations [60, 61], or extrapolation to regions with low spin density [62]. Auto-calibrating k-space methods reconstruct multi-coil k-space data without the need of coil map estimation [63]. Sensitivity weighting translates into a correlated multi-coil k-space due to the convolution with the FTs of the sensitivity maps. These k-space correlations can directly be extracted from the acquired data.

3.1.1 SENSE

In the sensitivity encoding (SENSE) model, redundancy due to sensitivity weighting of the Cartesian object vector $\boldsymbol{\rho} \in \mathbb{C}^N$ is reflected by the structure of the encoding matrix $\mathbf{E} = (\mathbf{I}_{N_c} \otimes \mathbf{F}_u) \mathbf{S} \in \mathbb{C}^{N_c M \times N}$ with the FFT or NUFFT operator \mathbf{F}_u , when the total number of measurements $N_c M$ exceeds the Nyquist sampling rate given by the k-space trajectory, the FOV and resolution of the imaging volume. A noise optimal inversion of (3.1) is given by minimizing a weighted least-squares problem (3.2) with the weighting matrix \mathbf{W} being the inverse of the noise covariance matrix or sample noise matrix [56]

$$\boldsymbol{\Psi} = \overline{\boldsymbol{\eta} \boldsymbol{\eta}^H} = \boldsymbol{\Psi}_c \otimes \mathbf{I}_M, \quad (3.3)$$

* $(\mathbf{A}\mathbf{B}^{-1}\mathbf{C} - \mathbf{D})^{-1}\mathbf{A}\mathbf{B}^{-1} = \mathbf{D}^{-1}\mathbf{A}(\mathbf{C}\mathbf{D}^{-1}\mathbf{A} - \mathbf{B})^{-1}$

with Ψ_c the $N_c \times N_c$ receiver noise matrix. The noise matrix contains noise variances of each receiver channel along the diagonal, while reflecting inter-channel noise correlations in the off-diagonal elements. The signal-to-noise optimal solution in this case is obtained as:

$$\boldsymbol{\rho} = (\mathbf{E}^H \boldsymbol{\Psi}^{-1} \mathbf{E})^{-1} \mathbf{E}^H \boldsymbol{\Psi}^{-1} \mathbf{d}. \quad (3.4)$$

The effect of the weighting matrix can be illustrated when Ψ_c is assumed to have entries on the diagonal only. In this case, each component of the data consistency term is weighted according to the coupling of the coil to the object of interest. By modifying the data vector, $\mathbf{d} \rightarrow \tilde{\mathbf{d}}$, and sensitivity maps, $\mathbf{E} \rightarrow \tilde{\mathbf{E}}$, $\boldsymbol{\Psi}$ can be eliminated from (3.4) by a noise-decorrelation process using Cholesky decomposition of Ψ_c [59]: $\boldsymbol{\rho} = (\tilde{\mathbf{E}}^H \tilde{\mathbf{E}})^{-1} \tilde{\mathbf{E}}^H \tilde{\mathbf{d}}$. If M equals the Nyquist sampling rate, (3.4) is referred to as Roemer combination [64] of multi-coil data.

The theoretical maximum undersampling factor R is limited by noise amplification caused by the reduced amount of acquired data samples and the degree of redundancy introduced by \mathbf{S} in the encoding matrix \mathbf{E} . The resulting local image space noise amplification relative to the fully sampled case is then inversely proportional to the so called geometry factor and the square root of R [56].

3.1.2 GRAPPA

While SENSE requires explicit knowledge of coil sensitivities to provide the coil-combined image $\boldsymbol{\rho} \in \mathbb{C}^N$, Cartesian generalized auto-calibrating partially parallel acquisitions (GRAPPA) [63] inverts (3.1) by reconstructing multi-coil k-space data $(\mathbf{I}_{N_c} \otimes \mathbf{F})\boldsymbol{\rho} \in \mathbb{C}^{N_c N}$ by means of a k-space interpolation scheme:

$$\boldsymbol{\rho} = (\mathbf{I}_{N_c} \otimes \mathbf{F}^H) \mathbf{G} (\mathbf{I}_{N_c} \otimes \mathbf{I}_u^T) \mathbf{d}, \quad (3.5)$$

where \mathbf{G} is composed of interpolation kernels for each coil synthesizing missing from acquired samples (Figure 3.1a). The number of kernels per coils depends on the different sampling patterns occurring when shifting a k-space data block over the missing k-space points. Inner- and inter-coil signal correlations which are assumed to be valid over the full k-space are informed from a fully sampled calibration area acquired in the center of k-space. This can be achieved with a so-called calibration matrix \mathbf{A} whose rows contain vectorized data blocks shifted over the calibration data (Figure 3.1a). The vectorized interpolation weights $\mathbf{g}_{i,s}$ corresponding to the i -th coil and the local

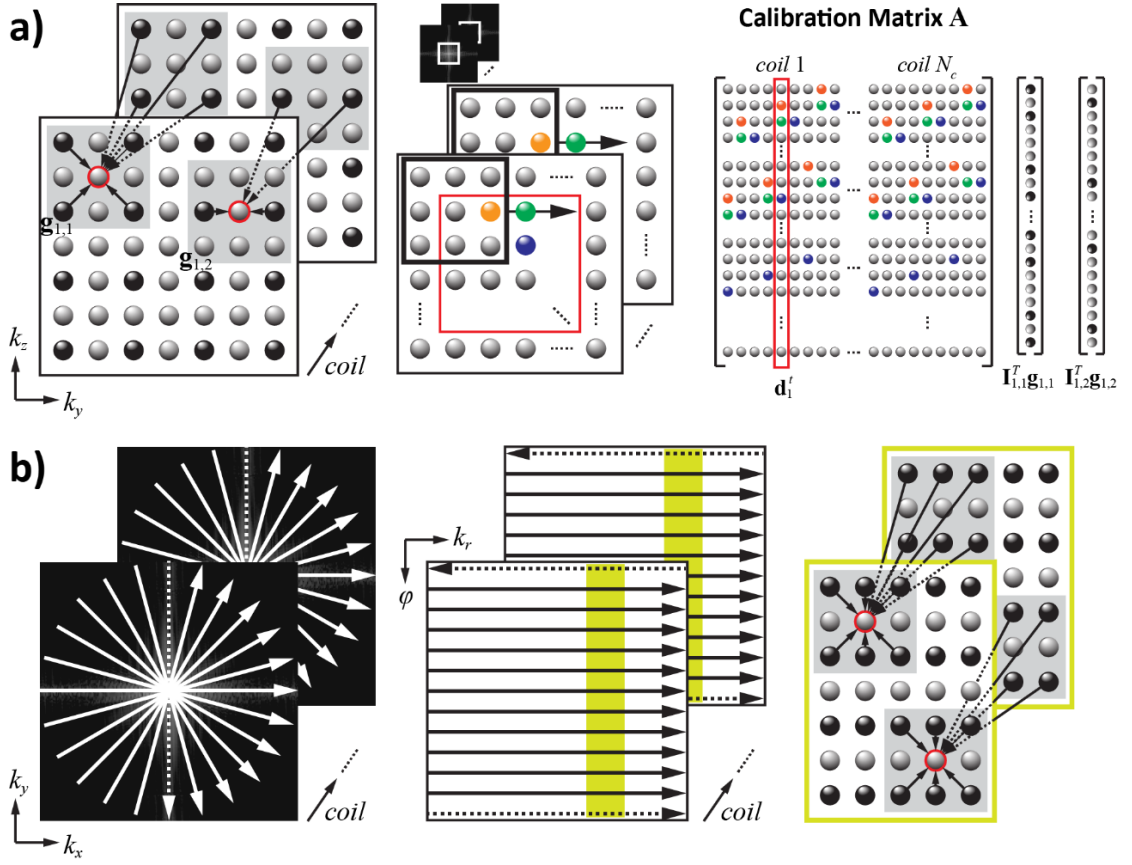


Figure 3.1 a) Cartesian GRAPPA linear k -space interpolation scheme. Missing (gray) phase encodes are synthesized from acquired (black) lines within a predefined neighborhood (gray blocks) across all coils (left). The coil specific and position dependent interpolation weights $\mathbf{g}_{i,s}$ are fitted to a fully sampled center of k -space (middle) by means of the calibration matrix \mathbf{A} (right) composed of vectorized k -space blocks shifted line by line over the calibration area. The corresponding first coil's calibration target points are indicated by the red area and column, respectively. **b)** Illustration of radial GRAPPA where profiles (right) are reordered in a hybrid k -space according to their angular positions (middle). Cartesian GRAPPA is then applied on segment along the radial components (right). Figure adapted from [23, 65, 66].

sampling pattern indexed by s can then be derived from following inverse problem:

$$\mathbf{d}_i^t = \mathbf{A}\mathbf{e}_i = \mathbf{A}\mathbf{I}_s^T \mathbf{g}_{i,s}, \quad (3.6)$$

with \mathbf{d}_i^t being the i -th coil's interpolation target points within the calibration area, \mathbf{e}_i a unit vector with a one at the component corresponding to the position of the target point within the vectorized full data block over all coils and \mathbf{I}_s a sampling matrix that extracts only acquired points from the local k -space grid.

Non-Cartesian GRAPPA methods are based on shifting acquired k-space points to the appropriate nearest Cartesian location [67] or rearranging the data into a Cartesian parameter space where standard GRAPPA can be performed [66, 68]. For example, 2D radial GRAPPA first reorders the acquired and missing projections onto a Cartesian grid with the two dimensions referring to angular and readout position (Figure 3.1b). This hybrid data space is then subdivided into segments along the readout direction which are then reconstructed separately using Cartesian GRAPPA.

3.1.3 SPIRiT/ESPIRiT

Iterative self-consistent PI reconstruction (SPIRiT) [23] is a recently proposed auto-calibrating method generalizing GRAPPA. A Cartesian multi-coil k-space \mathbf{d}_c is generated from samples \mathbf{d} acquired along an arbitrary sampling trajectory with the constraint of calibration consistency $\mathbf{d}_c = \mathbf{G}\mathbf{d}_c$, i.e. each Cartesian k-space point, whether acquired or not, is expressed as a linear combination of all k-space points within a local neighborhood across all channels (Figure 3.2). In contrast to GRAPPA, \mathbf{G} implements a Cartesian shift-invariant interpolation scheme, assuming fixed signal correlations over a fully sampled local neighborhood, independent of the local sampling patterns. Data fidelity with arbitrary trajectories is imposed by using a linear operator \mathbf{E}_k mapping reconstructed Cartesian k-space to \mathbf{d} : $\mathbf{d} = \mathbf{E}_k\mathbf{d}_c$. Since \mathbf{G} is composed of k-space convolution matrices, the calibration consistency constraint can be easily reformulated in image space by means of a matrix \mathbf{G}_x replacing the convolution operators with diagonal matrices corresponding to the image-domain representation of the k-space interpolation kernels: $\boldsymbol{\rho} = \mathbf{G}_x\boldsymbol{\rho}$. Thereby, voxel-wise multiplications of the multi-coil images $\boldsymbol{\rho}$ with the IFTs of the SPIRiT convolution kernels is implemented followed by summations over the coil dimension. Transforming \mathbf{G} into image space, replacing \mathbf{E}_c with the corresponding encoding matrix \mathbf{E} and relaxing these two linear constraints, image reconstruction can then be formulated as an unconstrained Lagrangian optimization problem:

$$\arg \min_{\boldsymbol{\rho}} \|\mathbf{d} - \mathbf{E}\boldsymbol{\rho}\|_2^2 + \lambda^2 \|\mathbf{G}_x - \mathbf{I}\boldsymbol{\rho}\|_2^2 + R(\boldsymbol{\rho}), \quad (3.7)$$

with λ trading data and calibration consistency and $R(\cdot)$ incorporating further regularization on the estimated multi-channel image.

\mathbf{G}_x reduces to voxel-wise matrix-vector multiplications $\boldsymbol{\rho}_n(\mathbf{r}) = \mathbf{G}_x(\mathbf{r})\boldsymbol{\rho}_{n-1}(\mathbf{r})$, updating the $N_c \times 1$ multi-channel image vector $\boldsymbol{\rho}_{n-1}(\mathbf{r})$ via the $N_c \times N_c$ matrix $\mathbf{G}_x(\mathbf{r})$ composed of the values of the inverse Fourier transformed convolution kernels at position \mathbf{r} , during iteration step n using an iterative solver for (3.7). Ideally, the solution converges to the scalar object function $\rho(\mathbf{r}) \in \mathbb{C}$

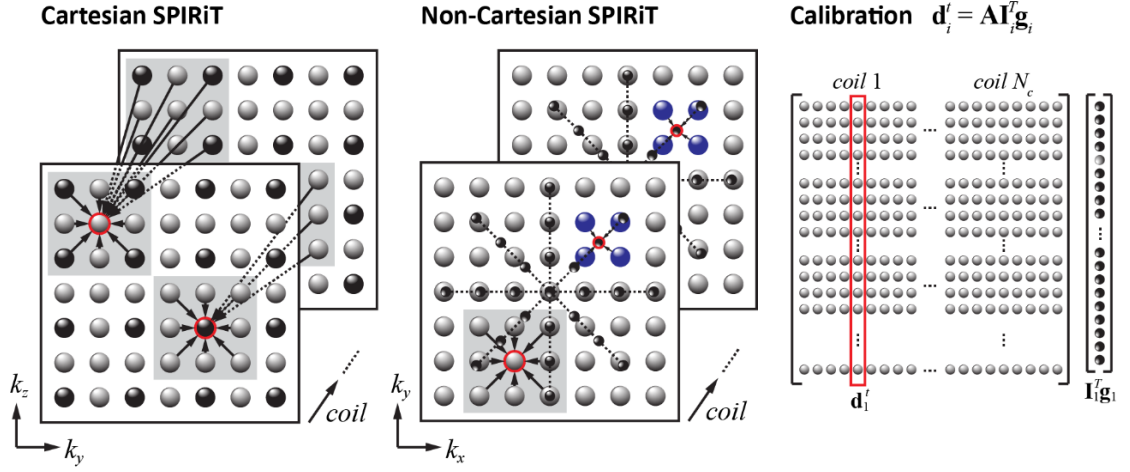


Figure 3.2 Illustration of the SPIRiT calibration consistency operation (left), inclusion of non-Cartesian trajectories (middle) and the calibration step (right). Generalizing GRAPPA, each Cartesian k -space point (whether acquired or not) is expressed as linear combination of all k -space samples within a predefined vicinity across all coils. Data consistency with non-Cartesian samples is enforced by a regridding operation relating reconstructed Cartesian k -space to the non-Cartesian trajectory. If the calibration matrix \mathbf{A} is assembled according to Figure 3.1a, calibration target vectors \mathbf{d}_i^T can directly be extracted from \mathbf{A} . Figure adapted from [23].

modulated by the coil sensitivity vector $\mathbf{c}(\mathbf{r}) \in \mathbb{C}^{N_c}$: $\lim_{n \rightarrow +\infty} \mathbf{p}_n(\mathbf{r}) = \rho(\mathbf{r})\mathbf{c}(\mathbf{r})$. With the above matrix-vector multiplication, this leads to:

$$\mathbf{c}(\mathbf{r}) = \mathbf{G}_x(\mathbf{r})\mathbf{c}(\mathbf{r}), \quad (3.8)$$

stating that the coil sensitivity vectors are the eigenvectors of the calibration matrices $\mathbf{G}_x(\mathbf{r})$ corresponding to the eigenvalue of 1. In practice only information about the relative spatial positioning between the coils can be extracted, and thus, the phase of an arbitrary reference coil needs to be subtracted from every coil map after the voxel-wise eigendecomposition of \mathbf{G}_x . Following these steps, one can proceed with SENSE or computationally optimized SPIRiT reconstruction (ESPIRiT) [65, 69]. However, this relation between the calibration operator and the coil sensitivity maps is fairly intuitive. A mathematically more profound relation is derived in [65], based on a different calibration operator. The underlying assumption is that all multi-coil k -space data blocks are spanned by the same orthonormal vector set generating the calibration data. Using the calibration matrix \mathbf{A} , whose rows are composed of the vectorized k -space blocks, basis vectors can be calculated using singular value decomposition of \mathbf{A} : $\mathbf{A} = \mathbf{U}\mathbf{\Sigma}\mathbf{V}^H$. The modified self-consistency operator then locally projects each data block $\mathbf{I}_k\mathbf{d}_c$ onto the subspace generated

by \mathbf{V}_{\parallel} (matrix with column vectors supporting the row space of \mathbf{A} according to the singular values in $\mathbf{\Sigma}$), plugs the projected data back into the k-space grid and averages overlapping positions:

$$\mathbf{G} = \mathbf{M}^{-1} \sum_{\mathbf{k}} \mathbf{I}_{\mathbf{k}}^T \mathbf{V}_{\parallel} \mathbf{V}_{\parallel}^H \mathbf{I}_{\mathbf{k}}, \quad (3.9)$$

with the diagonal matrix $\mathbf{M} = \sum_{\mathbf{k}} \mathbf{I}_{\mathbf{k}}^T \mathbf{I}_{\mathbf{k}}$. The rows of $\mathbf{V}_{\parallel} \mathbf{V}_{\parallel}^H$ can be viewed as multiple SPIRiT kernels working in parallel whose output images are averaged under the assumption of periodic boundary conditions. The image-domain implementation \mathbf{G}_x of \mathbf{G} and the estimation of normalized sensitivity maps ($\mathbf{S}^H \mathbf{S} = \mathbf{I}_N$) are further detailed in [65].

3.2 Compressed Sensing

Sparsity-promoting inversion of linear systems has gained a lot of attention in the signal processing community over recent years. Underdetermined linear systems of equations, $\mathbf{y} = \mathbf{A}\mathbf{z}$, have in general no or infinitely many solutions. If the system matrix has full rank, the pseudo-inverse gives the minimum-norm solution. However, it has been shown that one can recover a unique sparse solution vector solving the following non-convex optimization problem when \mathbf{A} fulfills certain requirements [70]: $\min \|\mathbf{z}\|_0$ s.t. $\mathbf{y} = \mathbf{A}\mathbf{z}$ with the ℓ_0 -norm $\|\cdot\|_0$ counting a vector's non-zero entries. In practice, tractable reconstruction algorithms need to be applied on noisy data. When replacing the ℓ_0 - with the convex ℓ_1 -norm

$$\|\mathbf{z}\|_1 = \sum_i |z_i|, \quad (3.10)$$

computationally feasible algorithms can be used for approximate solutions: $\min \|\mathbf{z}\|_1$ s.t. $\|\mathbf{y} - \mathbf{A}\mathbf{z}\|_2^2 < \epsilon$, with ϵ controlling data fidelity and is normally set at the noise level.

Based on [71, 72], Lustig et al. [73] adapted this concept of compressed sensing (CS) for MRI by ℓ_1 -regularizing the inversion of incomplete k-space measurements. If the object \mathbf{p} has a sparse representation in a linear transform domain, $\mathbf{\Psi}\mathbf{p}$, and the undersampling pattern leads to incoherent (noise-like) artifacts in the image and sparse domain, the object can be recovered by solving the unconstrained minimization problem

$$\arg \min_{\mathbf{p}} \|\mathbf{d} - \mathbf{E}\mathbf{p}\|_2^2 + \lambda \|\mathbf{\Psi}\mathbf{p}\|_1. \quad (3.11)$$

Depending on the imaging experiment, $\mathbf{\Psi}$ implements e.g. a discrete Wavelet, anisotropic total variation (TV), identity or temporal FT operation. Noise and incoherent artifacts are then removed

by the sparsity-seeking ℓ_1 -norm which suppresses noise-like contributions from small coefficients while maintaining the significant signal components. The non-linear conjugate gradient (CG) solver in [73] approximates the non-differentiable sum in (3.11) by $\|\Psi\boldsymbol{\rho}\|_1 \approx \boldsymbol{\rho}^H \Psi^H \mathbf{W}^{-1} \Psi \boldsymbol{\rho}$, with the real-valued diagonal matrix

$$\mathbf{W} = \text{diag}\left(\sqrt{(\Psi\boldsymbol{\rho})^* \circ (\Psi\boldsymbol{\rho}) + \boldsymbol{\kappa}}\right), \quad (3.12)$$

where the complex conjugate $(\cdot)^*$, the square root and the multiplication \circ denote element-wise vector operations. $\boldsymbol{\kappa}$ adds a small positive constant to each component. The gradient update during CG iterations is then calculated according to $\nabla\|\Psi\boldsymbol{\rho}\|_1 \approx 2\Psi^H \mathbf{W}^{-1} \Psi \boldsymbol{\rho}$. Using iterative reweighted least squares (IRLS) algorithms [74], the following problem which is quadratic in $\boldsymbol{\rho}$ is solved:

$$\boldsymbol{\rho}^{k+1} = \arg \min_{\boldsymbol{\rho}} \|\mathbf{d} - \mathbf{E}\boldsymbol{\rho}\|_2^2 + \frac{\lambda}{2} \boldsymbol{\rho}^H \Psi^H \mathbf{W}_k^{-1} \Psi \boldsymbol{\rho}, \quad (3.13)$$

with \mathbf{W}_k being the diagonal matrix evaluated at $\boldsymbol{\rho}^k$. The factor 1/2 origins from an auxiliary function defining an upper bound for the ℓ_1 terms, i.e. minimizing (3.13) for $k \rightarrow +\infty$ also minimizes (3.11). The above update can then be calculated by running a few CG iterations inverting $[\mathbf{E}^H \mathbf{E} + (\lambda / 2) \Psi^H \mathbf{W}_k^{-1} \Psi] \boldsymbol{\rho} = \mathbf{E}^H \mathbf{d}$. Unitary transforms ($\Psi^H \Psi = \mathbf{I}_N$) allow using iterative shrinkage-thresholding algorithms (ISTAs) [75-77] which can be decomposed into a line search step along the gradient of the convex data fidelity term, followed by a sparsity-promoting operation in the transform domain:

$$\boldsymbol{\rho}^{k+1} = \Psi^H S_{\lambda\tau/2} \left(\Psi \left[\boldsymbol{\rho}^k + \tau \mathbf{E}^H (\mathbf{d} - \mathbf{E}\boldsymbol{\rho}^k) \right] \right). \quad (3.14)$$

$S_i(x_i) = \max(|x_i| - t, 0) \text{sgn}(x_i)$ is the soft-thresholding function acting on the vector elements x_i and τ is a step size parameter.

Combining PI or dynamic imaging with the CS reconstruction formalism is straightforward [23, 78, 79]. Originally, most linear operators Ψ rely on fixed analytic transforms, which is only as good as the underlying mathematical model, and thus, can implement too rigid priors. Recent research focusses on more flexible data-adaptive sparse representations based on structural similarity of image patches [80, 81], coefficient support structure [82] or dictionary learning [83].

3.3 Dynamic Imaging

In dynamic imaging, k -space data were collected for different time points t , thereby spanning a so-called k - t space. Time-interleaved Cartesian and non-Cartesian undersampling introduces coherent or incoherent aliasing in the spatial and temporal frequency domain (x - f space). Undersampling artifacts in x - f space may be removed by linear or non-linear methods exploiting temporal correlations in an object series signal representation. Assuming that only minor parts within the image undergo rapid changes, the support of the dynamic object in the x - f domain is sparse and/or tightly packed.

Linear Cartesian reconstruction schemes like k - t SENSE [84] or k - t GRAPPA [85] acquire a fully sampled center of k - t space (either separated from or simultaneously with the actual data scan) for training or calibration data together with time-interleaved regularly skipped phase encoding lines (Figure 3.3). While k - t GRAPPA directly exploits signal correlations in k - t space by extending the GRAPPA kernel along the time axis, k - t SENSE reconstructs an unfolded x - f space vector \mathbf{p} by

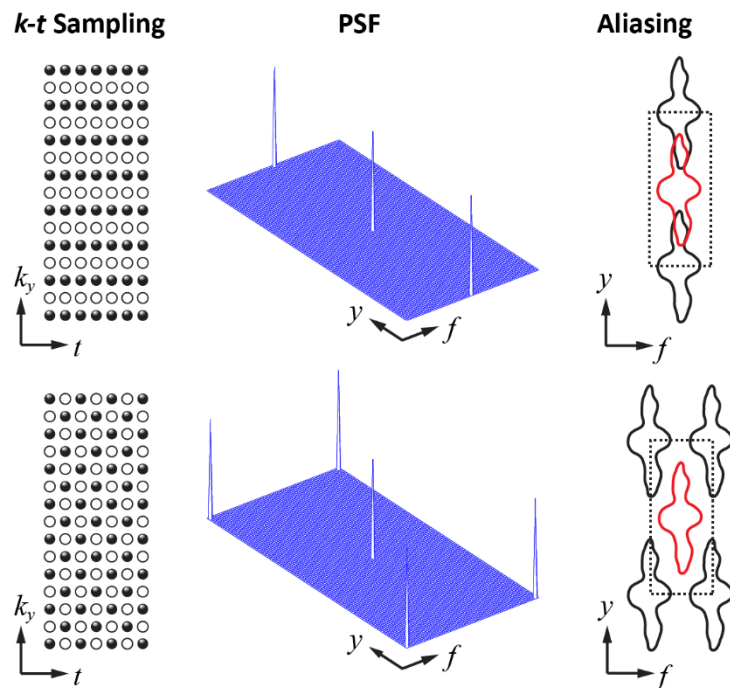


Figure 3.3 Regular 2D k - t undersampling leads to superimposing equidistant (separated by FOV_y / R) aliases of the spectral y - f support along the phase encoding axis (top). Coherent aliasing can be reduced using time-interleaved undersampling shifting aliases additionally along the temporal frequency axis according to the PSF (bottom). Figure adapted from [84].

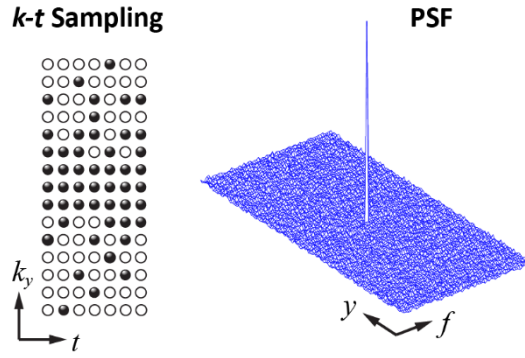


Figure 3.4 Illustration of time-interleaved 2D Cartesian variable-density random undersampling and a PSF revealing incoherent aliasing in the x - f space along the phase encoding and temporal frequency direction.

exploiting prior knowledge about the signal covariance $\Theta_{xf} = \overline{\mathbf{p}\mathbf{p}^H}$ and reduced aliasing due to sheared point-spread function (Figure 3.3):

$$\arg \min_{\mathbf{p}} (\mathbf{d} - \mathbf{E}\mathbf{p})^H \Theta_{kt}^{-1} (\mathbf{d} - \mathbf{E}\mathbf{p}) + \lambda \mathbf{p}^H \Theta_{xf}^{-1} \mathbf{p}, \quad (3.15)$$

with the noise covariance matrix Θ_{kt} , $\mathbf{E} = (\mathbf{I}_{N_c} \otimes \mathbf{F}_u) \mathbf{S} \mathbf{F}_t^H$ and the temporal FT \mathbf{F}_t . In practice, Θ_{xf} is approximated by the diagonal matrix \mathbf{M}_{xf}^2 containing the squared estimated signal magnitude from training data. Higher acceleration factors can be achieved by projecting the frequency distributions on a number of principle components derived from a principle component analysis (PCA) of the training data [86]. This constraint reduces the number of unknowns and better temporal fidelity is achieved. The object vector to be reconstructed contains the x - pc space coefficients, the encoding matrix is extended with the operator $\mathbf{B}_{pc \rightarrow f}$ implementing the transform from x - pc to x - f space, $\mathbf{E} = (\mathbf{I}_{N_c} \otimes \mathbf{F}_u) \mathbf{S} \mathbf{F}_t^H \mathbf{B}_{pc \rightarrow f}$, and the covariance matrix refers to the x - pc domain: Θ_{xpc} or \mathbf{M}_{xpc}^2 . Non-Cartesian implementations of k - t GRAPPA and k - t SENSE have been demonstrated in [21, 22].

Time-interleaved Cartesian variable-density random or non-Cartesian undersampling additionally spreads aliasing along the time and temporal frequency axis (Figure 3.4), respectively [78]. When the x - f signal support is sufficiently sparse, non-linear reconstruction can remove the incoherent artifacts using algorithms presented in Section 3.2:

$$\arg \min_{\mathbf{p}} \|\mathbf{d} - \mathbf{E}\mathbf{p}\|_2^2 + \lambda \|\mathbf{F}_t \mathbf{p}\|_1, \quad (3.16)$$

with the object vector \mathbf{p} containing the x - t image series. Other sparsifying transforms are based

on temporal derivatives [87, 88], PCA [11, 89, 90] or reordering schemes [91, 92]. Data-adaptive transforms exploit global or local low-rank structures [93-95], structure of coefficient support [96] or dictionary learning [97].

3.4 Motion

Motion compensation techniques are invaluable to reduce breathing artifacts, scan times, or to increase spatio-temporal resolution in cardiovascular MRI. Data acquisition over multiple heart and respiratory cycles makes measurements sensitive to motion. Thus, combining k-space profiles from multiple motion cycles can lead to inconsistencies in the encoding model resulting in ghosting or blurring artifacts in the reconstructed image due to periodic respiratory or random motion [98, 99]. This section provides a brief overview of current motion correction methods in thoracic and abdominal imaging.

3.4.1 Affine Motion

When excited spin distributions are not congruent with the reference positions during k-space profile readouts, mismatch occurs between encoded and actual object positions. Affine motion is a model allowing for analytical relations between image deformation and corresponding effects in k-space. After affine transformation, each position vector \mathbf{r} in the imaging volume is mapped according to $\mathbf{T}\mathbf{r} + \delta\mathbf{r}$, with $\mathbf{T} \in \mathbb{R}^{3 \times 3}$ and translation vector $\delta\mathbf{r} \in \mathbb{R}^3$. Rigid motion implies \mathbf{T} being orthogonal: $\mathbf{T}^T = \mathbf{T}^{-1}$. The k-space signal model is then affected according to

$$\begin{aligned} d(\mathbf{k}) &= \int_V c(\mathbf{T}\mathbf{r} + \delta\mathbf{r})\rho(\mathbf{T}\mathbf{r} + \delta\mathbf{r})e^{-i\mathbf{k}\cdot\mathbf{r}} d\mathbf{r} \\ &= \left(\int_V c(\mathbf{r})\rho(\mathbf{r})e^{-i((\mathbf{T}^{-1})^T\mathbf{k})\cdot\mathbf{r}} d\mathbf{r} \right) e^{i((\mathbf{T}^{-1})^T\mathbf{k})\cdot\delta\mathbf{r}} = d((\mathbf{T}^{-1})^T\mathbf{k})e^{i((\mathbf{T}^{-1})^T\mathbf{k})\cdot\delta\mathbf{r}}, \end{aligned} \quad (3.17)$$

i.e. elementary affine transformations such as translation lead to a linear phase ramp in k-space according to the Fourier shift theorem, a rotation in image remains the same rotation in k-space, and an expansion becomes a contraction and vice versa.

3.4.2 Motion Compensation

Cardiac motion artifacts can be minimized by separately collecting k-space profiles for short time intervals which are synchronized with the cardiac cycle using an electro-cardiogram (ECG).

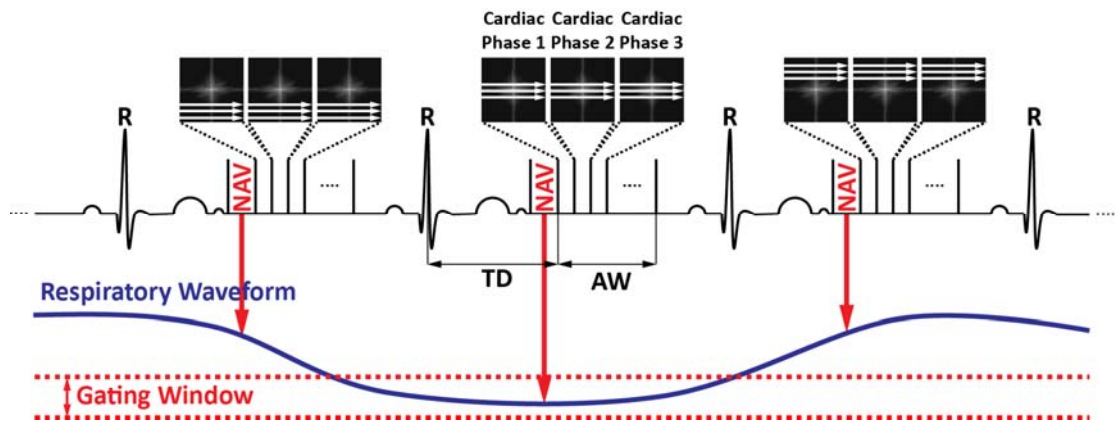


Figure 3.5 Illustration of cardiac and respiratory gating (TD: trigger delay, AW: acquisition window). Each heart phase's k-space profile acquisition is distributed over multiple heart beats and R-R intervals, respectively. Data are only accepted if the respiratory motion related NAV signal is within the gating window.

Depending on the width and relative position with respect to the ECG R-wave, the corresponding cardiac phases can be resolved. When collecting data over the full cardiac cycle, the profiles are then retrospectively binned (relative to the recorded R-waves) into cardiac phases [100]. If no reliable ECG signal is available, cardiac self-gating methods assessing an ECG surrogate signal from repeatedly collected profiles may be used [27, 101].

Respiratory motion suppression by breath-holding is widely used [102, 103], but its use is limited in non-compliant patients, in case of breath-hold drifts or if breath-hold durations are a concern. The latter can be counteracted in conjunction with k-space undersampling techniques. In case scan times exceed a patient's breath-hold capability, free-breathing acquisitions using pro- or retrospective motion correction are warranted.

Using prospective motion compensation methods, motion information is estimated during the scan to correct for corruption in real-time. For example, navigators (NAVs) monitor the movement of the lung-liver interface which is assumed to be linearly correlated with the position of the heart [102]. When the NAV signal falls within an acceptance window, the acquired data within the corresponding heart beat are accepted (Figure 3.5). Until acceptance of a profile, rejected profiles need to be resampled in the subsequent heart beats. For an acceptance window of 5mm width, scan time can be prolonged by a factor between 2 and 3 in practice. To address the limited gating efficiency, k-space position dependent gating approaches [104] may be used to allow for larger gating window widths for higher phase encoding lines where artifacts are less pronounced as compared to the lower spatial frequencies. Phase encode reordering [105] reduces ghosting artifacts by prospectively encoding k-space profiles according to the NAV

position, and thus, the periodicity of the respiratory motion over the sampling scheme is reduced. In general, the NAV excitation pulse is interleaved with the imaging sequence and the quality of the gating signal depends on the field strength [106]. In contrary, respiratory belt-based gating [107, 108] provides a continuous and field strength independent signal from a pressure sensor placed around the chest wall measuring its extension during respiration. A drawback is that the positioning of the belt can affect the linearity of the correlation between chest and heart's movement [109]. Self-gating methods [101, 110] extract the gating signal from sampled k-space profiles, interleaved or simultaneously acquired with the imaging sequence, and thus, do not rely on external sensors. Heart motion can be tracked directly, and therefore, does not depend on linear models between diaphragm and heart position which can be inaccurate because of patient-specific correlation factors [111] or heart-diaphragm hysteresis [112]. Slice or volume tracking methods [113, 114] modify the RF pulses and imaging gradients after the NAV signal. Affine motion correction with a patient-specific motion model trained on three 1D NAVs has shown significant error reduction in free-breathing coronary angiography [115]. Since the motion model parameters are trained on a reduced region of interest (ROI) in a separate calibration scan, while motion compensation is applied globally, artifacts originating from outside the ROI cannot be captured, and the model fails when breathing patterns deviate between the actual and the calibration scan.

Retrospective compensation strategies are designed to reduce artifacts during image reconstruction of motion-corrupted data. When models are restricted to translational, rotational or affine motion, profiles can be corrected according to (3.17). Motion model parameters may be extracted from radial profiles [116, 117], low-resolution images obtained during startup cycles before the acquisition window [114, 118] or from data densely sampled in the k-space center [119, 120], binning data to different respiratory positions [25, 121-123], or changes in coil sensitivity profiles [124]. General non-rigid motion has been approximated by locally restricted analytical motion models [125-127].

3.4.3 Matrix Formalism for General Motion Model

A reconstruction framework for retrospective motion correction incorporating a matrix description of general non-rigid motion has been proposed in [128]. The linear encoding model (3.1) is extended with an operator $\mathbf{T} \in \mathbb{R}^{N_{ms} \times N}$ describing the spatial deformation of the reconstructed image in a reference respiratory position relative to the motion states ($i = 1, \dots, N_{ms}$)

during the data acquisition:

$$\mathbf{d} = \mathbf{E}\mathbf{T}\boldsymbol{\rho} + \boldsymbol{\eta} = \begin{bmatrix} \mathbf{E}_1 & \dots & \mathbf{0} \\ \vdots & \ddots & \vdots \\ \mathbf{0} & \dots & \mathbf{E}_{N_{ms}} \end{bmatrix} \begin{bmatrix} \mathbf{T}_1 \\ \vdots \\ \mathbf{T}_{N_{ms}} \end{bmatrix} \boldsymbol{\rho} + \boldsymbol{\eta}, \quad (3.18)$$

Given the 2D or 3D spatial transformation fields $\mathbf{u}_i(\mathbf{r})$ and assuming that the entries of the deformation matrix can be extracted from acquired profiles, a motion-corrected image can be reconstructed by using standard numerical algorithms for inversion of the modified forward encoding model. The \mathbf{T}_i 's then spatially align $\boldsymbol{\rho}$ to the motion states via bi- or trilinear interpolation: $\rho_i(\mathbf{r}) = T_i(\rho) = \rho(\mathbf{r} + \mathbf{u}_i(\mathbf{r}))$. Figure 3.6 depicts the principle of general non-rigid linear transformation with an illustrative deformation of a 2D brain image. This motion matrix formalism has already been combined with SENSE-based PI [120, 129-131], k - t PCA [132] and CS [25].

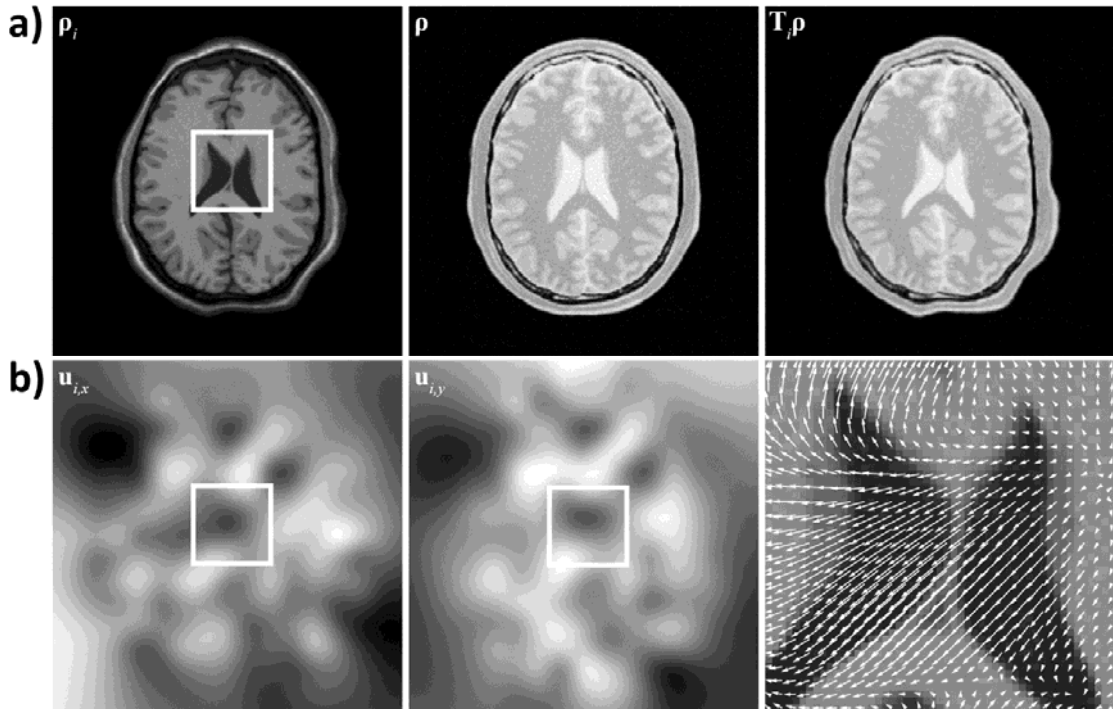


Figure 3.6 a) Reference image ($\boldsymbol{\rho}$) is transformed ($\mathbf{T}_i \boldsymbol{\rho}$) to the motion state ($\boldsymbol{\rho}_i$) using the linear operator \mathbf{T}_i . b) 2D displacement field components (describing spatial deformation of $\boldsymbol{\rho}_i$ to $\boldsymbol{\rho}$) obtained by non-rigid image registration are superimposed onto $\boldsymbol{\rho}$. Brain data set was provided by elastix.isi.uu.nl.

Chapter 4

Radial k - t SPIRiT: Auto-Calibrated PI for Generalized PC MRI*

4.1 Introduction

Sensitivity encoding (SENSE) [56] and generalized auto-calibrating partially parallel acquisitions (GRAPPA) [10] are the most widely used and commercially available parallel imaging (PI) reconstruction methods among various other techniques [133-139]. Accurate coil sensitivity estimation is essential for SENSE reconstruction quality which can be hampered by misregistration errors between calibration and actual scan (e.g., due to respiratory or bulk motion), field of view (FOV) limitations [60, 61], or regions with low spin density [62]. In contrast, GRAPPA is an auto-calibrating PI method extracting coil sensitivity information from fully sampled calibration lines of the actual scan. The missing data for each coil are separately synthesized by means of a shift-variant k -space interpolation scheme whose weights are fitted to a fully sampled calibration area. Misregistration errors, difficulties with accurate coil sensitivity estimation and FOV limitations can thus be avoided or reduced. However, for GRAPPA reconstruction techniques, the inclusion of non-Cartesian trajectories [66, 68, 140, 141] needs approximations and is not as straightforward as in SENSE [59]. Dynamic PI methods such as TSENSE [142], TGRAPPA [143], or k - t SENSE [84] exploit temporally averaged calibration or spatio-temporal correlations, but may suffer from temporal filtering effects caused by signal nulling or errors in sensitivity maps [144].

* Published in: C. Santelli, T. Schaeffter and S. Kozerke, "Radial k - t SPIRiT: Autocalibrated Parallel Imaging for Generalized Phase-Contrast MRI", *Magnetic Resonance in Medicine*, vol. 72(5), pp. 1233-1245, 2014.

Recently, iterative self-consistent PI reconstruction (SPIRiT) generalizing GRAPPA has been proposed [23]. Correlated k-space data are reconstructed iteratively with a full and shift-invariant interpolation kernel enforcing self-consistency with calibration data for arbitrary sampling trajectories. The inclusion of prior knowledge by means of additional regularization terms offers a general reconstruction formalism similar to SENSE. Relative to GRAPPA, better reconstruction accuracy and noise behavior have been shown [23]. Additionally, using low-rank matrix completion, the SPIRiT calibration data can be reconstructed from a partially sampled calibration area [145, 146]. A non-linear k - t SPIRiT method exploiting Wavelet-domain sparsity in conjunction with ℓ_1 -norm minimization has also been proposed [92]. In that study, the SPIRiT kernel was derived from a time-averaged center of k-space, and thus, only signal correlations along the spatial encodes were used.

Acceleration by data undersampling is needed in time-resolved flow encoded phase-contrast (PC) MRI to achieve appropriate spatio-temporal resolution within an acceptable scan time [9-11, 147-156]. Radially acquired one-directional through-plane PC measurement for aortic flow volume quantification has been combined with non-linear temporally constrained reconstruction regularizing first- or second-order temporal derivatives [88, 157].

While PC assesses mean velocity, Fourier velocity encoding (FVE) [8, 158] is a technique, which resolves the distribution of velocities within a voxel by adding another encoding dimension along the velocity direction (k_v). For this, the velocity encoding gradients are varied to obtain a range of k_v -points, i.e., different first moments $k_v(t) = \gamma \int_0^t G(\tau) \tau d\tau$. However, due to the large number of encodings, scan time becomes critical. One major advantage of FVE is that it allows for quantification of both mean velocities and turbulence [12]. It has been shown that turbulent kinetic energy (TKE) maps can also be calculated from undersampled velocity-encodings assuming Gaussian distributed velocity spectra [12]. Originally, a standard PC k_v -sampling scheme has been proposed requiring estimation of velocity standard deviations (SDs) to find optimal k_v -points potentially causing mean velocity phase wrapping. By sampling multiple k_v -points, phase wrapping can be avoided and sensitivity is increased for a wide range of velocities [159, 160]. However, this multi-point velocity encoding scheme prolongs scan time further.

In this work, following the principle of k - t GRAPPA [85], we propose to extend non-Cartesian SPIRiT to include the temporal dimension thereby additionally exploiting temporal correlations in k - t space. The performance of this linear ℓ_2 -norm minimizing k - t method relative to frame-by-frame SPIRiT and auto-calibrated radial k - t GRAPPA [22] reconstruction is evaluated based on

simulated and prospectively undersampled radial two-dimensional (2D) in vivo multi-point PC aortic flow measurements.

4.2 Theory

The basic SPIRiT formalism [23] enforces data and calibration consistency. The latter exploits coil sensitivity dependent signal correlations by expressing a Cartesian k-space sample, independently if acquired or not, as a linear combination of k-space points in a full neighborhood across all coils. Accordingly, a coupled system of linear equations $\mathbf{d}_c = \mathbf{G}\mathbf{d}_c$ is used, with vector \mathbf{d}_c containing the Cartesian k-space data of all channels and the operator \mathbf{G} defining a shift-invariant interpolation scheme. The weights of \mathbf{G} are fitted to a fully sampled centre of k-space, termed calibration area. Arbitrary sampling trajectories are incorporated by the data consistency term $\mathbf{d} = \mathbf{E}_k\mathbf{d}_c$ relating the reconstructed Cartesian k-space to the acquired signal \mathbf{d} using the linear operator \mathbf{E}_k . For Cartesian acquisition this becomes an operation simply selecting the acquired k-space points out of \mathbf{d}_c , whereas for non-Cartesian sampling \mathbf{E}_k represents a regridding matrix. The reconstruction process is then formulated as the following unconstrained Lagrangian minimization problem:

$$\arg \min_{\mathbf{d}_c} \|\mathbf{d} - \mathbf{E}_k\mathbf{d}_c\|_2^2 + \lambda^2 \|(\mathbf{G} - \mathbf{I})\mathbf{d}_c\|_2^2, \quad (4.1)$$

with the regularization parameter λ trading data and calibration consistency, and identity matrix \mathbf{I} originating from the constraint $\mathbf{G}\mathbf{d}_c - \mathbf{d}_c = \mathbf{0}$. Using an iterative solver for problem (4.1), each coil's full k-space is re-synthesized from the k-space in the previous iteration step. In contrast, GRAPPA non-iteratively synthesizes missing k-space from the acquired data, and therefore, uses a shift-variant interpolation kernel; its weights depend on the relative positions of the sampled k-space points to the target locations comprising only non-acquired points to be interpolated.

Dynamic MR data are acquired in k - t space. Similar to k - t GRAPPA extending GRAPPA for dynamic imaging, SPIRiT is extended to this higher-dimensional k - t space to additionally exploit temporal correlations. For this purpose the calibration consistency operator \mathbf{G} in (4.1) is modified to include the temporal neighborhood of a Cartesian k-space sample. Accordingly, every Cartesian k - t point, whether sampled or not, is represented as a weighted sum of k - t points within a predefined full neighborhood over all coils and adjacent time frames (Figure 4.1a). Adapting \mathbf{E}_k leads to a linear mapping of the reconstructed Cartesian k - t space over all coils \mathbf{d}_c to a dynamic sampling trajectory \mathbf{d} (Figure 4.1b). The weights of the interpolation kernels in \mathbf{G} are again fitted to a fully sampled k - t calibration area by means of the calibration matrix \mathbf{A} stacking row by row

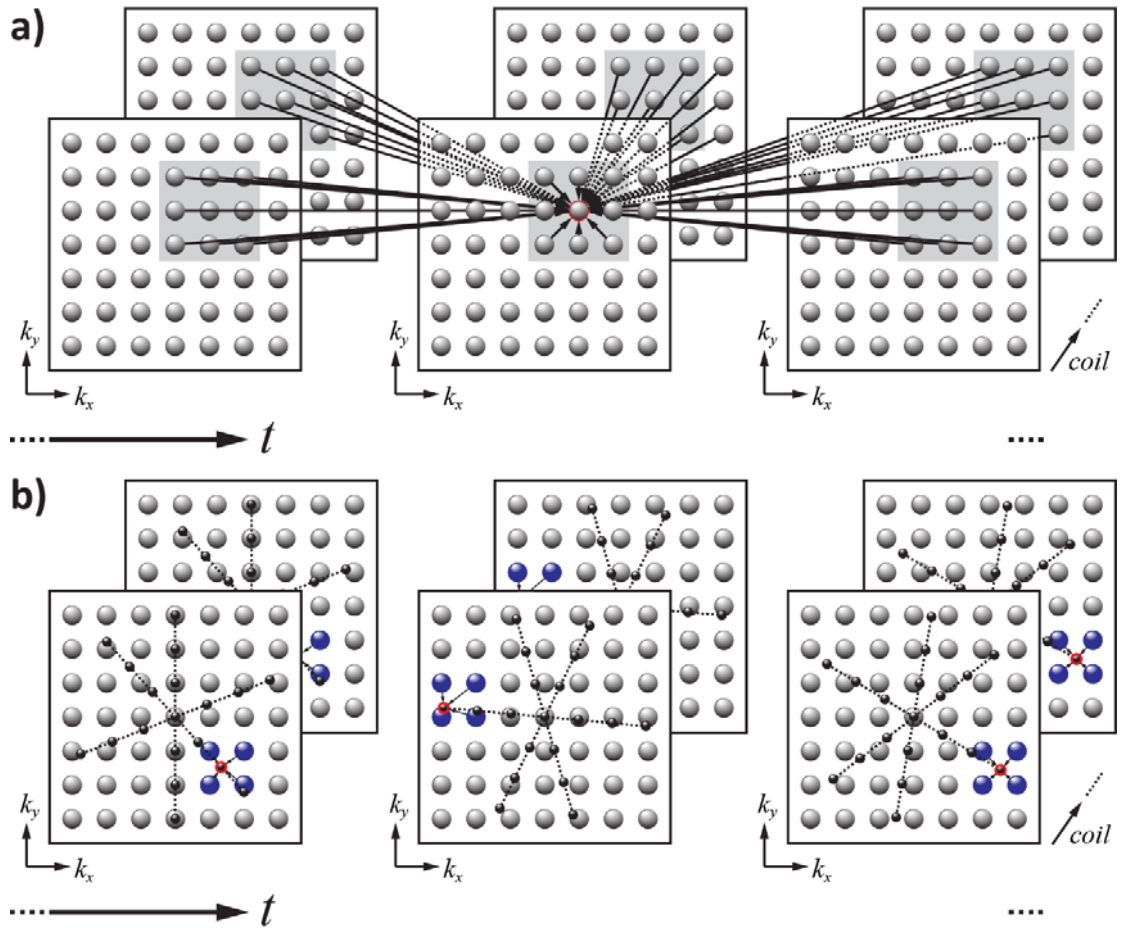


Figure 4.1 a) Schematics of k - t SPIRiT. Every Cartesian k - t sample point is expressed as a linear combination of neighboring points in dynamic k - t space across all coils. The corresponding weights are indicated by the arrows. Calibration consistency for every Cartesian k - t space point is enforced over a full neighborhood (grey blocks) including acquired and non-acquired Cartesian samples. **b)** Illustration of Golden angle (GA) sampling providing an optimal distribution of radial profiles over time. Data consistency with non-Cartesian sampling is accomplished by regridding the reconstructed points on the sampling trajectory.

vectorized k - t space data blocks (across all coils) containing target and source points. The data blocks are shifted in a row-by-row manner over the calibration area. Accordingly, adjacent rows correspond to overlapping k - t blocks. The coil specific convolution kernels \mathbf{g}_i , $i = 1, \dots, N_c$, assembling \mathbf{G} are then estimated by solving the following Tikhonov regularized least-squares problem:

$$\arg \min_{\mathbf{g}_i} \left\| \mathbf{d}_i^t - \mathbf{A}_i \mathbf{g}_i \right\|_2^2 + \lambda_{calib,i}^2 \left\| \mathbf{g}_i \right\|_2^2, \quad (4.2)$$

with vector $\mathbf{d}_i^t = \mathbf{A}\mathbf{e}_i$ containing the target points within the calibration area of coil i , and $\mathbf{A}_i = \mathbf{A}\mathbf{I}_i^T$ the corresponding reduced calibration matrix whose rows are composed of the vectorized source points (\mathbf{e}_i : as defined in (3.6), \mathbf{I}_i : sampling matrix that extracts the source points corresponding to \mathbf{g}_i from a vectorized full k -space data block). $\lambda_{calib,i}$ can be determined using the L-curve method [161]. For reconstruction, the functional (4.1) with modified operators and data vectors is minimized using a conjugate gradient (CG) solver for the equivalent problem:

$$\arg \min_{\mathbf{d}_c} \left\| \begin{bmatrix} \mathbf{E}_k \\ \lambda(\mathbf{G} - \mathbf{I}) \end{bmatrix} \mathbf{d}_c - \begin{bmatrix} \mathbf{d} \\ \mathbf{0} \end{bmatrix} \right\|_2^2. \quad (4.3)$$

Multiplying the vector difference with matrix $[\mathbf{E}_k^H \ \lambda(\mathbf{G} - \mathbf{I})^H]$ corresponds to solving the normal equation of the least-squares problem in expression (4.3). Because \mathbf{G} also represents convolutions in k - t space followed by appropriate summations over all coils, it can be equivalently implemented by point-wise multiplications with the IFT of the corresponding kernels in the x - f domain. Therefore, the dynamic multi-coil image $\boldsymbol{\rho}$ in x - f space can efficiently be reconstructed by solving:

$$[\mathbf{E}^H \mathbf{E} + \lambda^2 (\mathbf{G}_{xf} - \mathbf{I})^H (\mathbf{G}_{xf} - \mathbf{I})] \boldsymbol{\rho} = \mathbf{E}^H \mathbf{d}, \quad (4.4)$$

with the modified data and calibration consistency operators \mathbf{E} and \mathbf{G}_{xf} , respectively. \mathbf{E} then maps the object in x - f space to the measured trajectory in k - t space.

4.3 Methods

4.3.1 Data Acquisition

Free-breathing navigator-gated fully sampled 2D gradient-echo radial cine FVE data with three-directional velocity encoding were acquired in the aortic arch of 11 healthy volunteers on a 3 Tesla (T) Philips Achieva scanner (Philips Healthcare, Best, The Netherlands) using a six-element cardiac receive array. The FOV was set to 250 x 250 mm² with a voxel size of 2 x 2 x 10 mm³. Data for three different first gradient moments corresponding to encoding velocities of 50 cm/s, 100 cm/s and 200 cm/s were acquired in addition to a reference data set ($k_v = 0$). For three-directional velocity mapping, this amounts to 10 k_v -point sampling: 3 k_v -points for each direction, plus the reference image (Figure 4.2a). For k - t SPIRiT, simulated undersampled radial data sets were obtained by separately regridding these 10-point measurements onto GA profiles [38] rotated by $(0.5\pi N / R)\Delta\phi_{GA}$ (N : image matrix dimension, R : undersampling factor relative to radial Nyquist,

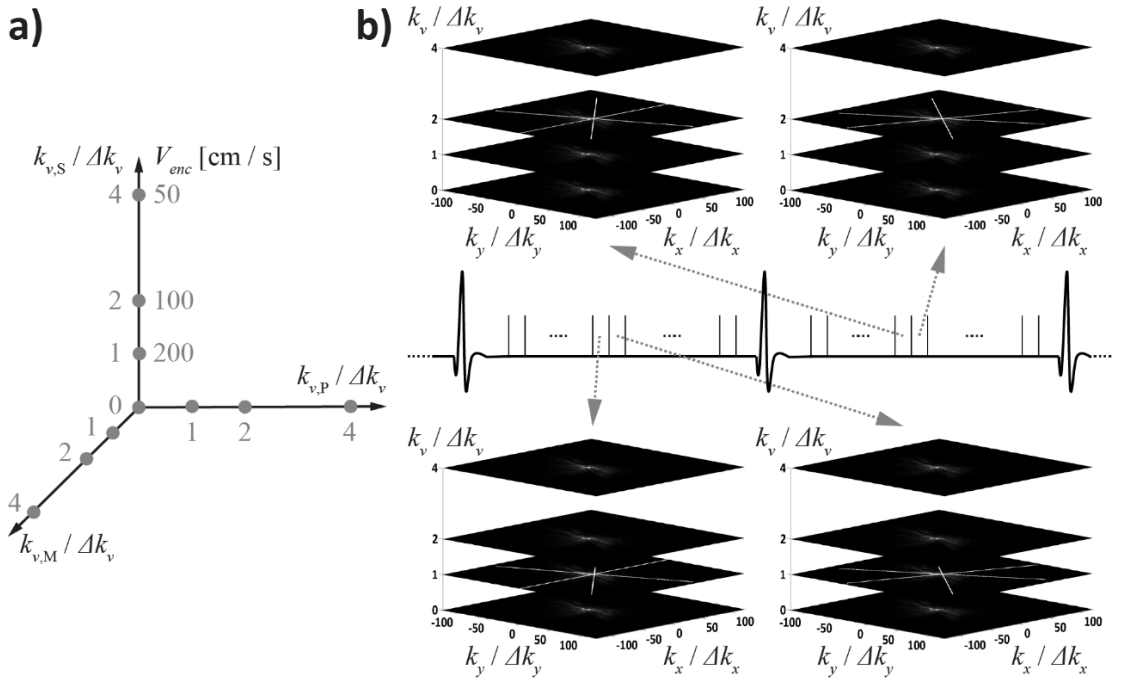


Figure 4.2 a) Illustration of 10-point k_v -space sampling ($\Delta k_v = \pi / (200 \text{ cm/s})$). Three orthogonal directions in the measurement coordinate system (M-P-S) are flow encoded. **b)** Stack of GA radials cine sampling trajectory for a velocity encoded direction ($\Delta k_v = \pi / (200 \text{ cm/s})$, $\Delta k_x = \Delta k_y = 1 / \text{FOV}$).

$\Delta\varphi_{GA} = 111.25^\circ$) between adjacent cardiac phases (Figure 4.2b). For standard frame-by-frame SPIRiT reconstruction, regridding on equally spaced projections was performed. For comparison with self-calibrated radial k - t GRAPPA [22], regridding on time-interleaved equally spaced projections was used, s.t. each k -space position was sampled in every R -th time frame.

A time-interleaved GA sampling scheme was implemented for prospective undersampling and SPIRiT-based reconstruction. A fully sampled data set was acquired in a healthy volunteer. Prospective undersampling by a factor of R was realized by retaining the first $0.5\pi N / R$ projections in each heart phase.

4.3.2 Image Reconstruction

Each velocity encoded image was reconstructed separately with a 7×7 k_x - k_y and $7 \times 7 \times 3$ k_x - k_y - t neighborhood for frame-by-frame and k - t SPIRiT, respectively. The 7×7 extension in k_x - k_y direction was chosen according to [23] for a good trade-off between reconstruction convergence and accuracy. Based on simulations, a temporal interpolation window width of 3 was found to be optimal for magnitude and velocity reconstruction. The appropriate kernel weights were calculated from a $30 \times 30 \times$ (no. of cardiac phases) calibration area from the data

($k_v = 0$) corresponding roughly to $1/8 \times 1/8$ of the acquisition matrix dimension (248×248). For each undersampled data set ($R = 2, 4, 6, 8, 10, 12, 14$), the calibration area for each heart phase was synthesized by means of structured low-rank matrix completion [146] (Figure 4.3). For an oversampled center of k-space ($R = 2, 4, 6, 8$), this step is theoretically redundant, but was found to provide improved results in practice due to noise reduction. The iterative algorithm alternates between singular value decomposition (SVD) thresholding of each heart phase's calibration matrix and averaging of matrix entries referring to the same k-space location, imposing low rank and Hankel structure, respectively. Data consistency of an updated Cartesian calibration data estimate was enforced by interpolating it onto the non-Cartesian trajectory and subtracting the gridded residual from the current estimate. $\lambda_{calib,i}$ in (4.2) were calculated for each experiment separately with the L-curve method using the SVDs of source point matrices \mathbf{A}_i . Then, the interpolation weights \mathbf{g}_i were directly obtained by means of the SVD matrices and $\lambda_{calib,i}$. The regularization parameter λ for image reconstruction was empirically set to 0.125 and 0.25 for simulated and prospective undersampling, respectively. For k - t GRAPPA reconstruction, projections were reordered in a hybrid (φ, k_r, t) -space (φ, k_r : polar coordinates of projections) [66]. The readout direction (k_r) was divided into equally spaced segments of width 8 which were then separately reconstructed using $2 \times 3 \times 2$ Cartesian k - t GRAPPA kernels: each missing k-space line was interpolated from the two neighboring acquired lines along azimuthal and temporal direction with a kernel size of 3 along the readout direction. For interpolation weight estimation, kernels were shifted along all (φ, k_r, t) -space dimensions over the calibration data ($k_v = 0$) generated according to [22].

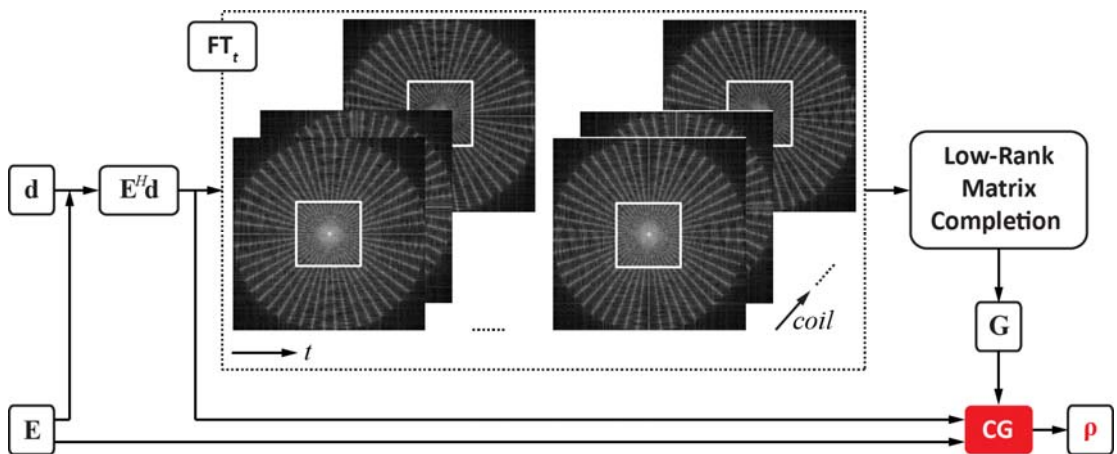


Figure 4.3 k - t SPIRiT reconstruction workflow. The calibration operator \mathbf{G} is calculated from the center of k - t space obtained by structured low-rank matrix completion before it is passed on to the CG solver.

From the resulting coil-combined image series, $\rho(\mathbf{r}, t, k_v)$, mean velocity $v_m(\mathbf{r}, t)$ and SD $\sigma_v(\mathbf{r}, t)$ at position \mathbf{r} and frame t were calculated for each velocity encoded direction according to $\rho(\mathbf{r}, t, k_v) / \rho(\mathbf{r}, t, 0) = \exp(-0.5\sigma_v(\mathbf{r}, t)^2 k_v^2 - iv_m(\mathbf{r}, t)k_v)$ and equation (2.32), respectively [12]. Magnitude images were combined using a sum-of-squares approach, while velocity induced phase was calculated with a magnitude weighted sum of phase differences [162]. $\sigma_v(\mathbf{r}, t)$ was fitted to $|\rho(\mathbf{r}, t, k_v)| / |\rho(\mathbf{r}, t, 0)|$ for all $k_v \neq 0$ in a standard least-squares sense. Turbulence intensity maps were then derived according to [163]. Following standard PC processing, $v_m(\mathbf{r}, t)$ was assessed by taking the phase of the complex valued ratio $\rho(\mathbf{r}, t, k_v) / \rho(\mathbf{r}, t, 0)$ for $k_v / \Delta k_v = 1$ and $k_v / \Delta k_v = 2$ allowing for two- and three-point velocity estimation [164]. For the three-point method, the velocity was estimated using a weighted least-squares fit to the two unwrapped phase maps. The weighting matrix was assessed according to $k_v \exp(-0.5\sigma_v(\mathbf{r}, t)^2 k_v^2)$ [160].

4.3.3 Data Analysis

Reconstruction accuracy of simulated undersampled data was measured using the temporally resolved and overall root-mean-square error (RMSE) over a region of interest (ROI):

$$RMSE_t = \sqrt{\frac{\sum_{i \in ROI_t} |r_{t,i} - o_{t,i}|^2}{\sum_{i \in ROI_t} |o_{t,i}|^2}} \quad \text{and} \quad RMSE = \sqrt{\frac{\sum_t \sum_{i \in ROI_t} |r_{t,i} - o_{t,i}|^2}{\sum_t \sum_{i \in ROI_t} |o_{t,i}|^2}}, \quad (4.5)$$

where $r_{t,i}$ and $o_{t,i}$ denote the i -th pixel value of the reconstructed and the fully sampled reference measure in the dynamic ROI_t , respectively. r and o can represent image magnitude or SD. A magnitude weighted RMSE metric was used to measure mean velocity reconstruction performance by reducing the impact from random phase variations due to low signal magnitude [154]:

$$RMSE_v = \sqrt{\frac{\sum_t \sum_{i \in ROI_t} \left(\frac{r_{t,i} + o_{t,i}}{2} (v_{t,i}^r - v_{t,i}^o) \right)^2}{\sum_t \sum_{i \in ROI_t} (o_{t,i} v_{t,i}^o)^2}}. \quad (4.6)$$

For the overall RMSEs, the mean over all volunteers was taken. The ROI was manually segmented over the aortic arch for every heart phase t .

4.4 Results

Figure 4.4a reveals the mean velocity reconstruction accuracy of frame-by-frame SPIRiT, k - t GRAPPA and k - t SPIRiT for two- and three-point velocity encoding within the ROI covering the aortic arch. The mean overall RMSE over all volunteers is plotted against different undersampling factors. The three velocity encoded directions in measurement (M), phase-encode (P), and slice-select (S) are given. It is seen that k - t SPIRiT improves velocity reconstruction accuracy, especially for higher acceleration factors. k - t GRAPPA was found to slightly outperform frame-by-frame SPIRiT up to $R = 12$. The error level was lowest for the phase-encode (P) direction where highest velocities occur. The through-plane component (S) with the lowest velocity-to-noise ratio (VNR) shows the highest error levels. Figure 4.4b shows linear regression analysis between reference and reconstructed data of the velocity components in P direction for SPIRiT, k - t GRAPPA and k - t SPIRiT. Data for undersampling factors of 4, 8, 12, and 14 are compared. All pixels in the dynamic ROI were included in the analysis. Pearson's correlation coefficients for the two- and three-point reconstructions are shown in Table 4.1. Additional line fit parameters are presented in Tables 4.2 and 4.3 in the Appendix Section 4.6.

R	2-Point			3-point		
	SPIRiT	k - t GRAPPA	k - t SPIRiT	SPIRiT	k - t GRAPPA	k - t SPIRiT
2	0.9968	0.9973	0.9981	0.9989	0.9990	0.9993
4	0.9946	0.9951	0.9960	0.9977	0.9978	0.9983
6	0.9884	0.9905	0.9942	0.9958	0.9962	0.9975
8	0.9857	0.9860	0.9927	0.9938	0.9939	0.9967
10	0.9798	0.9820	0.9911	0.9904	0.9914	0.9957
12	0.9763	0.9792	0.9898	0.9874	0.9890	0.9949
14	0.9734	0.9746	0.9887	0.9863	0.9839	0.9940

Table 4.1 Pearson's correlation coefficients of linear regression analysis between reconstructed and reference velocities.

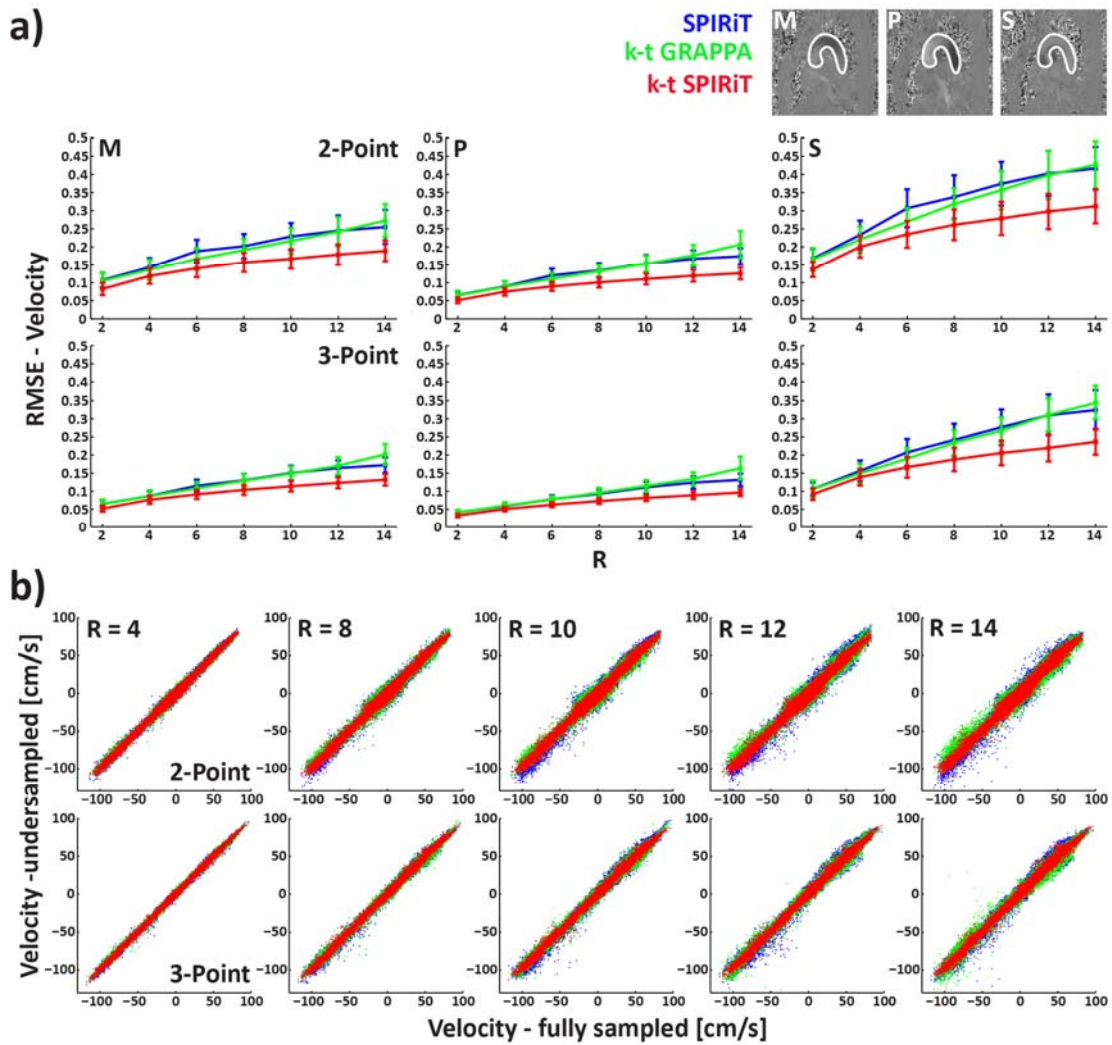


Figure 4.4 a) Mean overall RMSE of the three orthogonal velocity components (M-P-S) as a function of acceleration factor. The error bars indicate the SD. The RMSEs were calculated over ROIs covering the aortic arch as illustrated in the mean velocity maps. **b)** Pixelwise correlation of mean velocities relative to the fully sampled reference in a ROI for the in-plane component P using one (top row) and two (bottom row) velocity encodes. Correlation plots of SPIRiT (blue), k-t GRAPPA (green) and k-t SPIRiT are compared for 4-, 8-, 10-, 12-, and 14-fold undersampling.

In Figure 4.5a, systolic spatial velocity profiles (blue, green and red) along the indicated horizontal lines through the ascending and descending aorta are compared relative to the fully sampled reference (black). Figure 4.5b shows a SPIRiT, k-t GRAPPA and k-t SPIRiT reconstructed systolic velocity map for different undersampling factors together with the reference. The corresponding masked error maps confirm better performance of k-t SPIRiT compared with SPIRiT and k-t GRAPPA.

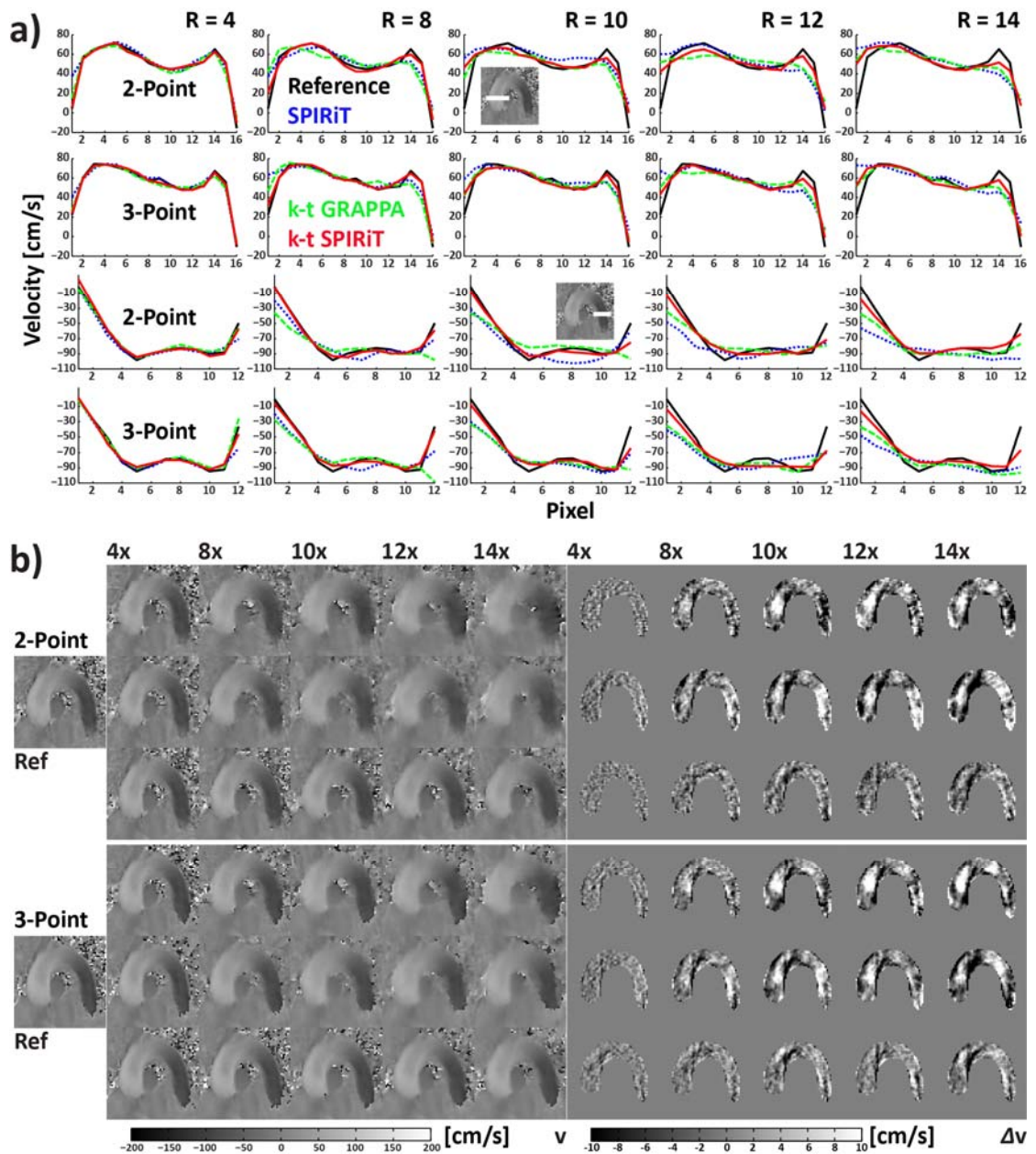


Figure 4.5 a) Horizontal velocity profile plots along the indicated lines through the ascending (top two rows) and descending (bottom two rows) aorta. Two- and three-point reconstructed P components are shown for the fully sampled reference (black) and the three reconstruction techniques (blue, green and red). b) Reconstructed systolic velocity maps (SPIRiT: top row, k -t GRAPPA: middle row, k -t SPIRiT: bottom row) along with reference data and masked error maps are given.

Magnitude reconstruction accuracy of frame-by-frame SPIRiT, k -t GRAPPA and k -t SPIRiT over all volunteers is compared in Figure 4.6a. The overall RMSE with respect to the ROI illustrated in the systolic magnitude reference image is plotted against different undersampling factors for all three orthogonal directions. The rows correspond to the reference and the applied encoding velocities.

A systolic magnitude image is added to each plot illustrating the magnitude damping observed at higher k_v -values. Error levels increase with decreasing encoding velocities. Additionally, at higher k_v 's, less improvement in reconstruction accuracy by k - t SPIRiT is observed for the M- and P-directions. Figure 4.6b compares the temporally resolved error performance in a single volunteer of SPIRiT, k - t GRAPPA and k - t SPIRiT. The temporal magnitude RMSE is shown for different undersampling factors (columns) and encoding velocities (rows) for the S-direction. k - t SPIRiT clearly outperforms frame-by-frame SPIRiT and k - t GRAPPA reconstruction for high undersampling factors. Temporal changes in magnitude level due to higher gradient's first moments are reflected by increased RMSEs during systole.

Systolic magnitude frames from fully sampled signal are shown together with frame-by-frame SPIRiT (top), k - t GRAPPA (middle) and k - t SPIRiT (bottom) reconstructed data in Figure 4.7a for two k_v -points along the M-direction. Corresponding difference maps relative to reference confirm reduced reconstruction error of k - t SPIRiT relative to SPIRiT and k - t GRAPPA. Data acquired at $k_v / \Delta k_v = 0$ show larger error reduction by k - t SPIRiT compared with data encoded with $k_v / \Delta k_v = 4$. Temporal magnitude profiles for all acceleration factors are given in Figure 4.7b.

The mean overall RMSEs of SD for each velocity encoded direction are shown in Figure 4.8a together with plots of the temporal SD RMSE in a single volunteer. Errors are smallest in systolic frames where phase dispersion is largest. In Figure 4.8b,c , systolic velocity magnitude and TKE maps derived from the SD reconstructions using frame-by-frame SPIRiT and k - t GRAPPA versus k - t SPIRiT are shown relative to the fully sampled reference.

Velocity reconstructions of prospectively undersampled data reconstructed with SPIRiT and k - t SPIRiT are compared in Figure 4.9a relative to the fully sampled reference. A systolic P-component velocity map is shown for different undersampling factors and for two- and three-point processing. Corresponding error maps (Figure 4.9b) confirm increased reconstruction accuracy for k - t SPIRiT.

Systolic magnitude frames reconstructed from prospectively undersampled data are shown in Figure 4.10a along with the fully sampled reference. SPIRiT and k - t SPIRiT reconstruction results are shown for two velocity encodes along the P-direction. Figure 4.10b represents the corresponding temporal profile plots along the indicated lines. Improved reconstruction by k - t SPIRiT is revealed. Figure 4.10c shows systolic TKE maps reconstructed using frame-by-frame SPIRiT and k - t SPIRiT.

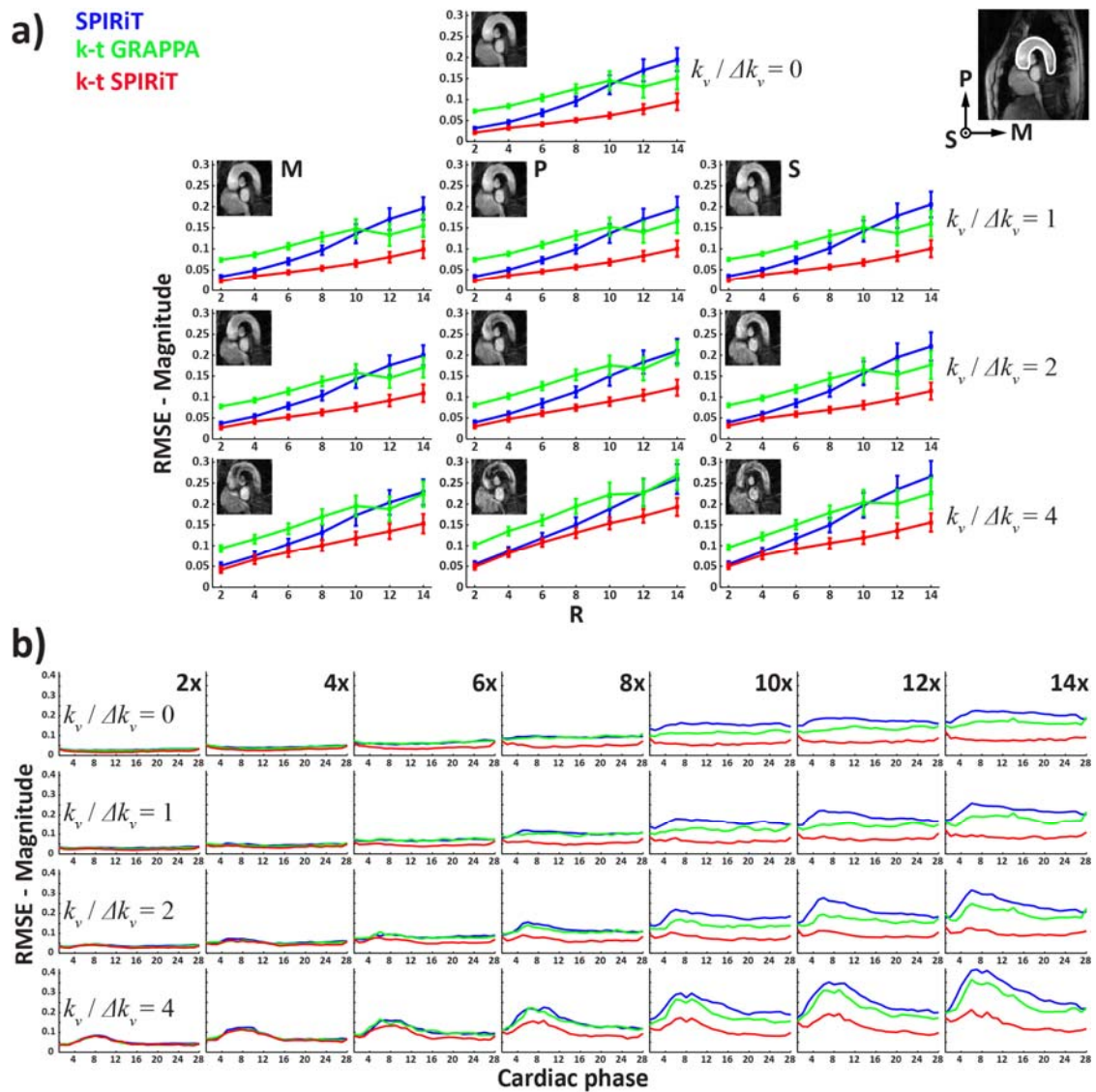


Figure 4.6 a) Mean and SD of overall RMSE of SPIRiT, k-t GRAPPA and k-t SPIRiT magnitude reconstruction for reference image ($k_v / \Delta k_v = 0$), 200 cm/s- ($k_v / \Delta k_v = 1$), 100 cm/s- ($k_v / \Delta k_v = 2$) and 50 cm/s-encoded ($k_v / \Delta k_v = 4$) images. The RMSEs are assessed from ROIs as indicated in the systolic magnitude reference frame. The frames in the graphs illustrate the signal destruction in the blood pool due to velocity induced intravoxel phase dispersion at higher k_v -values. **b)** Temporal magnitude reconstruction accuracy of the three techniques applied. Error curves for the S-direction are compared as a function of undersampling factor (columns) and encoding velocity (rows).

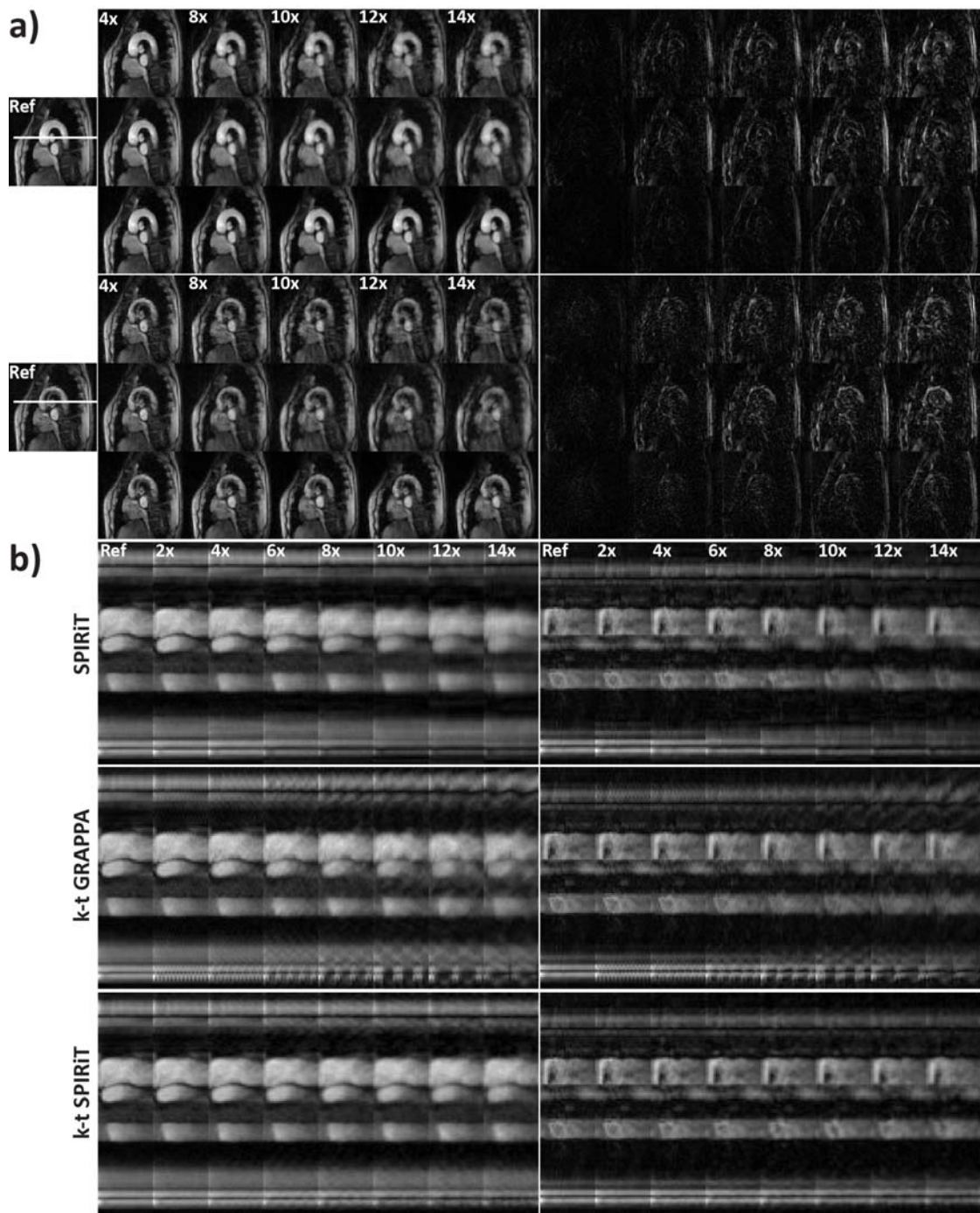


Figure 4.7 a) Systolic magnitude images of $k_v / \Delta k_v = 0$ (top) and $k_v / \Delta k_v = 4$ (bottom) encoded segment in M direction. Fully sampled reference and reconstructed frames (SPIRiT: top row, k-t GRAPPA: middle row, k-t SPIRiT: bottom row) from 4-, 8-, 10-, 12-, and 14-fold undersampling are illustrated together with corresponding error maps. b) Temporal profile plots along indicated lines in reference images.

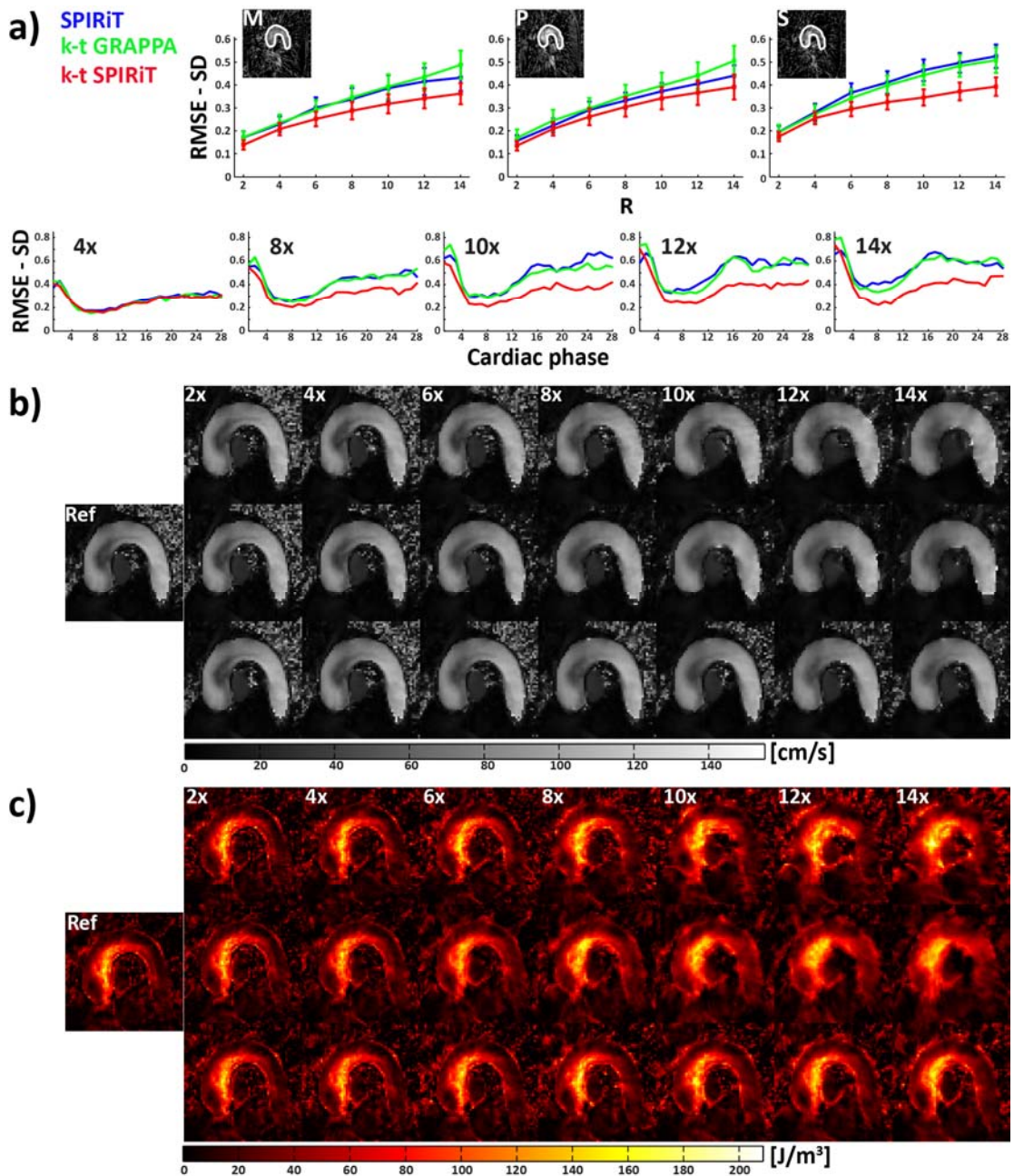


Figure 4.8 a) Mean overall reconstruction accuracy of SDs fitted to the magnitude images for all three encoded directions depending on the degree of undersampling. The ROI is illustrated in the three systolic SD maps. Additionally, RMSEs of SD reconstructions along S-direction as a function of cardiac phase for 4-, 8-, 10-, 12-, and 14-fold undersampling are shown. b) Systolic velocity magnitude maps obtained with frame-by-frame SPIRiT (top row), k-t GRAPPA (middle row) and k-t SPIRiT (bottom row) compared with the fully sampled reference. c) Corresponding TKE maps [J/m³].

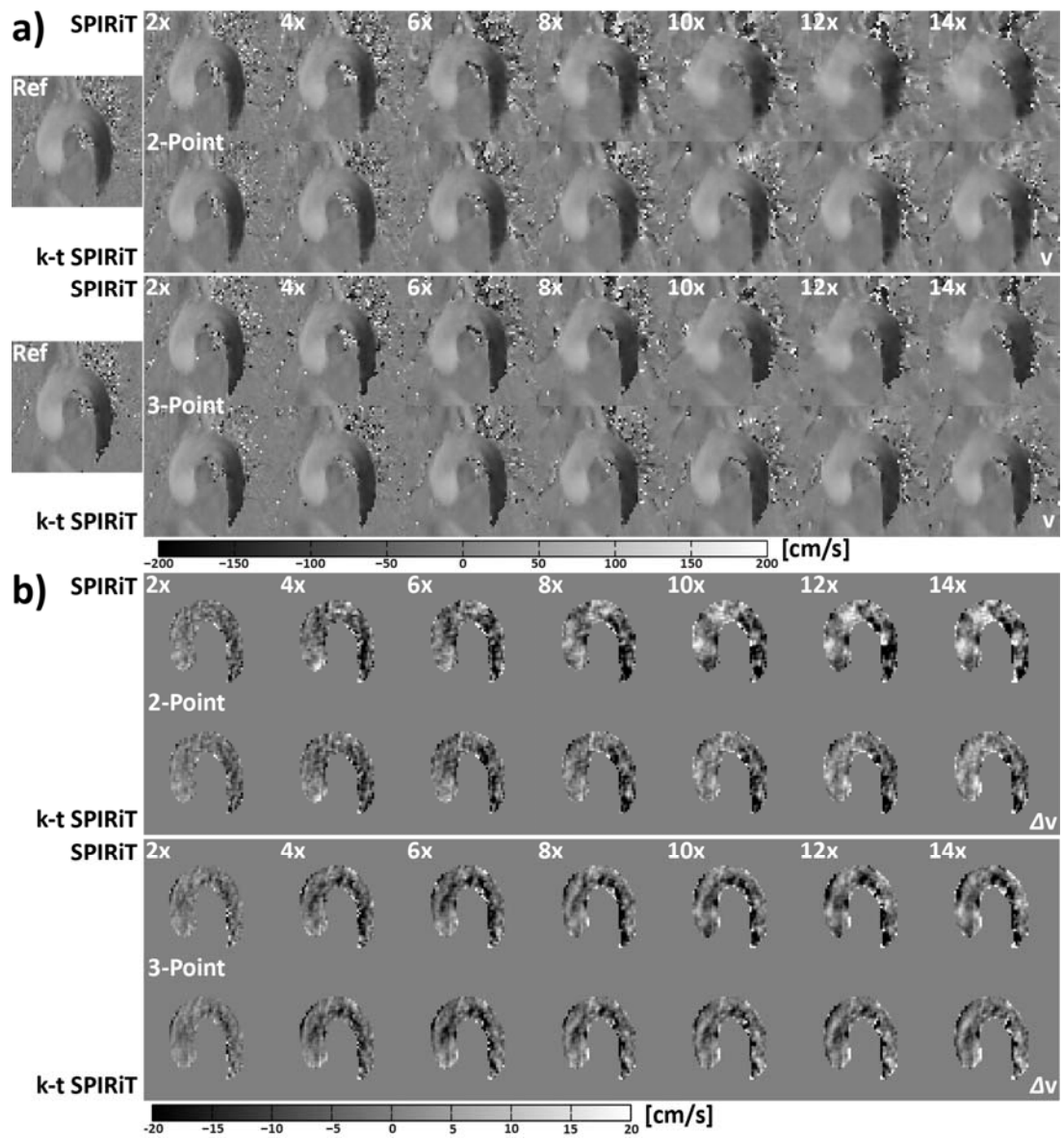


Figure 4.9 a) *SPIRiT* and *k-t SPIRiT* reconstructed systolic mean velocity maps encoded along *P* direction of prospectively undersampled data. Results from two- (top row) and three-point (bottom row) processing are illustrated together with data from the fully sampled reference. b) Corresponding error maps.

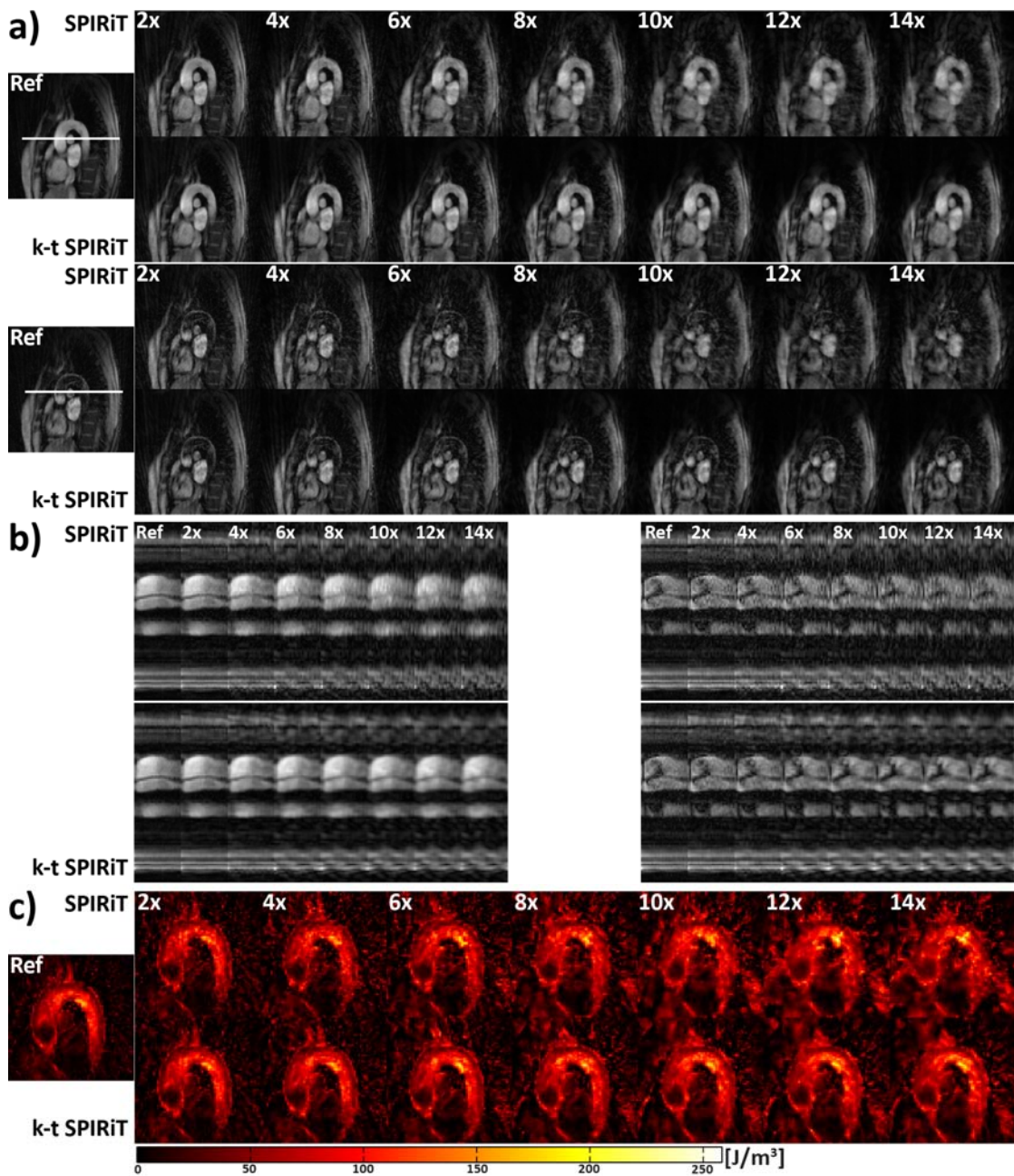


Figure 4.10 a) Systolic magnitude images reconstructed from prospectively undersampled data reconstructed with SPIRiT and k-t SPIRiT. Images illustrate two velocity encodes (top: $k_v / \Delta k_v = 0$, bottom: $k_v / \Delta k_v = 4$) along P direction and the fully sampled reference. b) Corresponding temporal profile plots along indicated lines. c) Systolic TKE maps.

4.5 Discussion

In this work, the auto-calibrating coil-by-coil method SPIRiT has been extended to exploit both spatial and temporal correlations. The proposed k - t SPIRiT scheme has successfully been implemented and tested on simulated and prospectively undersampled 2D radial multi- k_v flow encoded in vivo data of the aortic arch.

k - t SPIRiT shows improved reconstruction accuracy of mean velocity. Error levels were lowest along the component with highest velocities. Point-wise correlation analysis confirmed improved accuracy of mean velocities reconstructed with k - t SPIRiT versus SPIRiT and radial k - t GRAPPA relative to fully sampled ground truth data up to radial undersampling factors of 14.

Improvements in magnitude reconstruction accuracy were shown for all k_v -encodings. Highest error reduction by k - t SPIRiT was found at high encoding velocities with low intravoxel phase dispersion. Accordingly, magnitude damping was low, and hence, local signal-to-noise ratio was high. Temporally resolved magnitude profiles revealed a clear reduction in spatial blurring and enhanced sharpness of vessel borders with k - t SPIRiT compared to frame-by-frame SPIRiT and k - t GRAPPA reconstruction. At higher k_v -encodes, temporal profile plots of the proposed k - t method showed reduced noise-like artifacts relative to standard SPIRiT. Relative to k - t GRAPPA, which resulted in temporal blurring at high acceleration factors, spatio-temporal resolution was better preserved when using k - t SPIRiT. Consequently, the accuracy of assessing velocity SD and TKE was found to improve with k - t SPIRiT relative to SPIRiT and k - t GRAPPA.

In the present implementation, each spatial direction was encoded using the same k_v -sampling pattern and strengths. The error dependency of velocity SD as a function of cardiac phase, and hence of VNR, prompts for Bayesian processing of multi- k_v data as proposed previously [160]. At the same time, the high radial undersampling factors feasible with k - t SPIRiT would permit finer sampling of k_v -space to improve SD estimates also at lower mean velocities during diastole. In this respect, it should, however, be noted that SD and TKE estimates are diagnostically most relevant during systole in the aorta where transient and even turbulent flows can occur.

In the k - t SPIRiT reconstruction scheme implemented here, spatial, temporal or spatio-temporal transform operators were not included. It is expected that the incorporation of sparsifying transforms can further improve reconstruction accuracy.

Currently, average reconstruction times per frame for k - t and frame-by-frame SPIRiT are in the same range using the Matlab implementation (38 s with calibration operator calculation, 18 s without calibration for velocity encoded frames). However, it has already been demonstrated

that SPIRiT reconstruction times can significantly be reduced by using parallelized implementation on multi-GPU and multi-core systems [165].

Applying k - t SPIRiT to generalized PC MRI has allowed assessing reconstruction accuracy of both image magnitude and phase. Adaptation of the method to other dynamic imaging protocols including cine imaging is straightforward.

In summary, k - t SPIRiT offers improved reconstruction accuracy at high radial undersampling factors and hence will facilitate the use of generalized PC MRI for routine use. While this preliminary report has described the implementation and feasibility, studies in larger cohorts are warranted to prove robustness of the approach in a clinical setting.

4.6 Appendix

R	2-Point			3-point		
	SPiRiT	<i>k-t</i> GRAPPA	<i>k-t</i> SPiRiT	SPiRiT	<i>k-t</i> GRAPPA	<i>k-t</i> SPiRiT
2	0.9978	0.9946	0.9974	0.9987	0.9959	0.9984
4	0.9905	0.9810	0.9923	0.9938	0.9854	0.9943
6	0.9847	0.9683	0.9866	0.9897	0.9760	0.9892
8	0.9800	0.9546	0.9779	0.9876	0.9700	0.9835
10	0.9908	0.9356	0.9715	0.9963	0.9619	0.9766
12	0.9792	0.9123	0.9666	0.9862	0.9548	0.9730
14	0.9820	0.8848	0.9642	0.9888	0.9304	0.9732

Table 4.2 *m-values (slope) of linear line fits ($mx + b$) in Figure 4.4b*

R	2-Point			3-point		
	SPiRiT	<i>k-t</i> GRAPPA	<i>k-t</i> SPiRiT	SPiRiT	<i>k-t</i> GRAPPA	<i>k-t</i> SPiRiT
2	-0.0044	-0.0189	0.0027	0.0129	0.0086	0.0253
4	0.0119	-0.0415	0.0314	0.0440	0.0646	0.0967
6	-0.0182	-0.0202	0.0591	0.0695	0.1249	0.1739
8	-0.1558	0.1772	0.0879	0.1243	0.2294	0.2625
10	-0.4621	0.2005	0.1409	0.0426	0.3124	0.3356
12	0.1149	0.4894	0.0990	0.3172	0.5160	0.3252
14	-0.0682	0.1679	0.0793	0.4869	0.1102	0.3433

Table 4.3 *b-values (offset) of linear line fits ($mx + b$) in Figure 4.4b*

Chapter 5

Accelerating 4D Flow MRI by Exploiting Vector Field Divergence Regularization*

5.1 Introduction

Time-resolved, 3D phase-contrast (PC) flow measurements, also referred to as 4D flow MRI, allow the assessment of complex flow patterns and calculation of hemodynamic parameters in larger vessels [4, 166]. The method encodes the velocity vector components of blood flow along three orthogonal directions into phase differences between multiple complex-valued images acquired with different first gradient moments [167]. As a result of the sequential encoding concept and large volumetric coverage, scan times can be considerable, thereby hampering wide-spread use of the method in a clinical setting [168].

Scan acceleration techniques exploiting coil sensitivity weighting [23, 56, 63], spatio-temporal redundancy [84-86, 142, 143, 169], transform-domain sparsity [73, 78] or non-Cartesian sampling [170, 171] have successfully been applied to PC protocols [10, 11, 148-151, 154, 155, 172].

In compressed sensing (CS) based techniques [73], a smooth object phase is assumed and transforms are designed to sparsify the image magnitude. Additional ℓ_1 -regularization of complex differences between flow encoded segments has shown improvement for 2D cine PC MRI with one-directional velocity encoding [156]. Alternatively, the volume continuity of incompressible flow, i.e. the divergence-free condition, has been exploited for noise reduction of velocity vector

* Published in: C. Santelli, M. Loecher, J. Busch, O. Wieben, T. Schaeffter and S. Kozerke, "Accelerating 4D Flow MRI by Exploiting Vector Field Divergence Regularization", Magnetic Resonance in Medicine, DOI 10.1002/mrm.25563, 2015.

fields in post-processing methods [173-180]. Normalized convolution with divergence-free radial basis functions (RBF) [177] and divergence-free Wavelets (DFWs) thresholding [180] have demonstrated promising vector field denoising performance. While the RBF method needs accurate segmentation of the blood pool and long processing times, Wavelet-based vector field denoising imposes fast and suitable boundary conditions that can be obtained by keeping non-divergence-free Wavelet coefficients.

A reconstruction framework for CS with separate magnitude and phase regularization has been proposed in [181] with alternating minimization of image magnitude and phase. The method was tested on retrospectively undersampled 2D flow measurements with ℓ_1 -norm regularization of Wavelet-transformed magnitude and a finite difference (FD) penalty using either ℓ_2 -norm or edge-preserving potential functions. Relative to standard CS, improved reconstruction performance of magnitude and phase data could be demonstrated.

Based on the concept to directly incorporate physical priors about blood flow, which was first presented in [182], we propose to use the separate magnitude and phase framework for 3D velocity field reconstruction with ℓ_1 -regularization of image phase components enforcing incompressibility and divergence-free condition, respectively. A novel reconstruction algorithm using a FD divergence and curl operator is proposed. Similar to [183], DFW-based velocity field regularization is presented, however, with a simpler thresholding scheme as proposed in [183]. The performance of these phase regularization methods is tested and compared to standard CS on simulated 3D computational fluid dynamics (CFD) and 4D flow MRI in vivo data from healthy volunteers and a patient.

5.2 Theory

5.2.1 Separate Magnitude and Phase Reconstruction

Let $\boldsymbol{\rho} = \mathbf{m} \circ e^{i\boldsymbol{\phi}} \in \mathbb{C}^N$ be the N -dimensional complex-valued image vector with real valued magnitude $\mathbf{m} \in \mathbb{R}^N$ and phase $\boldsymbol{\phi} \in \mathbb{R}^N$, \mathbf{E} the encoding matrix mapping the reconstructed object to the acquired data $\mathbf{d} \in \mathbb{C}^M$, $\boldsymbol{\Psi}$ a sparsifying transform (e.g. an orthonormal Wavelet transform) and λ a regularization parameter trading data consistency and transform-domain sparsity. \circ denotes the component-wise vector multiplication between \mathbf{m} and the phase exponential vector

$e^{i\phi}$. For multi-coil Cartesian data acquisition, the encoding operator is composed of coil sensitivity weighting $\mathbf{S} \in \mathbb{C}^{N_c \times N \times N}$, FT $\mathbf{F} \in \mathbb{C}^{N \times N}$ and an undersampling matrix $\mathbf{I}_u \in \{0,1\}^{M \times N}$: $\mathbf{E} = (\mathbf{I}_{N_c} \otimes \mathbf{I}_u \mathbf{F}) \mathbf{S}$. While standard ℓ_1 -norm regularized CS [73] minimizes the convex error functional

$$\|\mathbf{d} - \mathbf{E}\boldsymbol{\rho}\|_2^2 + \lambda \|\boldsymbol{\Psi}\boldsymbol{\rho}\|_1, \quad (5.1)$$

a separate magnitude and phase CS-based reconstruction formalism [181] aims to solve the optimization problem

$$\arg \min_{\mathbf{m}, \phi} \|\mathbf{d} - \mathbf{E}(\mathbf{m} \circ e^{i\phi})\|_2^2 + \lambda_m \|\boldsymbol{\Psi}_m \mathbf{m}\|_1 + \lambda_\phi R(\phi), \quad (5.2)$$

via alternating minimization of the error function $f(\mathbf{m}, \phi) = \|\mathbf{d} - \mathbf{E}(\mathbf{m} \circ e^{i\phi})\|_2^2 + \lambda_m \|\boldsymbol{\Psi}_m \mathbf{m}\|_1 + \lambda_\phi R(\phi)$.

Thereby, $f(\mathbf{m}, \phi)$ is minimized with respect to phase and magnitude with fixed magnitude \mathbf{m}^k and phase ϕ^{k+1} obtained in iteration step k and $k+1$, respectively:

$$\phi^{k+1} = \arg \min_{\phi} f(\mathbf{m}^k, \phi) \quad (5.3)$$

$$\mathbf{m}^{k+1} = \arg \min_{\mathbf{m}} f(\mathbf{m}, \phi^{k+1}). \quad (5.4)$$

Here, the sparsifying operator $\boldsymbol{\Psi}_m$ acts only on the magnitude while different regularization $R(\phi)$ is used for the phase.

5.2.2 Phase Regularizers

For 4-point velocity encoding [42], the phase of the image acquired with flow compensation (denoted as reference image ϕ_0) is ℓ_2 -norm penalized via a gradient operator on the exponential of the phase, thereby enforcing smoothness [181]:

$$R(\phi_0) = \left\| \begin{bmatrix} \mathbf{D}_x^T & \mathbf{D}_y^T & \mathbf{D}_z^T \end{bmatrix}^T e^{i\phi_0} \right\|_2^2, \quad (5.5)$$

with the FD gradient operators $\mathbf{D}_{x,y,z}$ along the three orthogonal directions.

In contrast, ℓ_1 -penalization of the underlying 3D velocity vector field is proposed for the three velocity encodes. Following the vector field denoising principles in [176] and [180], FD- or Wavelet-based velocity regularization is incorporated as two different approaches for regularizing divergence. The three corresponding magnitude and phase difference images are now stacked in

vectors $\mathbf{m} \in \mathbb{R}^{3N}$ and $\phi_v \in \mathbb{R}^{3N}$, respectively. FD divergence and curl penalization is performed with a divergence matrix $\mathbf{D}_{div} = [\mathbf{D}_x \ \mathbf{D}_y \ \mathbf{D}_z]$ and a curl operator $\mathbf{D}_{curl} = [\mathbf{0} \ \mathbf{D}_z \ -\mathbf{D}_y; \ -\mathbf{D}_z \ \mathbf{0} \ \mathbf{D}_x; \ \mathbf{D}_y \ -\mathbf{D}_x \ \mathbf{0}]$:

$$R(\phi_v) = \|\Psi_{div,curl} \mathbf{K}_v \phi_v\|_1 \quad \text{with} \quad \Psi_{div,curl} = \begin{bmatrix} \mathbf{D}_{div} \\ \gamma \mathbf{D}_{curl} \end{bmatrix}. \quad (5.6)$$

The diagonal matrix \mathbf{K}_v maps phase to velocity values according to the applied gradient's first moments. Relative weighting between divergence and curl penalization can directly be included by scaling of the resulting divergence scalar and curl vector field coefficients via $\gamma \in \mathbb{R}^{\geq 0}$. DFW transform (DFWT) [179, 180] projects a 3D vector field on divergence-free and non-divergence-free complement vector Wavelets spanning the entire space of velocity fields in \mathbb{R}^3 . Resulting divergence-free coefficients provide a sparse representation of incompressible flow, while non-divergence-free coefficients can depict divergence in e.g. partial volume voxels at vessel boundaries. Accordingly, ℓ_1 -phase-regularization using DFWT reads:

$$R(\phi_v) = \|\Psi_{df} \mathbf{K}_v \phi_v\|_1 \quad \text{with} \quad \Psi_{df} = \mathbf{B} \begin{bmatrix} \Psi_x & \dots & \mathbf{0} \\ \vdots & \Psi_y & \vdots \\ \mathbf{0} & \dots & \Psi_z \end{bmatrix}, \quad (5.7)$$

where $\Psi_{x,y,z}$ perform 3D Wavelet decompositions with component and coordinate dependent scaling and Wavelet functions [179]. \mathbf{B} implements linear combinations of the resulting standard Wavelet decomposition coefficients to obtain divergence-free and non-divergence-free representations. Detailed forward and inverse linear combinations are listed in [179, 180].

5.2.3 Phase Difference Reconstruction Algorithms

Let $\mathbf{E}_{m,\phi_0}^k = (\mathbf{I}_3 \otimes \mathbf{E}) \text{diag}(\mathbf{m}^k \circ e^{i\phi_0})$ be the modified encoding matrix including object magnitudes obtained in iteration step k , duplicated background phase $\phi_0 \in \mathbb{R}^{3N}$ and $\Psi_\phi \in \{\Psi_{div,curl}, \Psi_{df}\}$. The following non-convex optimization problem is then solved to update the velocity induced phase vector:

$$\phi_v^{k+1} = \arg \min_{\phi_v} \|\mathbf{d} - \mathbf{E}_{m,\phi_0}^k e^{i\phi_v}\|_2^2 + \lambda_\phi \|\Psi_\phi \mathbf{K}_v \phi_v\|_1. \quad (5.8)$$

For FD-based regularization, we propose to use an augmented Lagrangian (AL) framework with variable splitting [184]. More precisely, equation (5.8) is converted into an equivalent constrained optimization problem by introducing auxiliary variables decoupling quadratic and non-quadratic

terms. Then, an AL algorithm using alternating minimization with respect to the auxiliary variable is applied, dividing reconstruction into smaller sub-problems which can efficiently be implemented compared to direct solving of equation (5.8).

Using the splitting $\mathbf{u}_1 = e^{i\phi}$ and $\mathbf{u}_2 = \Psi_{div, curl} \mathbf{K}_v \phi_v$, equation (5.8) is first transformed into the constrained problem

$$\arg \min_{\mathbf{u}_1, \mathbf{u}_2, \phi} \left\| \mathbf{d} - \mathbf{E}_{m, \phi}^k \mathbf{u}_1 \right\|_2^2 + \lambda_\phi \left\| \mathbf{u}_2 \right\|_1 \quad \text{s.t.} \quad \mathbf{u}_1 = e^{i\phi}, \quad \mathbf{u}_2 = \Psi_{div, curl} \mathbf{K}_v \phi_v, \quad (5.9)$$

resulting in the unconstrained optimization problem with the vectors of modified Lagrange multipliers \mathbf{b}_1 and \mathbf{b}_2 , and the tuning parameters μ_1 and μ_2 weighting the quadratic penalty terms:

$$\arg \min_{\mathbf{u}_1, \mathbf{u}_2, \phi} \left\| \mathbf{d} - \mathbf{E}_{m, \phi}^k \mathbf{u}_1 \right\|_2^2 + \lambda_\phi \left\| \mathbf{u}_2 \right\|_1 + \frac{\mu_1}{2} \left\| \mathbf{u}_1 - e^{i\phi} - \mathbf{b}_1 \right\|_2^2 + \frac{\mu_2}{2} \left\| \mathbf{u}_2 - \Psi_{div, curl} \mathbf{K}_v \phi_v - \mathbf{b}_2 \right\|_2^2. \quad (5.10)$$

A solution of equation (5.10) is then obtained by alternating minimization with respect to \mathbf{u}_1 , \mathbf{u}_2 and ϕ_v including update rules for \mathbf{b}_1 and \mathbf{b}_2 ($\mathbf{b}_1^0 = \mathbf{b}_2^0 = \mathbf{0}$):

$$\mathbf{u}_1^{n+1} = \arg \min_{\mathbf{u}_1} \left\| \mathbf{d} - \mathbf{E}_{m, \phi}^k \mathbf{u}_1 \right\|_2^2 + \frac{\mu_1}{2} \left\| \mathbf{u}_1 - e^{i\phi^n} - \mathbf{b}_1^n \right\|_2^2 \quad (5.11)$$

$$\mathbf{u}_2^{n+1} = \arg \min_{\mathbf{u}_2} \lambda_\phi \left\| \mathbf{u}_2 \right\|_1 + \frac{\mu_2}{2} \left\| \mathbf{u}_2 - \Psi_{div, curl} \mathbf{K}_v \phi_v^n - \mathbf{b}_2^n \right\|_2^2 \quad (5.12)$$

$$\phi_v^{n+1} = \arg \min_{\phi} \frac{\mu_1}{2} \left\| \mathbf{u}_1^{n+1} - e^{i\phi} - \mathbf{b}_1^n \right\|_2^2 + \frac{\mu_2}{2} \left\| \mathbf{u}_2^{n+1} - \Psi_{div, curl} \mathbf{K}_v \phi_v - \mathbf{b}_2^n \right\|_2^2 \quad (5.13)$$

$$\begin{aligned} \mathbf{b}_1^{n+1} &= \mathbf{b}_1^n + e^{i\phi^{n+1}} - \mathbf{u}_1^{n+1} \\ \mathbf{b}_2^{n+1} &= \mathbf{b}_2^n + \Psi_{div, curl} \mathbf{K}_v \phi_v^{n+1} - \mathbf{u}_2^{n+1}, \end{aligned} \quad (5.14)$$

where n denotes the sub-iteration step within the $(k+1)$ -th update of ϕ , given in equation (5.10). The cost function (5.11) is quadratic in \mathbf{u}_1 which can be updated with a few numbers of conjugate gradient (CG) iterations [59]. Equation (5.12) is solved using soft-thresholding [76]. The non-convex sum in equation (5.13) is minimized using non-linear CG with Fletcher-Reeves update and a Newton-Raphson line search using backtracking [181]. Corresponding gradient and Hessian operators are detailed in the Appendix Section 5.6.1.

To exploit sparsity of the divergence-free flow field while allowing for divergent components at vessel borders, soft-thresholding of the divergence-free and non-divergence-free Wavelet coefficients is used in an iterative reconstruction scheme alternating between Wavelet shrinkage and data consistency (Figure 5.1).

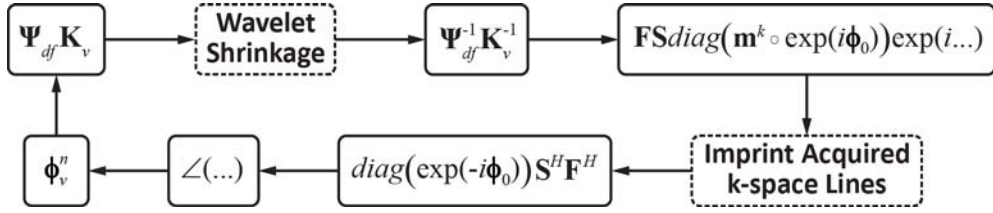


Figure 5.1 Schematic of iterative phase update via DFW regularization. The intermediate phase maps ϕ_v^n are decomposed using the divergence-free Wavelet filter bank whose coefficients are thresholded and then transformed back. Upon background phase addition and magnitude multiplication, the resulting complex-valued image is weighted by the coil sensitivities and transformed into k-space where sampled data points are replaced with the acquired signals. After inverse FT, coil combination and background phase subtraction, the phase provides an updated solution vector.

5.3 Methods

5.3.1 Numerical Phantom

Static three-dimensional 4-point PC MR data were simulated based on CFD data in a U-bend shaped tube where the fluid is modeled to be approximately divergence-free. The encoding velocity was set at 110% peak velocity in the CFD data set. A seven-element coil array whose elements were uniformly distributed around the object was incorporated. Complex Gaussian noise was added in image space to obtain a signal-to-noise ratio (SNR) of 15 relative to the maximum magnitude of the coil-combined images. Retrospectively decimated data sets with undersampling factors of $R = 3, 6$ and variable-density random undersampling [73] along k_y - and k_z -direction were reconstructed. Missing k-space data were then reconstructed using standard ℓ_1 -regularized CS-SENSE as well as the proposed separate magnitude/phase CS framework using either DFW- or FD-based operators.

5.3.2 In Vivo Experiments

Free-breathing navigator-gated 3D gradient-echo Cartesian cine 4-point PC data of the aortic arch were acquired in 5 healthy volunteers on a 3 Tesla Philips Achieva scanner (Philips Healthcare, Best, The Netherlands) using a six-element cardiac receive array. Data from 24 heart phases (42

ms temporal resolution), imaging volumes of $322 \times 252 \times 50.75\text{-}57.75 \text{ mm}^3$ (receiver bandwidth: 335 Hz/voxel) were acquired with an isotropic voxel size of $1.75 \times 1.75 \times 1.75 \text{ mm}^3$, a flip angle of 10° and TR/TE = 4.7/2.4 ms. The encoding velocities along the three orthogonal directions FH-AP-RL varied between 140-200, 120-160 and 100-130 cm/s, which were prescribed to optimize the dynamic ranges of the phase measurements based on acquired velocities from scout 2D PC scans. Additionally, post-operative data from a 71-year-old patient with an aortic valve and aortic prosthesis were acquired on a 1.5 Tesla Philips Achieva system with a 5-element cardiac coil array, a $320 \times 310 \times 82 \text{ mm}^3$ imaging volume (receiver bandwidth: 191 Hz/voxel), a $2 \times 2 \times 2 \text{ mm}^3$ voxel size, a 10° flip angle and TR/TE = 4.8/2.2 ms. Three different first gradient moments corresponding to encoding velocities of 160, 120 and 100 cm/s were applied.

Fully sampled data were retrospectively undersampled ($R = 3, 6$) using variable-density random undersampling in the phase encoding plane [73] and then reconstructed using standard CS and CS with DFW and FD phase regularization.

Written informed consent was obtained from all subjects prior to scanning according to ethics approval and institutional guidelines.

5.3.3 Image Reconstruction

Normalized 3D coil sensitivities were estimated from in vivo data using eigendecomposition of a linear k-space reconstruction operator [65].

For standard CS reconstruction of complex-valued images (reference and velocity encodes), an iterative projection onto convex sets (POCS) algorithm [185] leaving the acquired data unchanged was used (Table 5.1a). With normalized coil sensitivities ($\mathbf{S}^H \mathbf{S} \in \{\mathbf{I}_N, \mathbf{I}_{3N}\}$), the algorithm reduces to iterative soft-thresholding with a constant gradient step size of 1 [76]:

$$\boldsymbol{\rho}^{k+1} = \boldsymbol{\Psi}^H \mathcal{S}_{\lambda/2} \left(\boldsymbol{\Psi} \left[\boldsymbol{\rho}^k + \mathbf{E}^H (\mathbf{d} - \mathbf{E} \boldsymbol{\rho}^k) \right] \right), \quad (5.15)$$

with the orthogonal 3D Wavelet transform matrix $\boldsymbol{\Psi}$ and the shrinkage function

$$\mathcal{S}_t(x_i) = \max(1 - t/|x_i|, 0)x_i \quad (5.16)$$

operating on the vector elements x_i . A modified version keeping the image phase fixed, was implemented (Table 5.1b) for the magnitude update steps (5.4). The diagonal matrix \mathbf{W} fixes the phase values according to reference ($\mathbf{W} = \text{diag}(e^{i\phi^k})$) and velocity encoded ($\mathbf{W} = \text{diag}(e^{i\phi^k} \circ e^{i\phi^{k+1}})$) image reconstruction.

a) Complex-Valued Image Reconstruction			b) Magnitude Update		
Init: $k = 0, nIter, \rho^0, t_0, \varepsilon$			Init: $n = 0, nIter, \mathbf{m}^0, t_0, \varepsilon, \mathbf{W}$		
do $\rho^{k+1} \leftarrow \mathbf{S}^H[\mathbf{S}\rho^k + \mathbf{F}^H \mathbf{I}_u^T (\mathbf{d} - \mathbf{E}\rho^k)]$ if $\mathbf{S}^H \mathbf{S} \neq \mathbf{I}$ $\rho^{k+1} \leftarrow (\mathbf{S}^H \mathbf{S})^{-1} \rho^{k+1}$ end $\rho^{k+1} \leftarrow \Psi^H S_{t_k} (\Psi \rho^{k+1})$ $t_{k+1} \leftarrow \text{update}(t_k)$ $e \leftarrow \ \rho^{k+1} - \rho^k\ _2$ $k \leftarrow k + 1$ while $k < nIter$ and $e > \varepsilon$			do $\rho \leftarrow \mathbf{S}^H[\mathbf{S}\mathbf{W}\mathbf{m}^n + \mathbf{F}^H \mathbf{I}_u^T (\mathbf{d} - \mathbf{E}\mathbf{W}\mathbf{m}^n)]$ if $\mathbf{S}^H \mathbf{S} \neq \mathbf{I}$ $\rho \leftarrow (\mathbf{S}^H \mathbf{S})^{-1} \rho$ end $\mathbf{m}^{n+1} \leftarrow \Psi_m^T S_{t_n} (\Psi_m \rho)$ $t_{n+1} \leftarrow \text{update}(t_n)$ $e \leftarrow \ \mathbf{m}^{n+1} - \mathbf{m}^n\ _2$ $n \leftarrow n + 1$ while $n < nIter$ and $e > \varepsilon$		
c)		Reference Image	Velocity Encodes		
Recon Parameter	CS	Magn./Phase	CS	FD	DFW
λ	0.02	-	0.02	-	-
λ_m	-	0.02	-	0.02	0.02
λ_ϕ	-	0.2	-	[1, 5]	-
γ	-	-	-	0.5 / [0.01, 0.03]	-
$\mu_1 = \mu_2$	-	-	-	1	-
$t_{df,1} = t_{df,2}$	-	-	-	-	manually
t_{ndf}	-	-	-	-	[0.9 $t_{df,1/2}$, 1.1 $t_{df,1/2}$]

Table 5.1 a) POCs algorithm for complex-valued image reconstruction. In the intermediate solution, sampled k -space points are replaced with acquired signals. Thereafter, coil normalization is performed followed by the sparse coefficient soft-thresholding step. Thresholds can be updated in every iteration. Iterations are stopped when the maximum number of iterations $nIter$ or the convergence distance ε is reached. **b)** Modified version for magnitude update sub-iteration steps n . The phase from iteration step $k+1$ in (5.3) is assumed to be fixed and incorporated via the diagonal matrix \mathbf{W} . Wavelet shrinkage is then applied on the image magnitude only. **c)** Reconstruction parameters for reference segment and velocity encoded images. If not separated by “/”, values are valid for CFD and in vivo experiments ($t_{df,1/2}$, t_{ndf} : thresholds for divergence-free and non-divergence-free coefficients).

Background phase images ϕ_0 were reconstructed using the regularizer in equation (5.5) and non-linear CGs with backtracking line search [181] (<http://web.eecs.umich.edu/~fessler/irt/irt/contrib/zhao,feng/separate-mag-phase/>). The optimization problem (5.8) was solved for velocity phase updates using the algorithms as described in Section 5.2.3. Three detail levels were used in the DFW decomposition, while the scaling function coefficients remained unchanged during Wavelet shrinkage. Two different global thresholds were used: one for the two divergence-free and one for divergent vector Wavelet coefficients. Non-convex magnitude and phase retrieval was initialized with a few numbers of complex valued convex CS iterations (Table 5.1a) to increase the probability of finding a global minimizer of equation (5.8). Reconstruction times were 6 minutes per timeframe for the DFW method, and 20 minutes per timeframe for the FD method on an AMD 6134 CPU.

Regularization and thresholding parameters were tuned manually for CFD and in vivo experiments in order to reduce divergence without over-regularizing flow values, as determined with divergence and flow measurements. Prior to reconstruction, multi-coil data were normalized to maximum signal magnitude. λ 's were set 0.02 for convex CS, $\lambda_\phi = 0.2$ for background phase reconstruction, $\lambda_\phi \in [1,5]$ for FD, $\gamma = 0.5$ and $\gamma \in [0.02,0.03]$ for CFD and in vivo data, respectively, and $\mu_1 = \mu_2 = 1$. Threshold levels for DFW shrinkage needed to be tuned separately for CFD and in vivo experiments: non-divergence-free thresholds were chosen between 90-110% of divergence-free coefficient threshold levels. Reconstruction parameters are summarized in Table 5.1c.

For the patient data measured at 1.5 Tesla, concomitant field correction was directly included in the phase regularized reconstructions of the velocity encoded images. This was accomplished by appending an additional phase exponential vector with the phase difference corrections to the modified encoding operator in equation (5.8).

The reconstruction algorithms implemented in Matlab (The MathWorks, Natick, MA, USA) and example data sets are available for download from http://www.biomed.ee.ethz.ch/research/bioimaging/cardiac/reduced_data/.

5.3.4 Data Analysis

Velocity vector fields reconstructed from undersampled CFD data were compared relative to the noiseless and fully sampled reference data in terms of directional and velocity magnitude reconstruction accuracy. Mean directional error was quantified in a region of interest (ROI)

capturing the flow regime according to

$$Directional\ error = \frac{1}{|\text{ROI}|} \sum_{i \in \text{ROI}} \left(1 - \frac{|\mathbf{v}_{r,i} \cdot \mathbf{v}_{o,i}|}{\|\mathbf{v}_{r,i}\|_2 \|\mathbf{v}_{o,i}\|_2} \right), \quad (5.17)$$

where $\mathbf{v}_{r,i}$ and $\mathbf{v}_{o,i} \in \mathbb{R}^3$ denote the reconstructed and reference velocity vector at the i -th voxel within the ROI, respectively. The normalized root-mean-square error (nRMSE) was used to quantify the error of velocity magnitude ($v = \|\mathbf{v}\|_2$) reconstruction:

$$nRMSE_v = \sqrt{\frac{\sum_{i \in \text{ROI}} (v_{r,i} - v_{o,i})^2}{\sum_{i \in \text{ROI}} v_{o,i}^2}}. \quad (5.18)$$

Mean values were assessed over 20 trials for $SNR = 15$ and $R = 3, 6$. In vivo data were analyzed by assessing mean absolute divergence, total flow, peak flow, streamline quantification and in-plane velocity vector display.

5.4 Results

Figure 5.2 illustrates velocity magnitude images reconstructed from undersampled data ($R = 3, 6$) relative to the noise-free and noisy fully sampled reference data for the numerical phantom. Improved velocity magnitude maps were obtained with separate magnitude and phase reconstruction using either DFW or FD when compared to standard CS. For $R = 6$, high velocities are best recovered by DFW. Difference maps were calculated relative to the noise-free reference.

Figure 5.3 shows corresponding maps of the absolute value of resulting vector field divergence. Improved noise characteristics and divergence reduction of the reconstructed flow fields are seen when the proposed phase regularization methods are used.

Axial velocity profiles and in-plane velocity vector plots along the indicated line are shown in Figure 5.4 for CS, DFW and FD reconstructions relative to the noise-free and noisy reference data. Improvements of in-plane velocity pattern visualization by phase-regularized reconstruction can be seen. At $R = 6$, standard CS produces vector fields having less visible noise as compared to $R = 3$. This qualitative improvement with increasing undersampling factor can also be observed for the proposed DFW and FD methods.

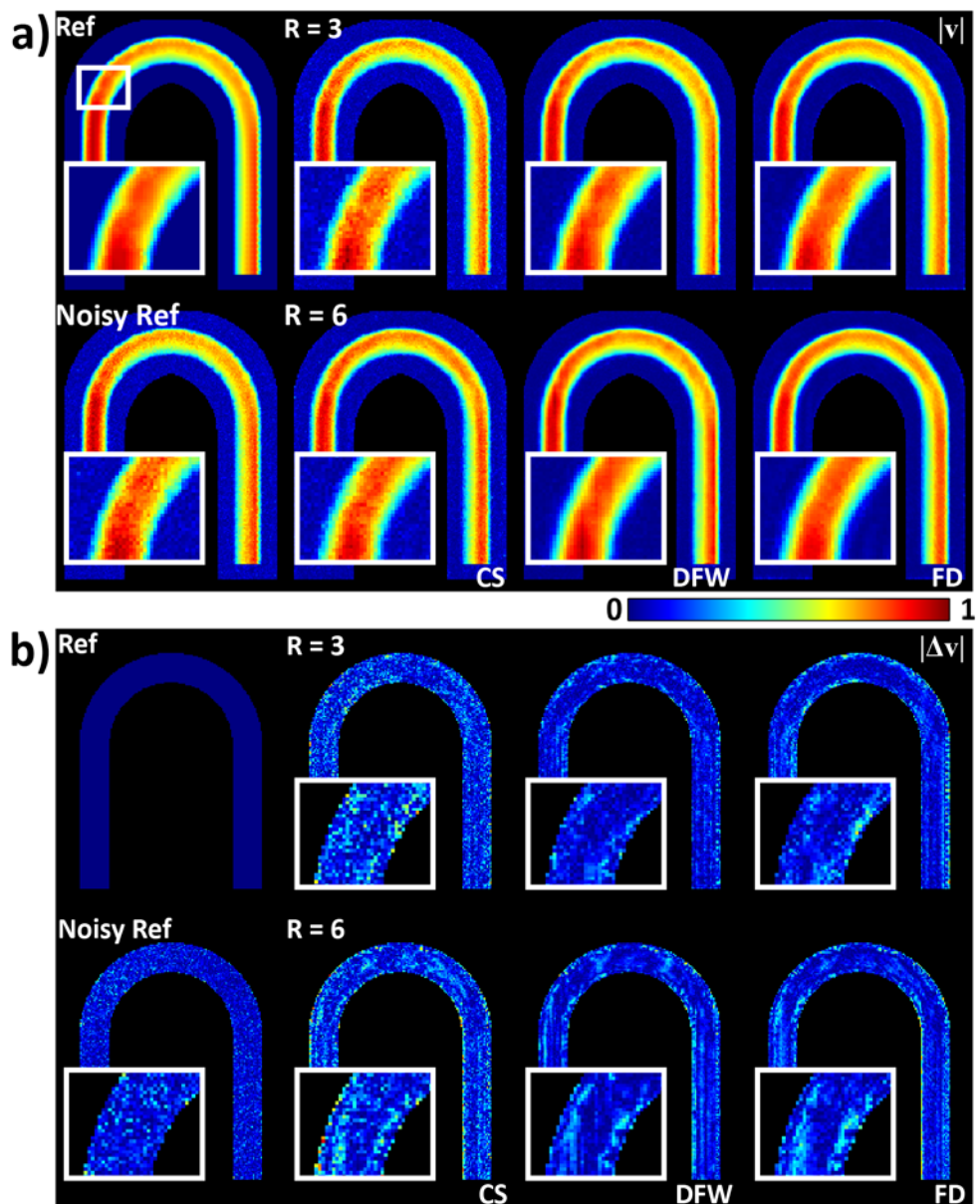


Figure 5.2 Numerical phantom. Normalized velocity magnitude images for CS, DFW and FD reconstructions from 3- (top row) and 6-fold (bottom row) undersampled data relative to noise-free and noisy ($SNR = 15$) references **a)**. Corresponding difference maps are given in **b)**.

Figure 5.5 shows bar plots of directional error, velocity magnitude nRMSE and the mean of the absolute value of divergence. The noisy reference, inverse FT (IFT), CS and divergence-regularized data (DFW, FD) are compared to the noise-free reference. Relative to CS, phase regularization reduces the directional error. For $R = 6$ directional errors become smaller for each method when compared to $R = 3$. This is consistent with the vector field plots shown in Figure 5.4. However, for the velocity magnitude nRMSE, error levels increase with increasing acceleration factor and are only slightly reduced by phase regularization. In contrast, a clear reduction in mean absolute

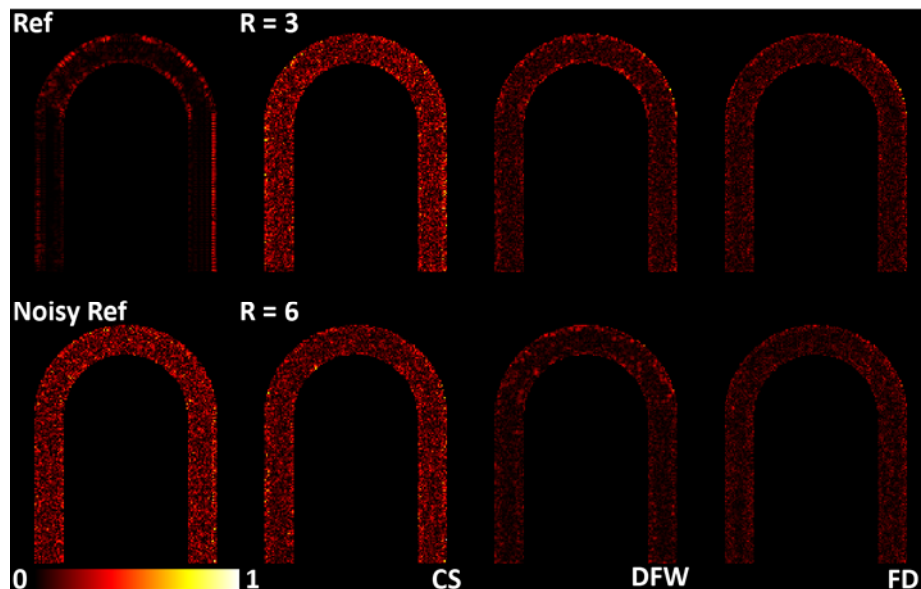


Figure 5.3 Absolute value of normalized velocity vector field divergence of the numerical phantom for CS, DFW and FD reconstructions from 3- and 6-fold undersampled data relative to noise-free and noisy references.

divergence by DFW and FD relative to standard CS is seen. In agreement with the directional error, divergence is also decreased for larger R with all reconstruction methods. The SNR dependence of mean absolute divergence reveals overall improvement of vector field reconstruction with DFW and FD regularization relative to CS for all SNR values tested. At low SNR values, FD-based divergence reduction is seen to outperform DFW regularization. Mean absolute divergence of the in vivo data is presented in Figure 5.5e comparing fully sampled reference, IFT, CS, DFW- and FD-phase-regularized reconstructions. Relative to standard CS, DFW reduced the mean absolute divergence of the flow field by 44.8% and 50.9% for three- and six-fold undersampling, respectively. Corresponding numbers for FD phase regularization are 50.6% and 54.2%. CS already decreased divergence to or even below the reference level. In vivo results also confirm the reduction of divergence with increasing scan acceleration as observed in the computer phantom. Figure 5.5f illustrates reconstructed divergence maps of an exemplary in vivo case covering ascending and descending aorta relative to the fully sampled reference data.

Figure 5.6 shows in-plane velocity vector field components in the indicated cross-section through the ascending aorta and pulmonary artery of a healthy volunteer. The background image represents velocity magnitude. Relative to the reference, denoising of the flow field is already obtained using CS, confirming the divergence statistics in Figure 5.5. Further reduction in divergence is reflected by smoother vector fields upon reconstruction with DFW and FD regularization.

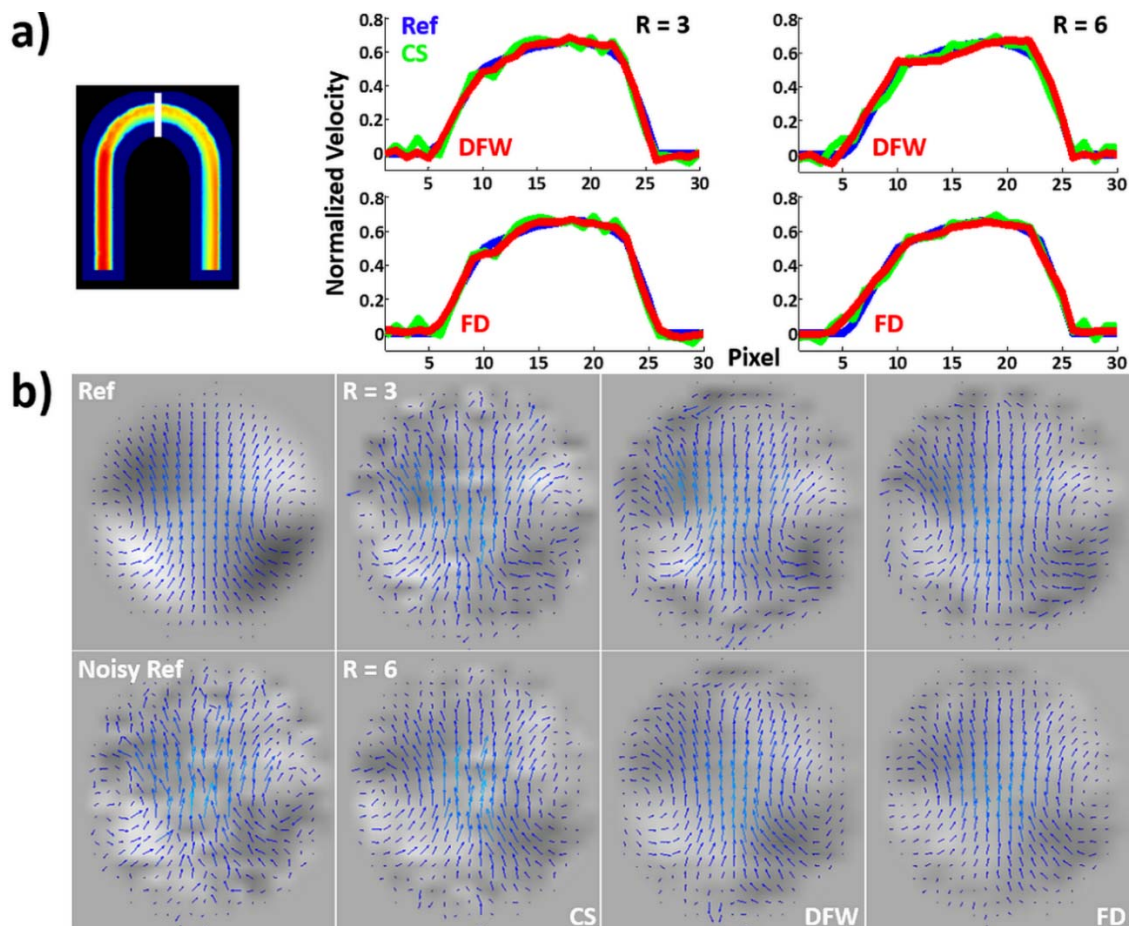


Figure 5.4 *Through-plane velocity profiles a) and in-plane velocity vectors b) across indicated line for CS (green profile line), DFW and FD (red profile lines) reconstructions from 3- and 6-fold undersampled data of the numerical phantom relative to reference data (blue profile line).*

Figure 5.7 illustrates in-plane flow field components of the patient data set. Noise reduction of the in-plane velocity vectors with DFW and FD regularization is seen relative to CS.

Figure 5.8 shows in-plane vector fields of the patient measurement. Besides divergence reduction relative to CS, the indicated vortex formation is better recovered by DFW and FD.

In Table 5.2a, relative errors of peak and total flow in the aortic arch for IFT, CS, DFW and FD reconstructions are compared to the fully sampled reference data in the healthy cohort. Increasing the undersampling factor leads to increased underestimation of peak and total flow with similar results for CS, DFW and FD reconstruction. Corresponding Bland-Altman and linear correlation plots can be found in the Appendix Section 5.6.2.

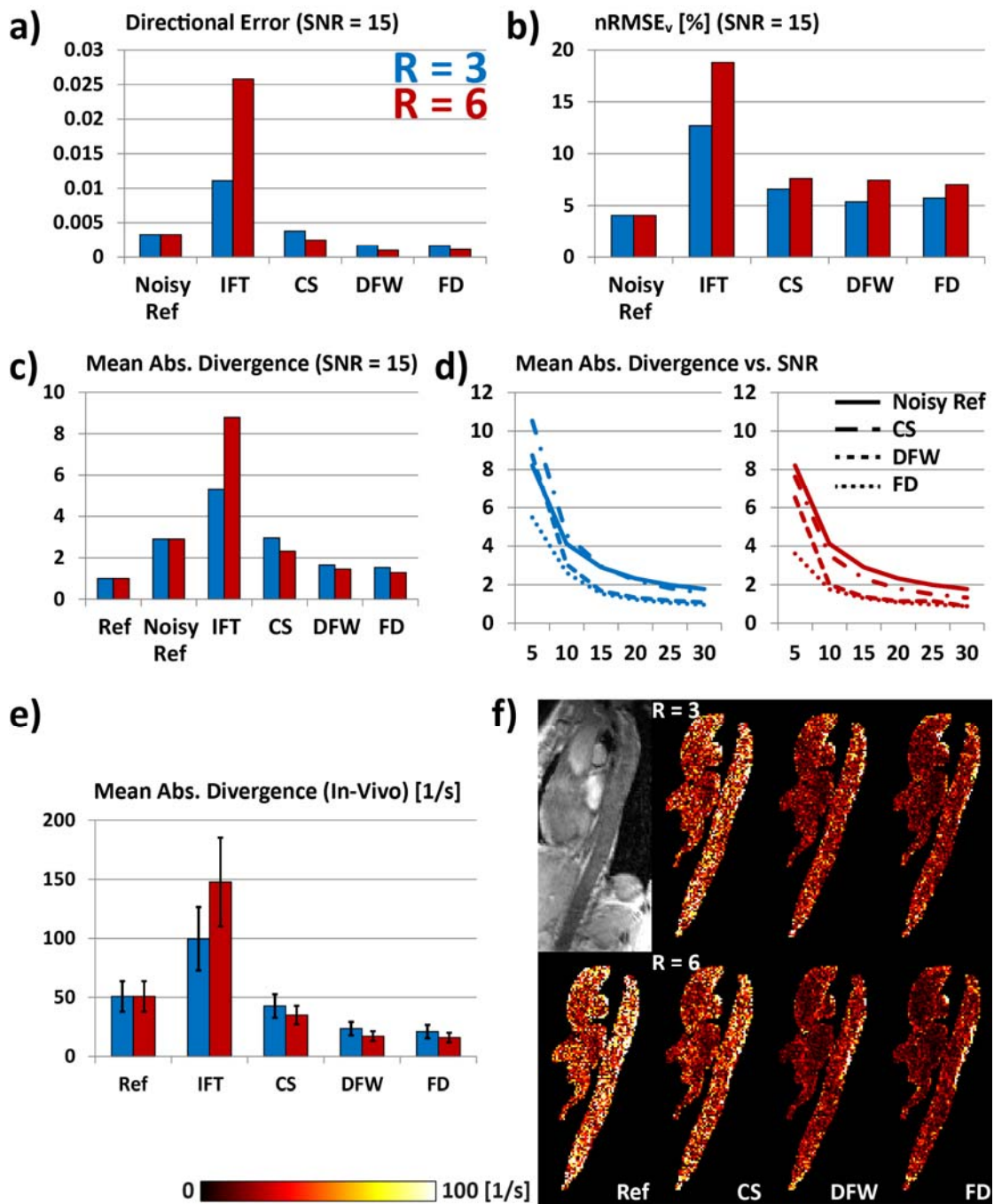


Figure 5.5 Comparison of directional error **a)**, $nRMSE$ of velocity magnitude **b)**, mean of absolute divergence **c)** and the dependency of divergence reduction on SNR **d)** for the numerical phantom. Comparison of mean absolute divergence in volunteer cohort **e)**. Example data of divergence maps in systole for the different reconstruction approaches **f)**.

Improvements in streamline visualization were measured by comparing streamline lengths as well as the number of streamlines arriving at their expected end point in the volunteer data relative to the fully sampled data (Table 5.2b). Streamlines were seeded after the aortic arch in the superior descending aorta, and then the lengths were measured as well as the number of

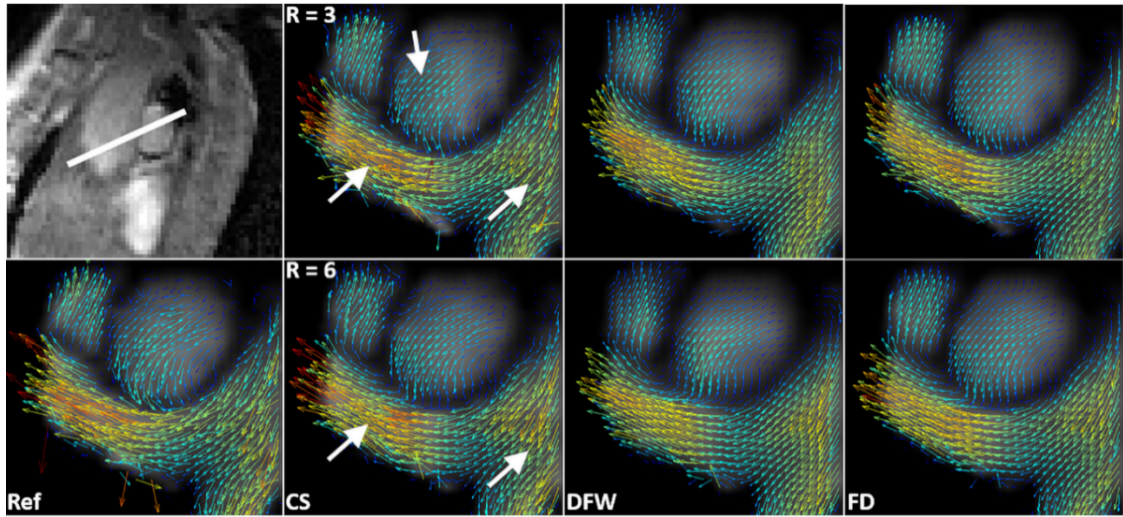


Figure 5.6 In-plane velocity field visualization in a cross-section at the line indicated in a healthy subject. Comparison of CS, DFW and FD reconstructions relative to fully sampled reference data for 3- (top) and 6-fold (bottom) undersampling. The arrows point to differences between CS, DFW and FD reconstructions.

lines crossing a plane at the inferior end of the descending aorta. Relative to standard CS, streamline lengths with DFW were 6.99% and 12.85% longer ($R = 3$ and $R = 6$). Streamline lengths with FD reconstruction were 19.95% and 19.41% longer. The number of streamlines crossing the target plane increased by 18.69% and 24.87% ($R = 3$ and $R = 6$) for DFW relative to CS, while FD improved this measure by 55.12% and 51.86%, respectively.

5.5 Discussion

In this work, physical prior knowledge about 3D blood flow has been incorporated into a CS-based reconstruction of undersampled 4D flow MRI data. Using a separate magnitude/phase reconstruction framework, FD divergence and curl operators have been incorporated for ℓ_1 -regularization of velocity encoded phase differences. An efficient reconstruction algorithm based on variable splitting was implemented for the non-convex phase image updates. Additionally, divergence-free vector Wavelet regularization alternating between Wavelet coefficient shrinkage and k-space data fidelity was tested. All methods were applied to simulated CFD-based 3D PC data of a U-bend and 4D flow in vivo data of the aortic arch, and compared to standard CS reconstruction.

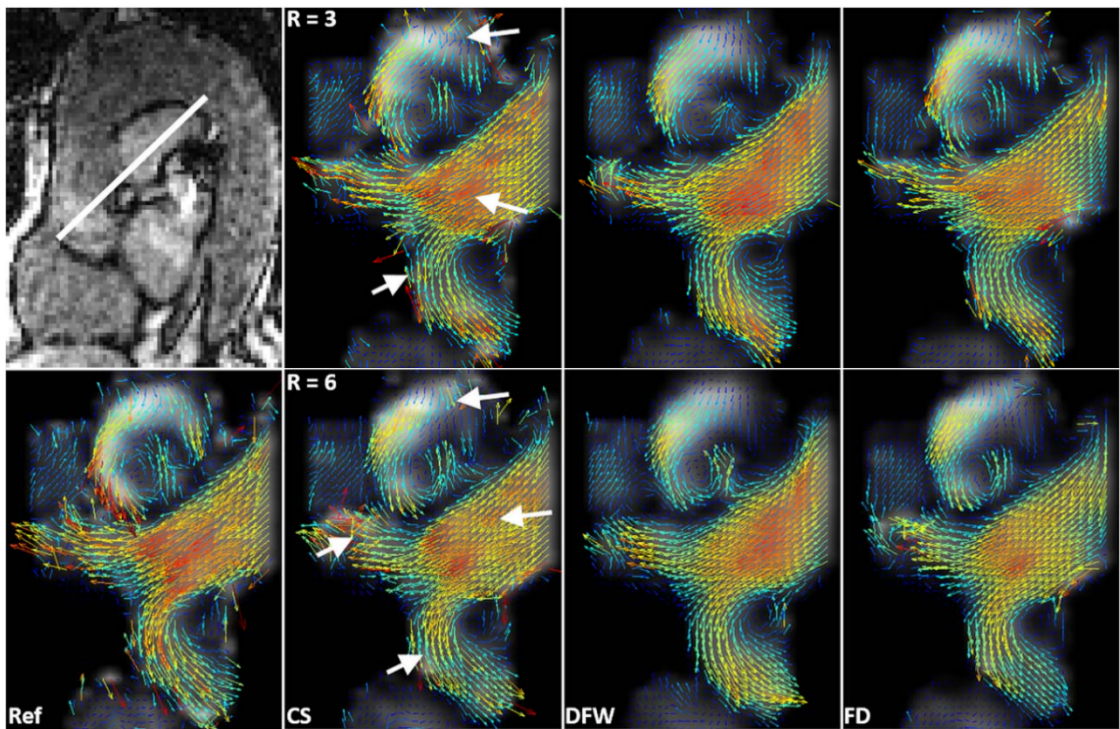


Figure 5.7 In-plane velocity field visualization in a cross-section at the line indicated in the patient magnitude image. Comparison of CS, DFW and FD reconstructions relative to fully sampled reference data for three- (top) and six-fold (bottom) undersampling. The arrows point to differences between CS, DFW and FD reconstructions.

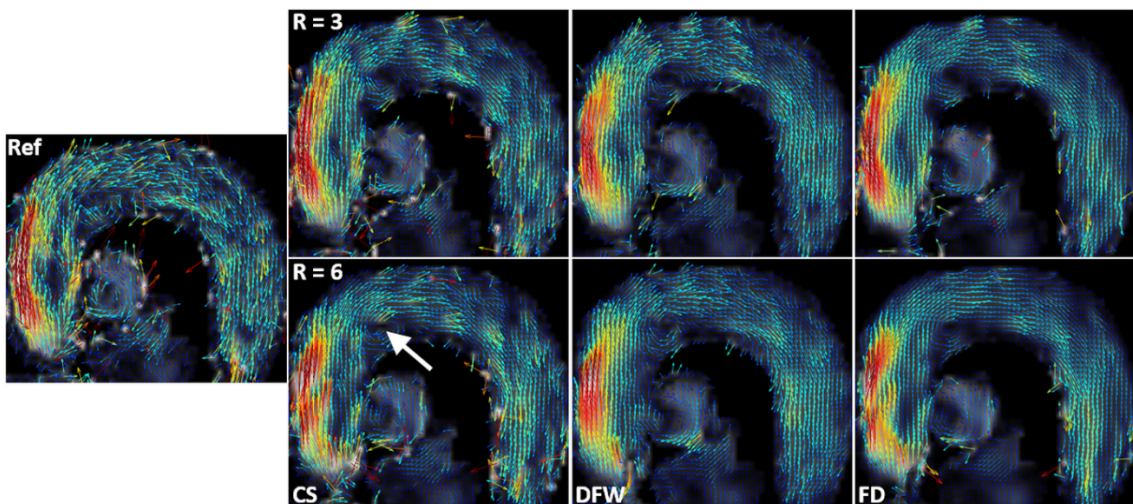


Figure 5.8 In-plane vector field components in slice through the aortic arch of the patient data. CS, DFW, and FD reconstruction results are compared to the fully sampled reference image for three- (top) and six-fold (bottom) acceleration. The arrow highlight the vortex in the flow field.

a)		R = 3		R = 6	
Method	Total Flow [%]	Peak Flow [%]	Total Flow [%]	Peak Flow [%]	
IFT	-17.37 ± 34.30	-19.63 ± 40.16	-65.13 ± 123.64	-65.63 ± 121.68	
CS	-3.74 ± 6.55	-2.42 ± 5.20	-7.24 ± 11.13	-4.45 ± 11.53	
DFW	-5.53 ± 9.61	-3.09 ± 10.26	-8.89 ± 15.84	-5.12 ± 17.41	
FD	-4.57 ± 8.56	-3.52 ± 8.61	-8.19 ± 15.88	-6.03 ± 13.60	

b)		R = 3		R = 6	
Method	Streamline Length [%]	Streamline Plane Crossing [%]	Streamline Length [%]	Streamline Plane Crossing [%]	
IFT	-22.96	-89.31	-43.56	-95.13	
CS	-0.43	-14.81	2.54	-12.86	
DFW	6.56	3.88	15.39	12.01	
FD	19.52	40.31	21.95	39.00	

Table 5.2 a) *Relative error (mean ± 1.96 x standard deviation) of peak flow and total flow measurements for IFT, CS, DFW and FD reconstructions relative to the fully sampled reference data in the five volunteer data sets.* b) *Relative change in streamline length and number of streamlines reaching the end of the descending aorta in comparison to the fully sampled reference data.*

The CFD phantom with added noise revealed improvement in velocity vector field assessment when using DFW or FD phase regularization relative to standard CS. Velocity magnitude images showed that FD and DFW regularization efficiently reduces undersampling and noise-like artifacts. Divergence was clearly reduced in the flow regime by separate magnitude and phase reconstruction relative to the standard CS method. Overall improvement in velocity vector field visualization was also demonstrated for 3- and 6-fold acceleration. Reduction in directional error and divergence was found to be most prominent when using phase regularization. Error levels for velocity magnitude were shown to be similar or slightly below standard CS. The increased error reduction of velocity direction compared to magnitude is due to the proposed phase regularizers which impose a penalty on velocity direction rather than on magnitude. Using variable-density random undersampling, data consistency is mainly enforced for low frequency spatial harmonics favoring smooth phase maps, while recovering high frequency components relies on model assumptions to a larger degree. Thus, reconstructed vector fields are increasingly

denoised/regularized in conjunction with standard Wavelet denoising (convex CS) or divergence penalization (DFW, FD), thereby favoring direction dependent error metrics (directional error and absolute mean divergence) at higher undersampling factors.

The spatial derivative operators applied on relatively low spatial resolution data with regard to the spatial extent of local peak flow and specific flow patterns further compromise the underestimation of total and peak flow amplitudes relative to standard CS. In order to improve the measurement accuracy of peak flow and flow jets, better reconstruction of high frequency components is required. In future work, optimal sampling patterns to recover peak flow need to be derived. In the current work, a sampling pattern common in standard CS has been chosen to enable a fair comparison with convex CS. Furthermore, the gain in scan efficiency due to undersampling should be investigated to improve spatial resolution, thereby reducing the influence of discrete spatial derivative operators.

For DFW phase regularization, coarse masking of the blood pool prior to application of the Wavelet filter banks resulted in minor improvements of denoising performance, while FD reconstruction was not affected by masking.

In vivo experiments confirmed the observation of reduced divergence with increasing undersampling in conjunction with variable-density sampling. Relative to standard CS, DFW and FD phase regularization, both led to a reduction in mean absolute divergence within the flow volumes, while divergence was least for FD. Vector field visualization and streamline quantification were improved by divergence regularization. Similar to post-processing techniques [178], vector field denoising by divergence-free reconstruction was confirmed by longer streamlines relative to the noisy fully sampled data. The assessment of peak flow revealed an underestimation by 2.4, 3.1, 3.5% ($R = 3$) and 4.5, 5.1, 6.0% ($R = 6$) for CS, DFW and FD.

The initialization of the non-convex reconstruction algorithms with a good solution estimate turned out to be crucial, and thus, a few preceding convex CS iterations were necessary. Due to the increased number of reconstruction parameters relative to standard CS, a limitation of this work is the lack of a fully optimized parameter set, which may also be a potential source of comprising the accuracy of the in vivo total and peak flow measures. In [180], a data-adaptive threshold selection procedure was applied to DFW denoising. However, this relied on the assumption of Gaussian distributed noise of the vector field components and for undersampled data reconstruction, manually tuned thresholds were used.

While the DFW reconstruction was significantly faster (3x) than FD, the FD regularization performed slightly better than the DFW regularizer for most metrics. However, at this point we

cannot recommend one method over the other, and thus, further data need to be acquired to conclude on the preferred approach.

In the present work, variable splitting was used to divide FD phase regularization into smaller sub-problems which were easier to solve (in terms of implementation and computational load) than direct minimization. However, each auxiliary variable comes at the expense of an additional regularization parameter weighting the added quadratic term. While in convex problems, the solution is not affected by these parameters influencing only the convergence rate [184], a detailed analysis of their effect in non-convex reconstruction is a remaining task.

Errors due to eddy currents in PC MRI lead to low-order phase offsets across the entire imaging volume. The addition of this phase offset in a vessel can potentially create non-stochastic divergence in the measured velocity fields, which will then be removed by divergence-free methods. Divergence-free methods will therefore correct some portion of eddy current errors, but with the potential of increasing or decreasing flow values. Our experiments showed no significant errors in total flow measurements, so the negative effects of removing the divergent portion of coherent phase errors appears to be negligible. However, magnetic field monitoring can be used if eddy current-related phase offsets need to be addressed explicitly [53]. The phase offset maps obtained from a short calibration scan can then directly be included in the velocity field reconstruction.

In summary, the incorporation of the divergence-free condition directly into the reconstruction via separate magnitude and phase regularization is a promising tool to enhance accelerated 4D flow MRI. Improved 3D velocity field reconstruction and visualization have been demonstrated on simulated CFD and in vivo data. To prove robustness of the methods in a clinical setting or their applicability to other vascular regimes, studies in larger cohorts are needed.

5.6 Appendix

5.6.1 Gradient and Hessian

The gradient ∇ and Hessian ∇^2 of the function $g(\boldsymbol{\phi}) = (\mu_1 / 2) \|\mathbf{y}_1 - e^{i\boldsymbol{\phi}}\|_2^2 + (\mu_2 / 2) \|\mathbf{y}_2 - \boldsymbol{\Psi}_{div, curl} \mathbf{K}_v \boldsymbol{\phi}\|_2^2$ with $\mathbf{y}_1 = \mathbf{u}_1^{n+1} - \mathbf{b}_1^n$ and $\mathbf{y}_2 = \mathbf{u}_2^{n+1} - \mathbf{b}_2^n$ are given by [181]:

$$\nabla g(\boldsymbol{\phi}_v) = \mu_1 \operatorname{Re}\{(ie^{-i\boldsymbol{\phi}_v}) \circ \mathbf{y}_1\} - \mu_2 \mathbf{K}_v^T \boldsymbol{\Psi}_{div, curl}^T (\mathbf{y}_2 - \boldsymbol{\Psi}_{div, curl} \mathbf{K}_v \boldsymbol{\phi}_v). \quad (5.19)$$

$$\nabla^2 g(\boldsymbol{\phi}_v) = \mu_1 \operatorname{Re}\{diag(e^{-i\boldsymbol{\phi}_v} \circ \mathbf{y}_1)\} + \mu_2 \mathbf{K}_v^T \boldsymbol{\Psi}_{div, curl}^T \boldsymbol{\Psi}_{div, curl} \mathbf{K}_v. \quad (5.20)$$

First and second derivative needed to optimize the step size α during the line search along direction \mathbf{e} are then given by $f'(\alpha) = \mathbf{e}^T \nabla g(\boldsymbol{\phi}_v + \alpha \mathbf{e})$ and $f''(\alpha) = \mathbf{e}^T \nabla^2 g(\boldsymbol{\phi}_v + \alpha \mathbf{e}) \mathbf{e}$, which reduce to element-wise vector, diagonal matrix and inner products.

5.6.2 Peak and Total Flow Bland-Altman Plots

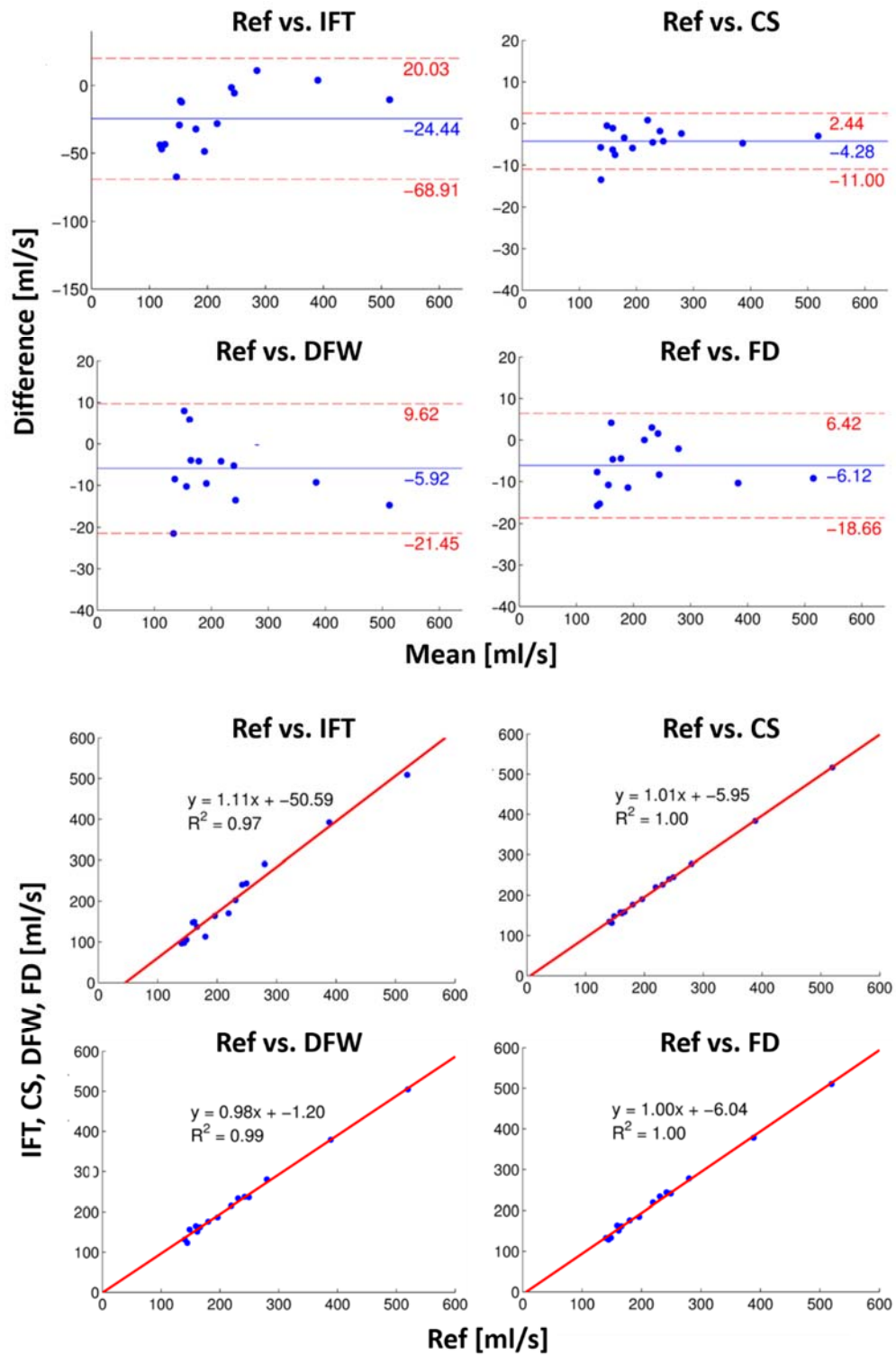


Figure 5.9 Bland-Altman and linear correlation plots of peak flow measurements ($R = 3$).

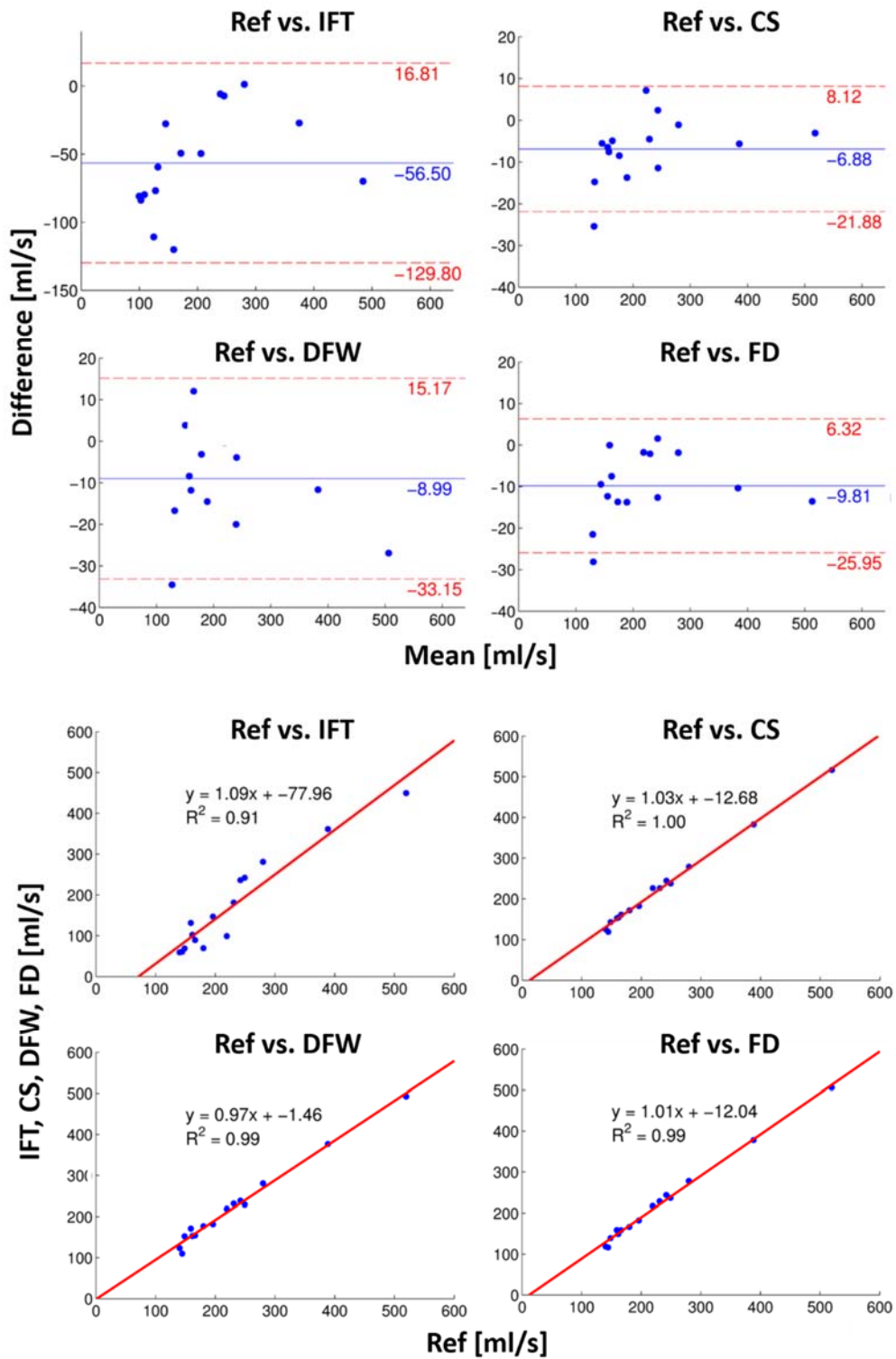


Figure 5.10 Bland-Altman and linear correlation plots of peak flow measurements ($R = 6$).

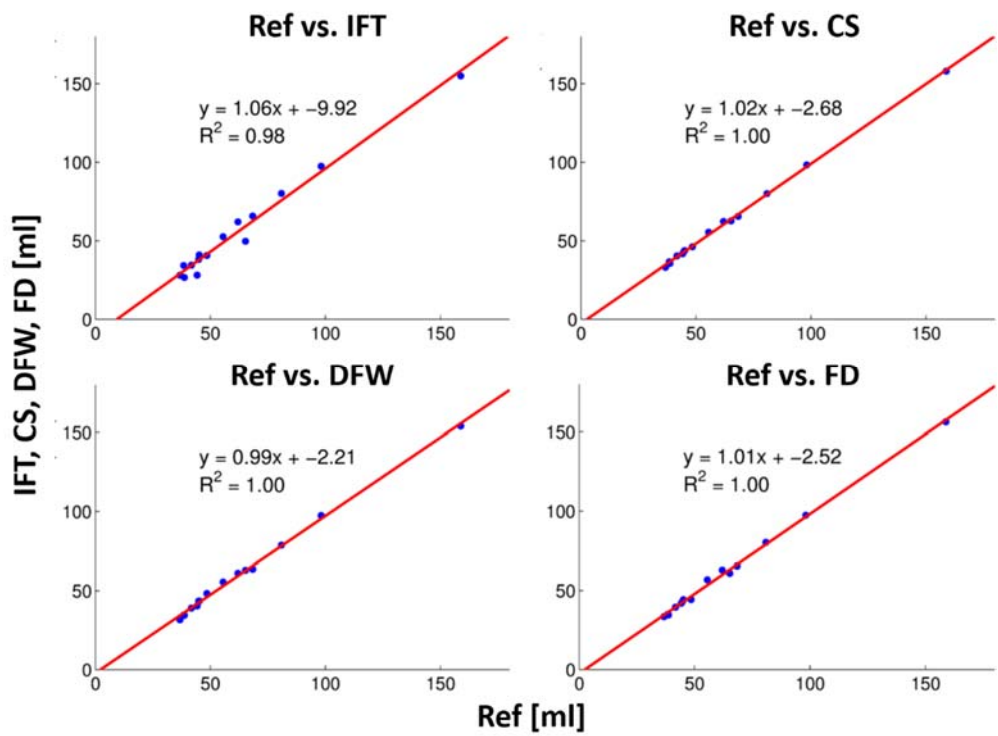
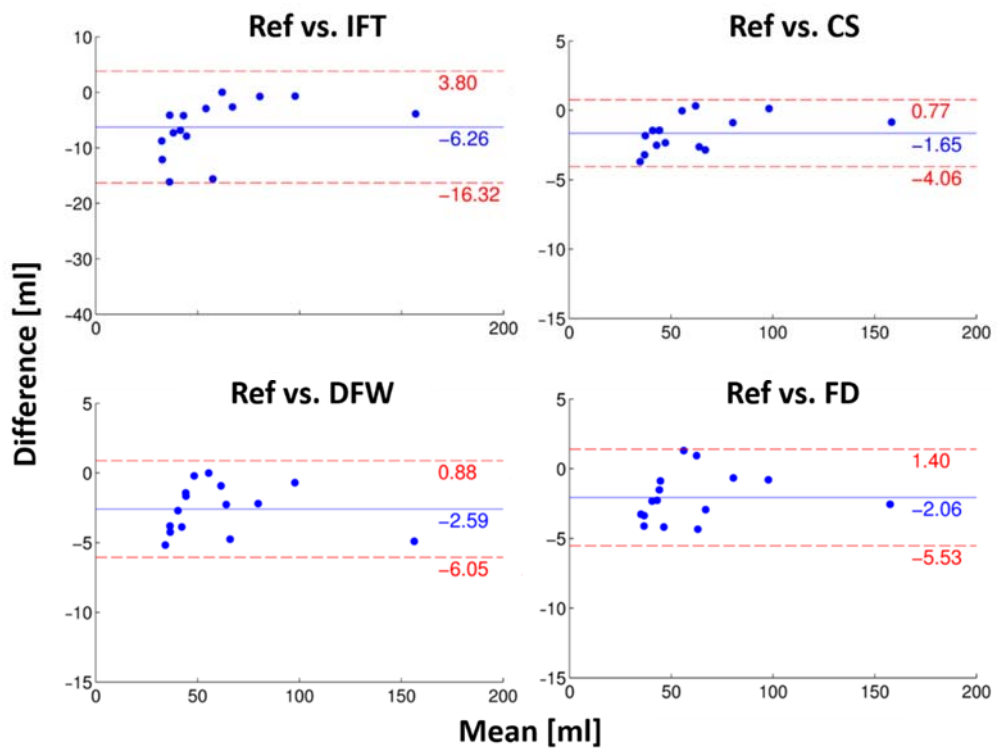


Figure 5.11 Bland-Altman and linear correlation plots of total flow measurements ($R = 3$).

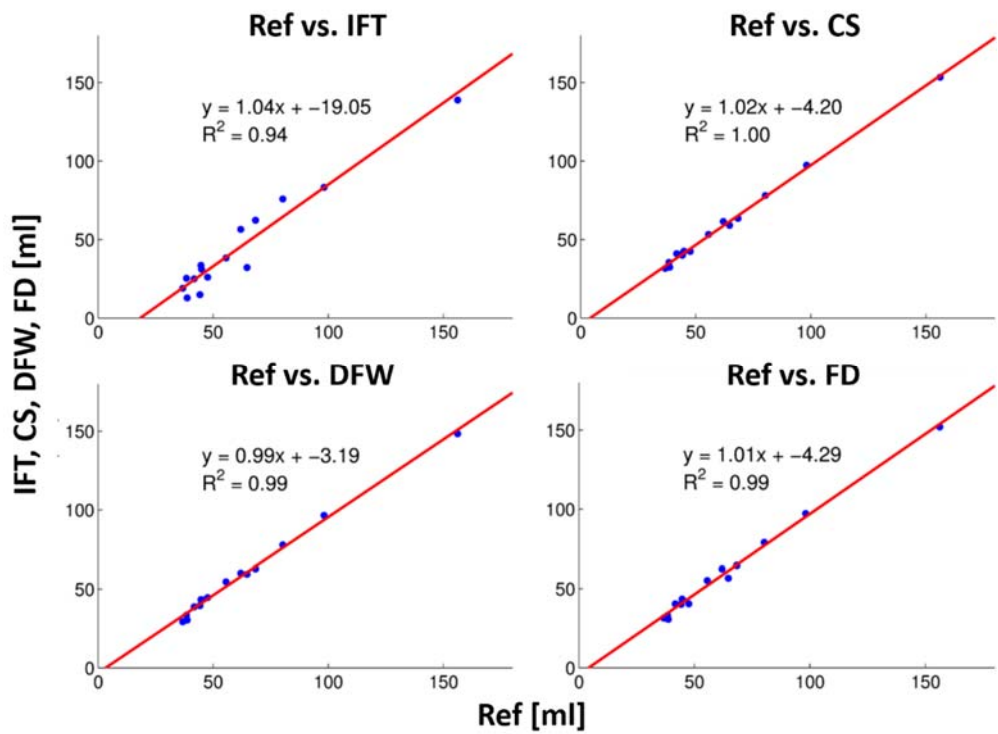
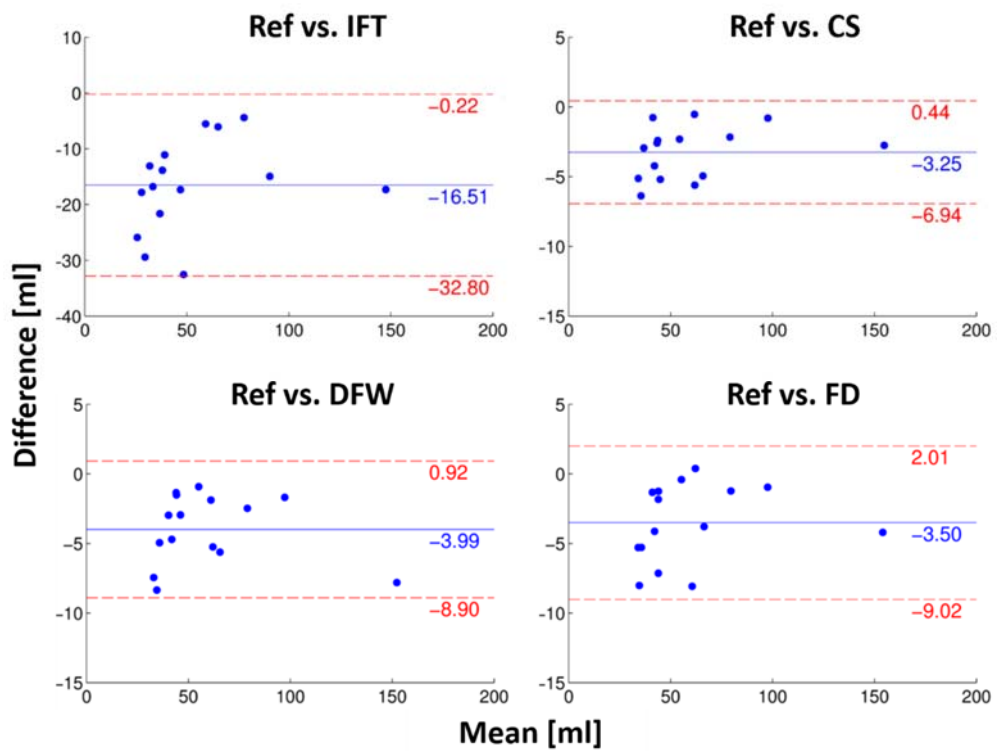


Figure 5.12 Bland-Altman and linear correlation plots of total flow measurements ($R = 6$).

Chapter 6

Optimized SPIRiT, Motion Correction and Sampling

6.1 Efficient SPIRiT Reconstruction*

SPIRiT (Section 3.1.3) is an auto-calibrating parallel imaging (PI) method for arbitrary k-space trajectories generalizing GRAPPA (Section 3.1.2). The computational complexity of the calibration operator has been reduced from $O(N_c^2)$ to $O(N_c)$ (N_c : number of coils) by extracting coil sensitivity maps via eigendecomposition (3.8) of the image-based interpolation kernel [69]. In [69] only the forward operation of the modified kernel has been used in a projection onto convex sets algorithm for Cartesian sampling. However, general gradient-based iterative solvers, e.g. conjugate gradients (CG) for non-Cartesian sampling also include adjoint besides forward operations.

Here we propose to reduce the computational complexity for non-Cartesian SPIRiT by incorporating the coil sensitivity-based kernel into CG-like reconstruction. Additionally, the two consecutive k-space interpolation steps during the regridding-gridding operation are approximated by a diagonal matrix multiplication reducing computational costs further.

In SPIRiT, the k-space interpolation kernel \mathbf{G} can efficiently be implemented in the image domain yielding a matrix-vector multiplication, $\mathbf{p}_n(\mathbf{r}) = \mathbf{G}_x(\mathbf{r})\mathbf{p}_{n-1}(\mathbf{r})$, for each pixel at iteration step n . $\mathbf{p}_n(\mathbf{r})$ denotes the $N_c \times 1$ column vector stacking each coil's image value at voxel position \mathbf{r} , and $\mathbf{G}_x(\mathbf{r})$ is a $N_c \times N_c$ matrix containing the values of the inverse Fourier transformed k-space kernel at \mathbf{r} . The corresponding image-domain operator, acting on all coil images stacked in vector \mathbf{p} , is then

* Based on: C. Santelli, T. Schaeffter and S. Kozerke, "Efficient Non-Cartesian SPIRiT without Explicit Consecutive Regridding and Gridding", Proceedings of the 21st Meeting of ISMRM, Salt Lake City, UT, USA, p. 2643, 2013.

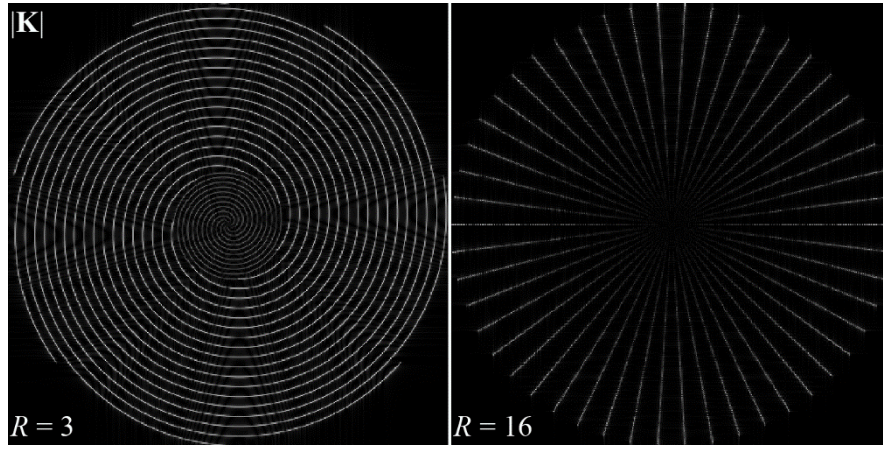


Figure 6.1 \mathbf{K} matrices of undersampled spiral (left) and radial (right) trajectories with acceleration factor R .

denoted as \mathbf{G}_x . It has been shown in [69] that the voxel-wise $O(N_c^2)$ matrix multiplication can be reduced to a successive $O(N_c)$ vector-vector and scalar-vector multiplication: $\mathbf{G}_x(\mathbf{r}) \approx \|\mathbf{c}(\mathbf{r})\|_2^{-2} \mathbf{c}(\mathbf{r})\mathbf{c}(\mathbf{r})^H$, where $\mathbf{c}(\mathbf{r})$ is the coil sensitivity vector corresponding to the eigenvector of $\mathbf{G}_x(\mathbf{r})$ with eigenvalue 1. Defining the modified operator as

$$\mathbf{C}_x(\mathbf{r}) \equiv \|\mathbf{c}(\mathbf{r})\|_2^{-2} \mathbf{c}(\mathbf{r})\mathbf{c}(\mathbf{r})^H \quad (6.1)$$

and \mathbf{C} for voxel-by-voxel and whole multi-coil image vector processing, respectively, it is seen that $\mathbf{C}_x(\mathbf{r})^H = \mathbf{C}_x(\mathbf{r})$ and $\mathbf{C}^H = \mathbf{C}$. With the identity \mathbf{I} , the calibration consistency and its adjoint operation appearing as $(\mathbf{G}_x - \mathbf{I})^H(\mathbf{G}_x - \mathbf{I})$ in CG-like reconstruction can then be simplified to

$$(\mathbf{C} - \mathbf{I})^H(\mathbf{C} - \mathbf{I}) = -(\mathbf{C} - \mathbf{I}). \quad (6.2)$$

Following [186], the regridding-gridding operation $\mathbf{E}^H\mathbf{E}$ with the encoding matrix \mathbf{E} of the data consistency term is replaced with

$$\mathbf{E}^H\mathbf{E} \approx \mathbf{I}_{zp}^T \mathbf{F}^H \text{diag}(\mathbf{F}_0\mathbf{Q})\mathbf{F}\mathbf{I}_{zp}, \quad (6.3)$$

with the zero-padding matrix \mathbf{I}_{zp} , doubling the image matrix dimensions, the unitary FT matrix \mathbf{F} , the non-unitary FT \mathbf{F}_0 , and \mathbf{Q} as defined in [186]. Instead of calculating \mathbf{Q} according to [186], $\text{diag}(\mathbf{F}_0\mathbf{Q})$ is approximated by another diagonal matrix \mathbf{K} . Similar to [187], \mathbf{K} is obtained by regridding a constant ones k-space onto the non-Cartesian trajectory followed by gridding back onto the Cartesian grid (Figure 6.1). Combining the two approaches, the normal equation to solve the image-domain minimization problem (3.7) reduces to:

$$\left[\mathbf{I}_{zp}^T \mathbf{F}^H \mathbf{K} \mathbf{F} \mathbf{I}_{zp} - \lambda^2 (\mathbf{C} - \mathbf{I}) \right] \boldsymbol{\rho} = \mathbf{E}^H \mathbf{d}, \quad (6.4)$$

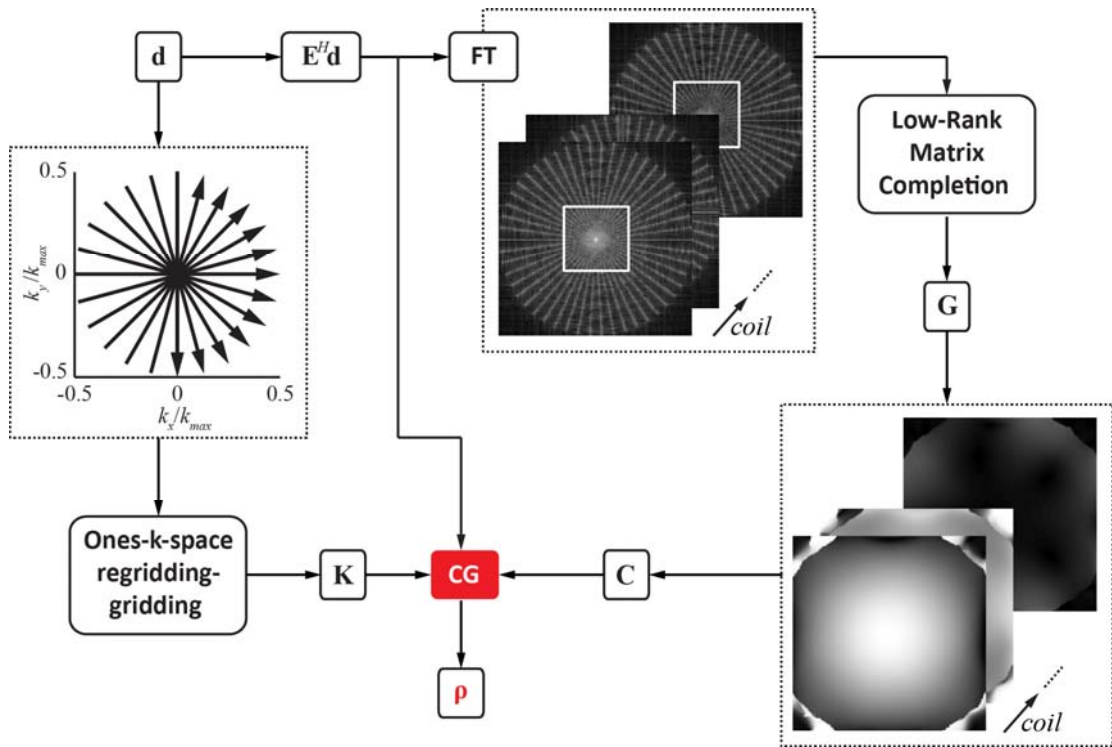


Figure 6.2 Reconstruction workflow. \mathbf{K} is obtained via the geometry of the undersampled trajectory. The calibration operators \mathbf{G} and \mathbf{C} are calculated from the center of k -space via low-rank matrix completion and eigendecomposition of the corresponding image-domain matrix \mathbf{G}_x , respectively.

with the arbitrary k -space trajectory \mathbf{d} and regularization parameter λ .

To test the approach, an artificial 16-channel coil array data set [188] was used to generate a reference multi-coil computer model data set. Complex-valued white Gaussian noise with independent real and imaginary part was added. Eight virtual channels were computed using coil array compression [188]. The reference data (256 x 256 matrix) were projected onto undersampled spiral and radial k -space trajectories. For both sampling schemes, a fully sampled k -space center (30 x 30) for calibrating \mathbf{G}_x with a 7 x 7 kernel was calculated via low-rank matrix completion [189]. \mathbf{C} was obtained by eigendecomposition of \mathbf{G}_x and \mathbf{K} using regridding and gridding of a (256 x 256) ones k -space (Figure 6.2). CG with 40 iteration steps was then used for reconstruction, once with \mathbf{G}_x and \mathbf{E} for standard SPIRiT, once with the new operators \mathbf{C} and \mathbf{K} , and once with \mathbf{C} and \mathbf{E} . To implement \mathbf{E} , the NUFFT griddler [35] was used.

Figure 6.3 shows reference, direct IFT, SPIRiT reconstructed and error images for the simulated spiral and radial data. The masked error images depict the equality of using operator \mathbf{G}_x or \mathbf{C} , and \mathbf{E} or \mathbf{K} . Compared to standard spiral SPIRiT with \mathbf{G}_x/\mathbf{E} , the saving in reconstruction time when using \mathbf{C}/\mathbf{K} and \mathbf{C}/\mathbf{E} was 43% and 40%, respectively. For radials, the corresponding time savings

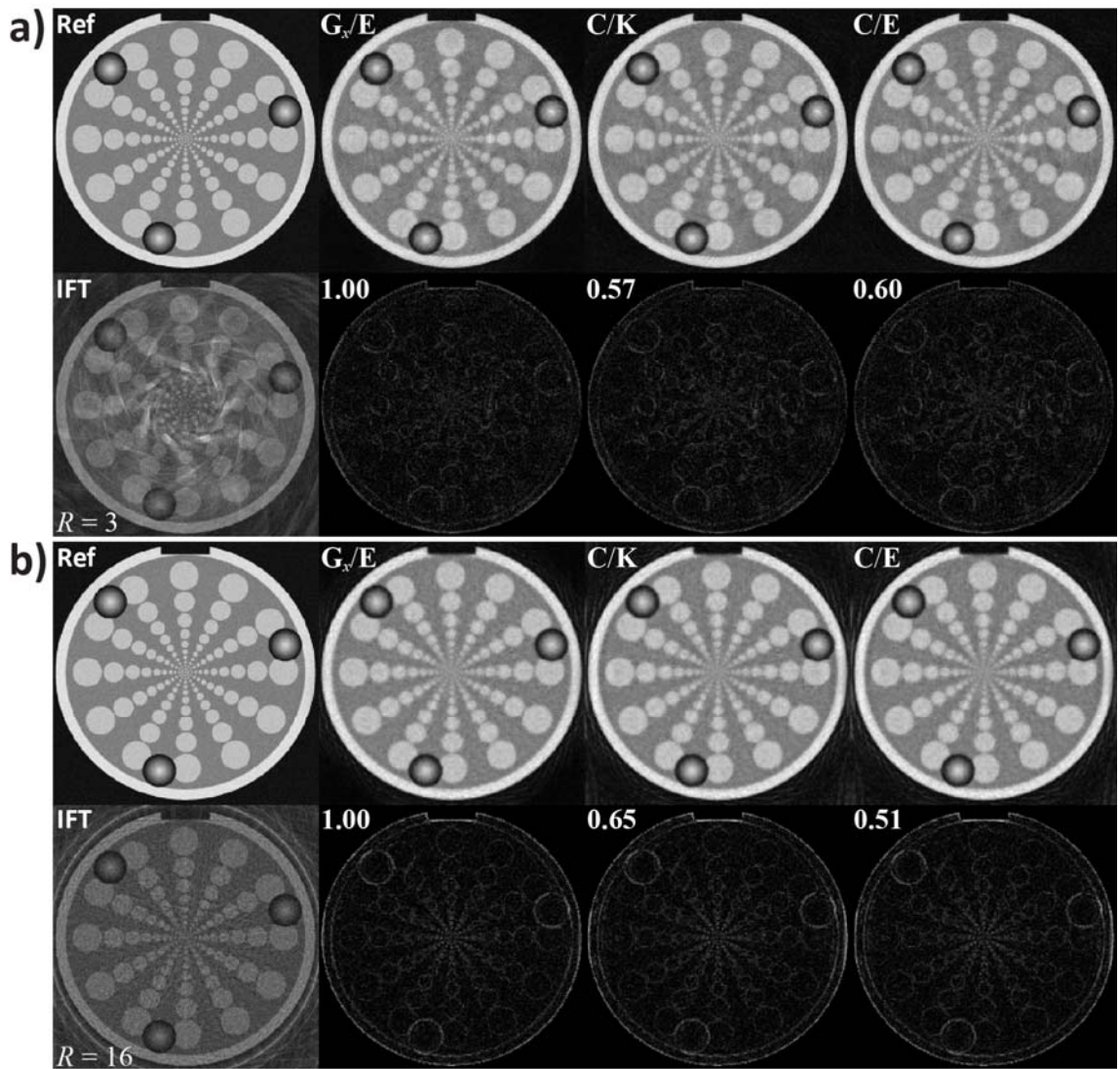


Figure 6.3 a) Coil-combined reference and gridded 3-fold undersampled spirals. Reconstructed and error images shown for standard SPIRiT with operators \mathbf{G}_x and \mathbf{E} and for the proposed method using operators \mathbf{C} and \mathbf{K} or \mathbf{C} and \mathbf{E} . Reconstruction times relative to standard SPIRiT (1.0) are given. b) Corresponding images for 16-fold undersampled radial data set.

were 35% and 49%, revealing that the benefit of \mathbf{K} depends on the number of acquired k-space samples.

In summary, significant reduction in reconstruction time has been achieved for spiral and radial data reconstruction using computationally optimized SPIRiT. In addition, the exchangeability of the two consecutive k-space interpolation steps with a diagonal matrix multiplication has been shown. Depending on the number of k-space samples, reconstruction time savings by a factor of 1.5-2 have been demonstrated.

6.2 SPIRiT^{mc} – Auto-Calibrating Parallel

Imaging with Non-Rigid Motion Correction*

Scan acceleration and motion-compensating techniques are invaluable to reduce acquisition times and breathing artifacts in cardiac imaging. Respiratory motion compensation with navigator (NAV) gating or breath-holding is widely used, but the approaches may be limited in non-compliant patients (Section 3.4). Based on the matrix formulation of general motion correction (Section 3.4.3) [128], various approaches have been presented permitting data acquisition during free breathing of the subject [130, 131]. It has also been demonstrated that the method can be combined with different undersampling techniques [25, 120, 132]. Among the PI portfolio, SPIRiT (Section 3.1.3) [23] has gained interest as an auto-calibrating PI technique for arbitrary k-space trajectories generalizing GRAPPA (Section 3.1.2) [63]. Here, the SPIRiT reconstruction framework is extended by incorporating a linear motion operator into the signal model allowing for scanning during the entire breathing cycle in cardiac imaging. Simulation and in vivo data demonstrate the benefits of the technique.

In SPIRiT, a Cartesian multi-coil image \mathbf{p} is reconstructed by minimizing (3.7). The data consistency term is extended with a bilinear interpolation matrix \mathbf{T} warping the coil images into the different motion states corresponding to the respiratory positions during data acquisition:

$$\|\mathbf{d} - \mathbf{E}\mathbf{T}\mathbf{p}\|_2^2 + \lambda^2 \|(\mathbf{G}_x - \mathbf{I})\mathbf{p}\|_2^2 + R(\mathbf{p}). \quad (6.5)$$

The encoding operator then maps the motion state images to the acquired profiles.

Dynamic short-axis view data (256 x 256 image matrix) were generated from the MRXCAT human anatomy model [190] simulating realistic cardiac and non-rigid respiratory motion. Thirty cardiac phases of 30 ms each, covering the whole cardiac cycle, were calculated for a number of heart beats corresponding to an undersampling factor R relative to radial Nyquist. Complex-valued coil sensitivities and Gaussian noise (resulting in a signal-to-noise ratio (SNR) of 30) were added. The dynamic 8-coil array data were then projected onto a 2D Golden angle (GA) radial trajectory [38] with a TR of 3 ms per profile (Figure 6.4). Fully sampled 2D radially (GA) encoded 4-point cine PC in vivo data (5 mm NAV window, 250 x 250 mm² field of view (FOV), uniform 200 cm/s velocity

* Based on: C. Santelli, T. Schaeffter and S. Kozerke, "SPIRiT^{mc} – Autocalibrating Parallel Imaging with Non-Rigid Motion Correction", Proceedings of the 21st Meeting of ISMRM, Salt Lake City, UT, USA, p. 3748, 2013.

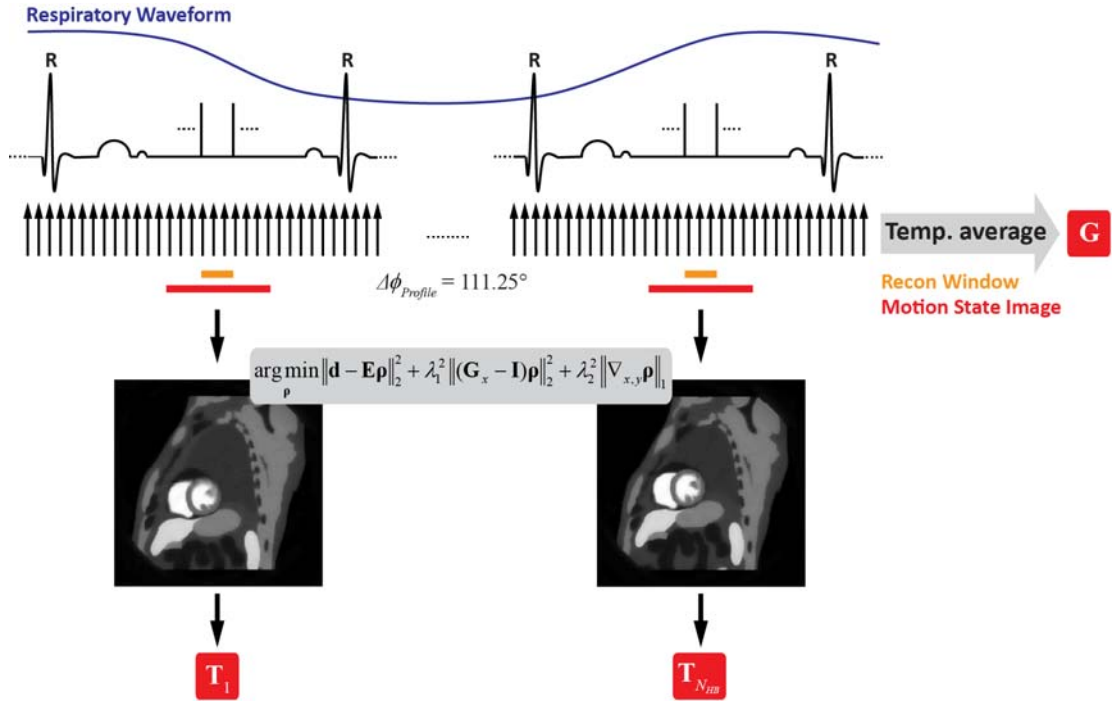


Figure 6.4 2D dynamic short-axis view MRXCAT phantom data simulating cardiac and non-rigid respiratory motion is projected onto a GA trajectory over a number of R-R intervals corresponding to the acceleration factor for a given temporal resolution. The calibration consistency operator for motion state and motion-corrected image reconstruction is derived from an image temporally averaged over all heartbeats. Motion state images are reconstructed using TV-regularized SPIRiT for each heartbeat’s cardiac phases from acquisition windows symmetrically placed around corresponding phase intervals. Upon non-rigid image registration relative to the reference respiratory position, deformation maps are then used to assemble each heart phase’s \mathbf{T} operator.

encoding, $2 \times 2 \times 10 \text{ mm}^3$ voxel size, 5.4/2.9 ms TR/TE, 28 ms temporal resolution) were acquired in a healthy volunteer during free breathing on a 3Tesla Philips scanner (Philips Healthcare, Best, The Netherlands) with six receiver coils. The same scan was repeated without NAV gating during normal free breathing with 4x radial undersampling. In a third scan, the volunteer was advised to breathe deeply, and thus, introducing severe motion artifacts. Reconstruction was performed with and without motion correction using equations (6.5) and (3.7) and with ℓ_1 anisotropic total variation (TV) regularization: $R(\rho) = \|\nabla_{x,y}\rho\|_1$, where $\nabla_{x,y} = [\nabla_x^T \quad \nabla_y^T]^T$ denotes the finite difference-based image gradient operator. The 7×7 k-space interpolation kernels assembling \mathbf{G}_x were fitted to a 30×30 calibration area extracted from a temporal average image of the reduced k-space data. Motion state images at each heartbeat and phase were assigned by reconstructing low-resolution images using equation (3.7) with TV from a 50 projections window around each

heart phase (Figure 6.4). \mathbf{T} was obtained by non-rigid registration of the motion state images relative to a reference heartbeat using the ITK-based elastix framework [191] (Figure 6.4).

Figure 6.5 compares images and temporal profiles of the heart model reconstructed from 4-, 8- and 12-fold radially undersampled data without (SPIRiT) and with motion correction (SPIRiT^{mc}) relative to the fully sampled reference. Figure 6.6 shows a comparison of the in vivo fully sampled NAV-gated reference, SPIRiT^{mc} and SPIRiT reconstructions from 4-fold undersampled data acquired without respiratory gating. Image artifacts induced by respiratory motion were well corrected for with SPIRiT^{mc}. In conjunction with significant undersampling, the method holds considerable potential for accelerating free-breathing cardiac imaging protocols.

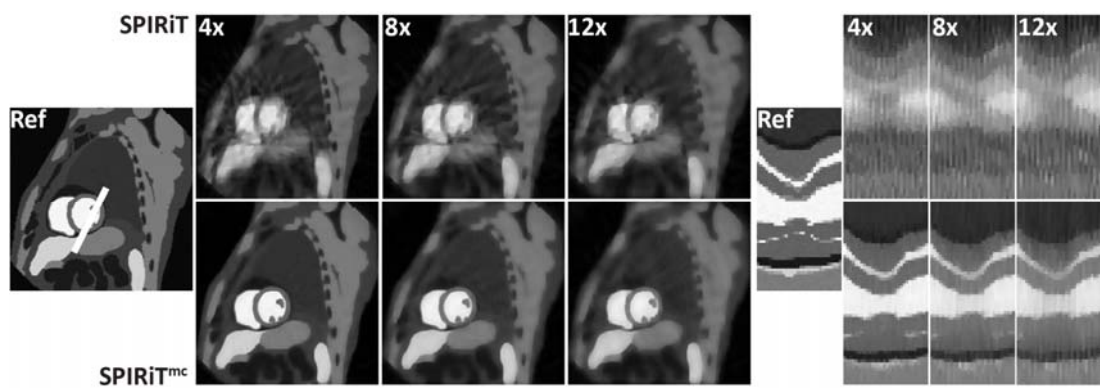


Figure 6.5 Cardiac frame of heart model (Ref) and reconstructed images for different undersampling factors without (SPIRiT, top row) and with (SPIRiT^{mc}, bottom row) motion correction. The corresponding temporal profiles are plotted along the indicated line.

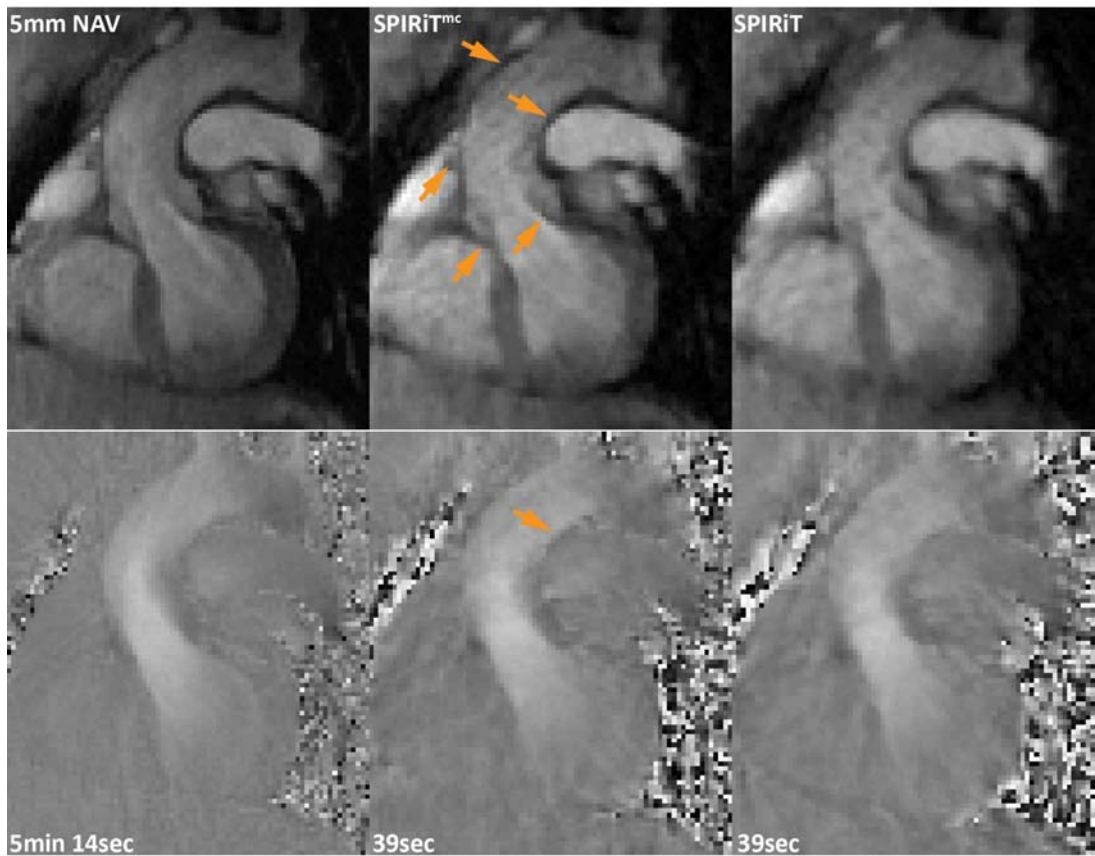


Figure 6.6 Systolic magnitude and in-plane velocity component images of NAV-gated scan (left). Reconstructed images of non-gated 4-fold radially undersampled measurement with (middle) and without (right) motion correction. The arrows point out regions where motion-correcting SPIRiT reduces blurring artifacts. The corresponding acquisition times are also depicted.

6.3 Optimized k - t Sampling for Combined Parallel Imaging and Compressed Sensing*

The combination of PI (Section 3.1) and compressed sensing (CS) (Section 3.2) has shown improved reconstruction performance [23, 79] as compared to applying either of the two methods alone. In many CS approaches, sampling patterns are designed to fully sample the center

* Based on: J. F. M. Schmidt*, C. Santelli* and S. Kozerke, “Optimized k - t Sampling for Combined Parallel Imaging and Compressed Sensing Reconstruction”, Proceedings of the 22nd Meeting of ISMRM, Milan, Italy, p. 4377, 2014. (* denotes shared first authorship)

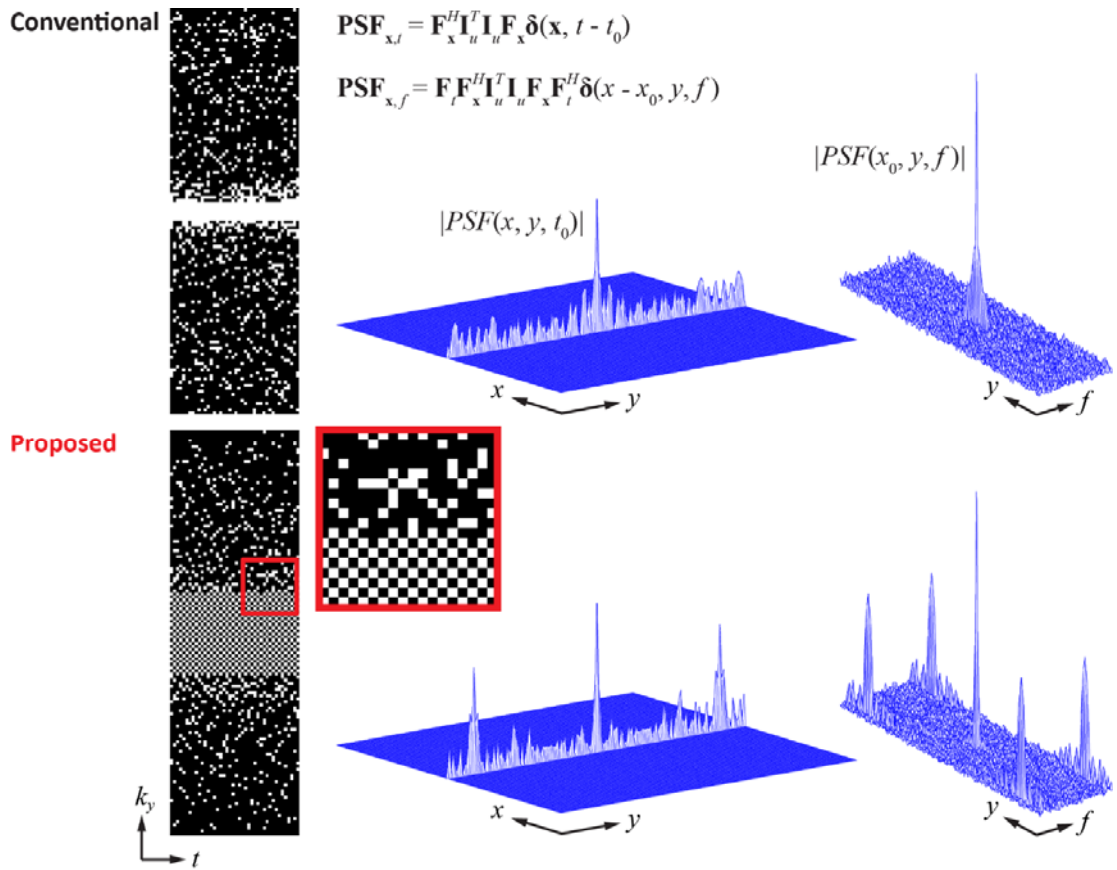


Figure 6.7 Illustration (neglecting sensitivity weighting and sampling density correction) of a single coil's PSF in the x - t and x - f domain showing the 5-fold undersampling artifacts of the conventional (top) and proposed (bottom) k - t sampling scheme. $\delta(\mathbf{x} - \mathbf{x}_0, t - t_0 / f - f_0)$ denotes a unit vector with the non-zero component at the position corresponding to voxel $\mathbf{x}_0 = (x_0, y_0)$ and time/frequency t_0/f_0 . The zoomed area shows the transition between regular (2-fold) and random undersampling. Peak-to-sidelobe ratios of the x - t PSFs are 3.22 (top) and 1.48 (bottom). Corresponding values for the x - f PSFs are 2.92 and 2.02.

of k -space while random undersampling with decreasing density at higher phase encodes is used. Optimization of k -space trajectories combining regular and random undersampling patterns has been proven beneficial to improve reconstruction accuracy [192, 193]. In dynamic imaging, time-interleaved k - t sampling may be used in addition to reduce signal overlaps in the spatio-temporal Fourier x - f domain [194]. Following ideas presented in [192] and [194], a Cartesian k - t sampling scheme for dynamic MRI with time-interleaved regularly and randomly undersampled low- and high-frequency components, respectively, is proposed. Using cardiac short-axis view data, it is demonstrated that this approach improves image reconstruction relative to standard density-weighted CS trajectories.

In ℓ_1 -norm regularized SENSE-based reconstruction, a coil-combined image \mathbf{p} is estimated by minimizing the optimization problem (3.11). For dynamic 2D Cartesian imaging, $\mathbf{E} = (\mathbf{I}_{N_c} \otimes \mathbf{I}_u \mathbf{F}) \mathbf{S}$ is composed of coil sensitivity weighting \mathbf{S} , FT \mathbf{F} along the spatial coordinates, and undersampling of each coil's k - t space using the reduced identity matrix \mathbf{I}_u . The point-spread function (PSF) of a conventional variable-density weighted CS k - t trajectory [79] is shown in Figure 6.7 with noise-like aliasing along the phase encoding and, in x - f space, additionally along the temporal frequency direction (providing sparse-domain incoherence). With the proposed method, the fully sampled center of k - t space is replaced with a regular time-interleaved pattern, while the degree of incoherent random undersampling is increased for higher phase encodes (Figure 6.7). The corresponding PSF in the spatio-temporal x - t domain features well-separated peaks generating coherent aliasing, which is well suited for PI. Upon temporal FT \mathbf{F}_t , the coherent Nyquist replicas are shifted along the temporal frequency direction [194]. Thereby, the x - f PSF replicates the spectral support along the diagonal reducing coherent signal overlap while preserving incoherent interference.

Breath-held fully sampled cine 2D balanced SSFP short-axis view data were acquired (28 coils, FOV: 296 x 264 x 8 mm³, spatial resolution: 2 x 2 x 8 mm³) in a healthy subject on a 3 Tesla scanner (Philips Ingenua, Philips Healthcare, Best, The Netherlands). Data were compressed to 12 virtual channels [188]. Normalized coil sensitivities ($\mathbf{S}^H \mathbf{S} = \mathbf{I}_N$) were computed from a temporal averaged image using ESPIRiT (Section 3.1.3) [65]. k - t space was retrospectively decimated (5- and 8-fold) using time-interleaved regular 2-fold and increasing random variable-density undersampling of low and high spatial frequencies, respectively. Standard random variable-density sampling with a full center of k -space [73, 79] was used for comparison. Image series \mathbf{p} were reconstructed with $\mathbf{\Psi} = \mathbf{F}_t$ using an iterative soft-thresholding algorithm (3.14) leaving the acquired data unchanged ($\tau = 1$). Normalized root-mean-square errors (nRMSE's) were calculated according to: $\|\mathbf{m}_r - \mathbf{m}_o\|_2 / \|\mathbf{m}_o\|_2$ with vectors \mathbf{m}_r and \mathbf{m}_o stacking reconstructed and reference magnitude pixels within a ROI, respectively.

Figure 6.8 shows reconstructed systolic and diastolic magnitude frames together with the corresponding error maps. Figure 6.9 illustrates temporal profile plots across the heart of the fully sampled reference and reconstructions from undersampled data.

Improved unfolding and temporal resolution relative to standard CS sampling is demonstrated. Even though sensitivity information in this study was not obtained frame-by-frame from decimated data, temporally resolved auto-calibration data can be easily derived by averaging of adjacent frames or via low-rank matrix completion [189]. The application to k -space-based

methods, e.g. SPIRiT [23], 3D imaging or further sparsification of the x - f representation [86] is straightforward.

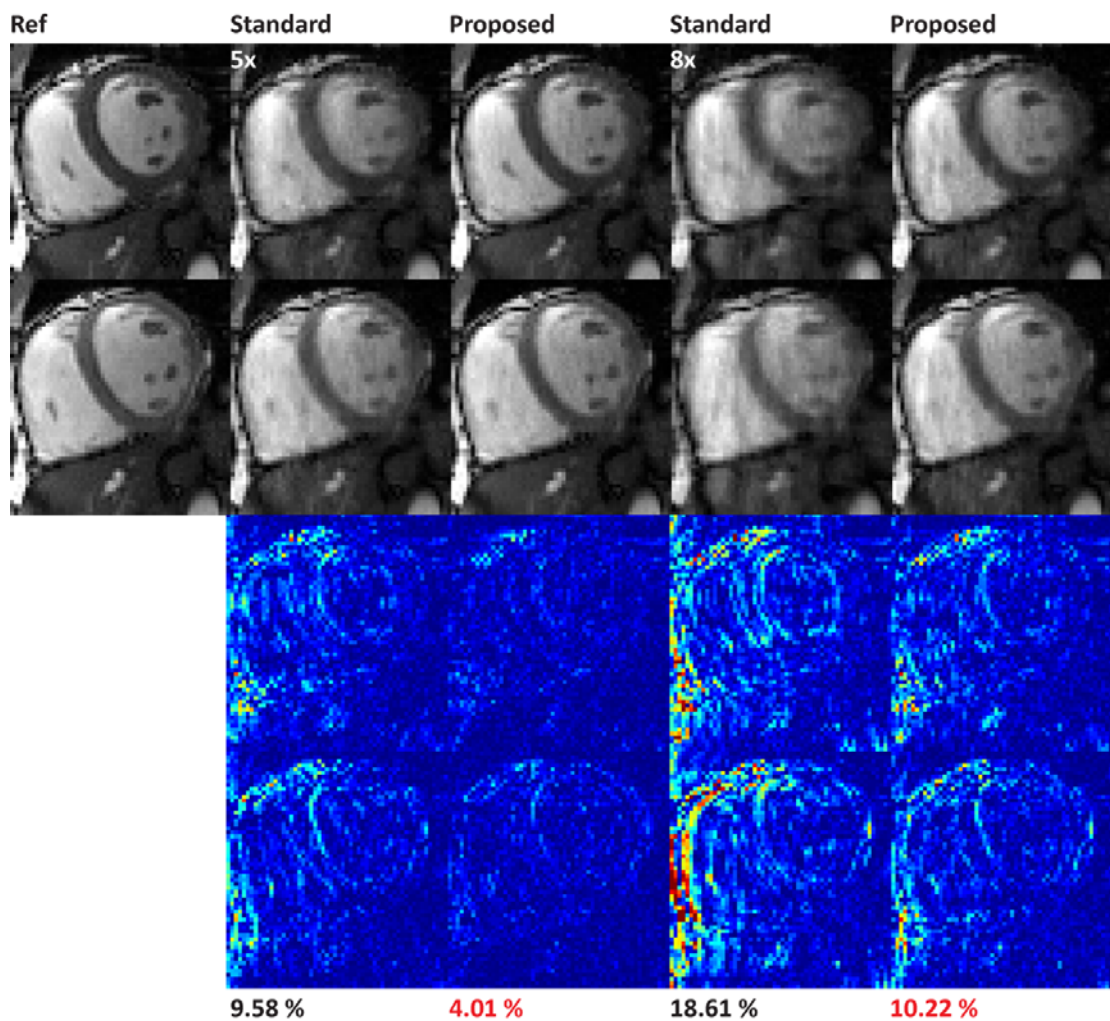


Figure 6.8 Systolic (first row) and diastolic (second row) reference and reconstructed images from 5- and 8-fold undersampled data (left: standard CS sampling, right: proposed sampling). Magnitude error maps depict error reduction due to combination of coherent and incoherent undersampling. Normalized root mean square errors are quoted.

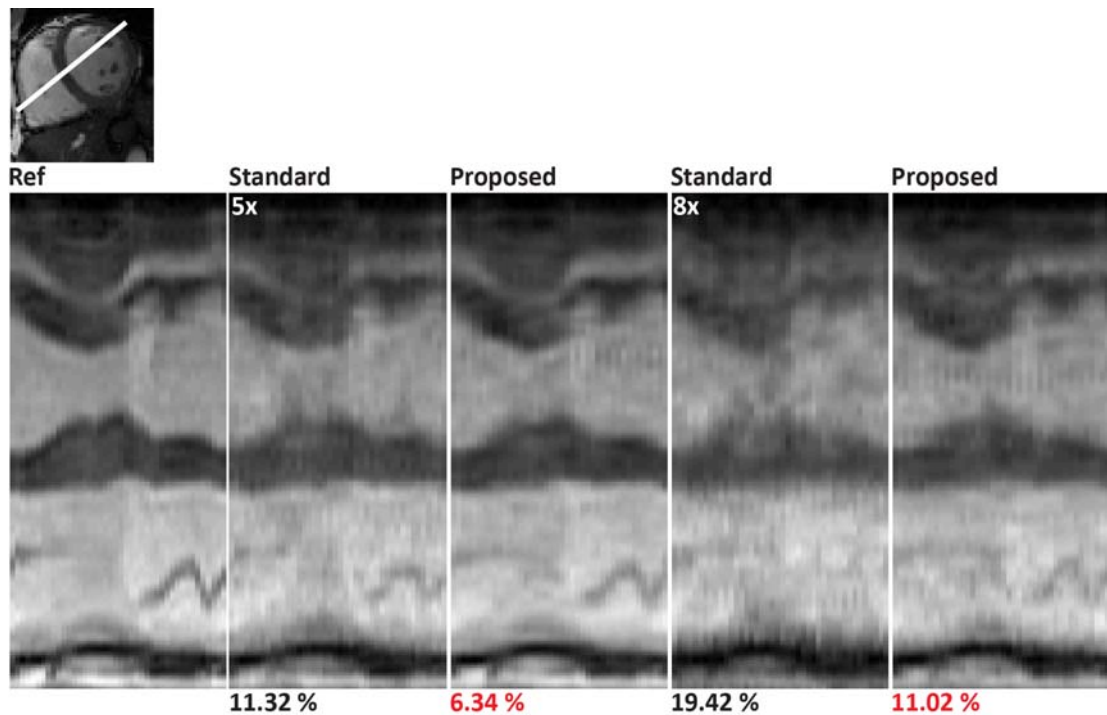


Figure 6.9 Temporal profiles along the indicated line. The proposed sampling scheme shows improved unfolding and temporal resolution compared to standard variable-density CS sampling. $nRMSE$'s of reconstructed profiles are also depicted.

6.4 Discussion

Reduced reconstruction times for non-Cartesian SPIRiT have been demonstrated using a modified PI operator and an approximation of the regridding-gridding cascade, which can be incorporated into any linear SPIRiT-based optimization problem. The extension to 3D and dynamic imaging is straightforward. The inclusion of non-linear regularization is part of future work and first successful attempts have already been made for ℓ_1 -problems [195]. Furthermore, the recently proposed ESPIRiT algorithm [65] is also a computationally optimized variant of SPIRiT, essentially reducing to auto-calibrated SENSE. Thereby, regularization terms act on coil-combined than on multi-coil images. Following this principle, temporally resolved and normalized coil sensitivities for SENSE-like reconstruction can be estimated from the k - t SPIRiT kernel (Chapter 4).

Retrospective data-driven respiratory motion correction has been combined with radial SPIRiT and preliminary results revealed the potential to bring down effective close to nominal scan times in flow encoded MRI. While motion-compensating techniques like averaging might work for 2D

scan protocols [154], future work must focus on the extension of the proposed method to dynamic 3D flow imaging, where 100% scan efficiency is essential. 3D volume imaging is further expected to reduce through-plane motion artifacts. Relative to isotropic 3D projection acquisition, stacked 2D radial trajectories are beneficial in terms of SNR. Relaxing the fixed Golden means (Section 2.2.3) and using modified GA increments [196], respectively, may reduce the noise exposure for the patient and eddy current artifacts due to smaller gradient step sizes. Since in vivo data were measured with prospective cardiac triggering, not the full cardiac cycle was covered. A retrospective cardiac gating PC sequence allowing to reconstruct arbitrarily placed cardiac phases of any temporal width needs to be implemented. Without any restriction on the deformation fields $\mathbf{u}_i(\mathbf{r})$, the i -th motion state's signal model (neglecting coil sensitivity weighting) reads

$$\begin{aligned}
d(\mathbf{k}) &= \int_V \rho(\mathbf{r} + \mathbf{u}_i(\mathbf{r})) e^{-i\mathbf{k} \cdot \mathbf{r}} d\mathbf{r} \\
&= \int_V m(\mathbf{r} + \mathbf{u}_i(\mathbf{r})) e^{i\phi(\mathbf{r} + \mathbf{u}_i(\mathbf{r}))} e^{-i\mathbf{k} \cdot \mathbf{r}} d\mathbf{r} \\
&= \int_V T_i(m) e^{iT_i(\phi)} e^{-i\mathbf{k} \cdot \mathbf{r}} d\mathbf{r} ,
\end{aligned} \tag{6.6}$$

with m and ϕ being the object magnitude and phase, respectively. Following the principle described in Section 3.4.3, both magnitude and phase should be warped prior to FT. If the T_i 's implement linear operations, the discrete encoding model in (3.18) is modified according to

$$\mathbf{d} = \mathbf{E} \text{diag}(e^{i\mathbf{T}\phi}) \mathbf{T}\mathbf{m} + \boldsymbol{\eta} = \mathbf{E}((\mathbf{T}\mathbf{m}) \circ e^{i\mathbf{T}\phi}) + \boldsymbol{\eta} , \tag{6.7}$$

where \circ denotes the element-wise vector multiplication between $\mathbf{T}\mathbf{m}$ and the phase exponential vector $e^{i\mathbf{T}\phi}$. Under which conditions the following approximation holds in flow encoded MRI is another remaining task:

$$\mathbf{T}\boldsymbol{\rho} = \mathbf{T}(\mathbf{m} \circ e^{i\phi}) \approx (\mathbf{T}\mathbf{m}) \circ e^{i\mathbf{T}\phi} . \tag{6.8}$$

Problem (6.7) may also be inverted via a separate magnitude and phase reconstruction framework used in [181] and Chapter 5. However, reconstruction times are then assumed to increase drastically. Restricting the motion model, e.g. to affine motion, the relation (3.17) between a deformed complex-valued object and the corresponding effect in k-space can be used to correct each profile prior to reconstruction. The application of external motion sensors, e.g. field probes for spatio-temporal magnetic field monitoring [197], for motion estimation or cardiac gating is another important part of future research.

An optimized Cartesian k - t sampling scheme for combined PI and CS has been proposed and applied to 2D cardiac short-axis view data. Due to the denser sampling of higher phase encodes,

the proposed acquisition strategy is a candidate to remove the bias of underestimating flow measures when using divergence-free phase regularization in conjunction with the conventional variable-density CS trajectory using a fully sampled center of k-space (Chapter 5). Therefore, the method has to be extended to 3D volume imaging and then tested on 4D flow data.

Chapter 7

Radial 3D *k-t* SPIRiT Multi-Point PC MRI in CHD Patients

7.1 Introduction

In congenital heart disease (CHD) patients, 2D phase-contrast (PC) MRI is considered as a reference method for blood flow measurements of various anatomical conditions [198]. Conventionally, PC MRI data are acquired during free breathing of the subject. To reduce respiratory motion-related image artifacts, a number of signal averages (NSA) is collected. For typical CHD measurements, 2-5 NSAs are acquired resulting in scan times of 2-5 minutes per slice. Depending on the CHD condition, the planning of the slice position and orientation can be very time consuming. In addition, 2D slices may not capture the 3D nature and complexity of pathophysiological blood flow in CHD patients, hence prompting for comprehensive 3D PC MRI imaging approaches.

While conventional PC MRI techniques provide an average velocity vector per image voxel, 3D multi-point PC MRI methods allow assessing velocity distributions within each voxel, and thereby, enable estimating the energy stored in velocity fluctuations [159, 160]. By quantifying both mean kinetic and turbulent kinetic energy (TKE), the energy budget of blood flow can be assessed. In addition, the multi-point encoding concept permits mapping of blood flow over a wide range of velocities without phase wraps [199]. The latter aspect is of particular importance in CHD patients which can present with large variation of flow conditions.

On a practical note, 3D PC MRI methods greatly simplify the planning of the scan, and hence, require less experience of the operator. However, total scan times of 3D PC MRI encoding both mean and turbulent kinetic energy are very long. Different scan acceleration techniques have

been employed to reduce acquisition times including k - t GRAPPA, SENSE, k - t BLAST, k - t PCA [152, 200-202]. Prospective undersampling in conjunction with a k - t PCA variant [154, 155] has been presented in [203].

In this work, the feasibility of 3D k - t SPIRiT multi-point PC MRI is assessed in CHD patients.

7.2 Methods

7.2.1 Data Acquisition

Prospectively undersampled 3D gradient-echo radial cine 10-point 3D PC MRI data with three-directional velocity encoding were acquired from 6 CHD patients (mean age: 6.2 years, range: 9 months – 12.3 years) on a 1.5 Tesla Philips Achieva scanner (Philips Healthcare, Best, The Netherlands). Written informed consent according to ethics guidelines was obtained from the subjects' parents. Golden angle [38] stack of stars trajectories were sampled with a 75% partial-echo factor for readout profiles in the k_x - k_y plane and a half-scan factor of 75% along the k_z phase encoding direction. Sampling patterns between two adjacent heart phases were rotated by a fixed angle increment while projections were congruent along the slice phase encoding direction. Together with the reference data set ($k_v = 0$), three different first gradient moments were sampled per spatial axis. The lowest k_v -value ($\neq 0$) was set according to the maximum expected velocity. The k_v -sampling pattern was the same for each encoded axis. Specific scan parameters

CHD patients characteristics and scan protocols

Patient #	Age	CHD type	Res. [mm ³]	FOV [mm ³]	No. card. phases	V_{enc} [cm/s]	N_c	GA
1	4y/7m	SP sten.	2x2x4	250x250x52	22	400/200/100	2	Yes
2	9m	PV sten.	2x2x2	250x250x20	19	200/100/50	2	Yes
3	2y/4m	LPA sten.	2x2x4	250x250x48	20	180/90/60	2	Yes
4	10y/11m	PA sten.	2x2x4	250x250x52	21	270/135/90	5	Yes
5	-	-	2x2x4	250x250x52	21	240/120/80	5	Yes
6	12y/4m	Dilated branch PAs	2x2x4	250x250x48	21	200/100/50	2	Yes

Table 7.1 *SP: sub-pulmonary, PV: pulmonary valve, LPA: left pulmonary artery, PA: pulmonary artery, V_{enc} : encoding velocity, N_c : number of coils, GA: general anaesthesia.*

for each CHD patient are listed in Table 7.1. The undersampling factor relative to radial Nyquist was set to 8. Respiratory motion artifacts were reduced by a navigator (NAV) placed on the right lung-liver interface. NAV gating efficiency was on the order of 50% using an acceptance windows (3-5 mm) adapting to drifting breathing patterns. The imaging volume was planned to cover the pathological structures.

7.2.2 Image Reconstruction

Each velocity encoded segment was reconstructed using a 3D variant of k - t SPIRiT: prior to reconstruction, congruent stack-of-star profiles were inverse Fourier transformed. Then, for each slice z , dynamic Cartesian k - t space was reconstructed using 2D k - t SPIRiT (Chapter 4). $7 \times 7 \times 3$ k_x - k_y - t kernels were used to assemble the calibration operator \mathbf{G} and were fitted to calibration areas corresponding to $(1/8N \times 1/8N \times \text{no heart phases})$ data arrays of the reference segments ($k_v = 0$), with N being the dimension of the volumes. Depending on the number of k_z phase encodes, number of heart phases and number of channels, reconstruction times were on the order of 2-5 hours on standard computer hardware.

7.2.3 Flow Quantification

From the resulting coil-combined image series $\rho(\mathbf{r}, t, k_v)$, mean velocity $v_m(\mathbf{r}, t)$ and standard deviation $\sigma_v(\mathbf{r}, t)$ were calculated for each velocity encoding direction according to equation (2.32):

$$\frac{\rho(\mathbf{r}, t, k_v)}{\rho(\mathbf{r}, t, 0)} = e^{-0.5\sigma_v(\mathbf{r}, t)^2 k_v^2} e^{-iv_m(\mathbf{r}, t)k_v} . \quad (7.1)$$

Magnitude and velocity induced phase were calculated using a sum-of-squares approach and with a magnitude weighted sum of phase differences [162], respectively. $\sigma_v(\mathbf{r}, t)$ was fitted to $|\rho(\mathbf{r}, t, k_v)| / |\rho(\mathbf{r}, t, 0)|$ for all $k_v \neq 0$ using standard least-squares methods. TKE maps were then computed using

$$TKE(\mathbf{r}, t) = \frac{\nu}{2} \sum_{i=1}^3 \sigma_{v,i}^2(\mathbf{r}, t), \quad (7.2)$$

with i indexing the three orthogonal directions and ν being the fluid density [163]. $v_m(\mathbf{r}, t)$ was obtained by taking the phase of the complex-valued ratio $\rho(\mathbf{r}, t, k_v) / \rho(\mathbf{r}, t, 0)$ for the two k_v 's corresponding to the highest and second highest encoding velocity allowing for three-point PC velocity processing [164].

7.3 Results

Figures 7.1-7.6 show the TKE and velocity magnitude volumes reconstructed with 3D radial k - t SPIRiT. Data sets for each patient show the slices along the k_z -direction. Magnitude image volumes of the reference segments ($k_r = 0$) illustrate the underlying anatomy. Turbulence and flow image series were manually segmented. These masks coincide with regions of interest (ROIs) used for the measurements illustrated in Figure 7.7.

Figure 7.1 shows systolic CHD flow data of a 4.6 year old patient with a hypoplastic LV, a double outlet right ventricle and a severe sub-pulmonary stenosis. Velocities over 300 cm/s occur across the sub-pulmonary structure under GA. The jet is surrounded by high TKE values in the range of 1450 J/m³. The sub-pulmonary narrowing is indicated by the arrow in the magnitude anatomy image.

Systolic TKE and velocity magnitude maps of a 9 months old child are shown in Figure 7.2. The patient was diagnosed with a ventricular imbalance, a dominant RV and a hypoplastic LV together with a mild stenosis at level of pulmonary valve and dilated PAs causing mild narrowing of proximal branch PAs at their origins. The jet formation across the indicated MPA rises up to 230 cm/s under GA comes along with TKE values larger than 400 J/m³.

Systolic CHD TKE and velocity data of a 2.3 year old child with moderate LPA stenosis are presented in Figure 7.3. The focal LPA stenosis at the origin of the bifurcation is highlighted in the TKE image. Higher TKE values are also visible in the ascending aorta adjacent to peak velocities of around 140 cm/s.

Patient data from a ten year old diagnosed with a hypoplastic aortic arch, dilated RV and an Ebstein's anomaly are shown in Figure 7.4. There is a jet across the small pulmonary homograft surrounded by high TKE values. The peak velocity measured within the indicated small homograft is around 260 cm/s while TKE rises up to 900 J/m³.

Systolic TKE formations around high velocity magnitude voxels of patient 5 are presented in Figure 7.5.

Figure 7.6 shows systolic TKE and velocity magnitude data from a 12.3 year old patient with a dilated MPA and branch PAs. Preferential flow toward the RPA is depicted by the arrow in the velocity magnitude image. Relatively high turbulence values are associated with moderate peak velocity magnitudes.

Correlation plots between 3D k - t SPIRiT reconstructed maximum TKE and maximum velocity magnitude together with the correlation between total TKE and maximum velocity magnitude

are illustrated in Figure 7.7. Data points are indexed with the corresponding patient numbers. Patient 1 has the highest peak TKE value, but with a spatially and temporally integrated TKE below numbers of patient 5 and 4. Similarly, patient 5 exhibits largest total TKE, while the peak energy density is below the ones of patient 1 and 4.

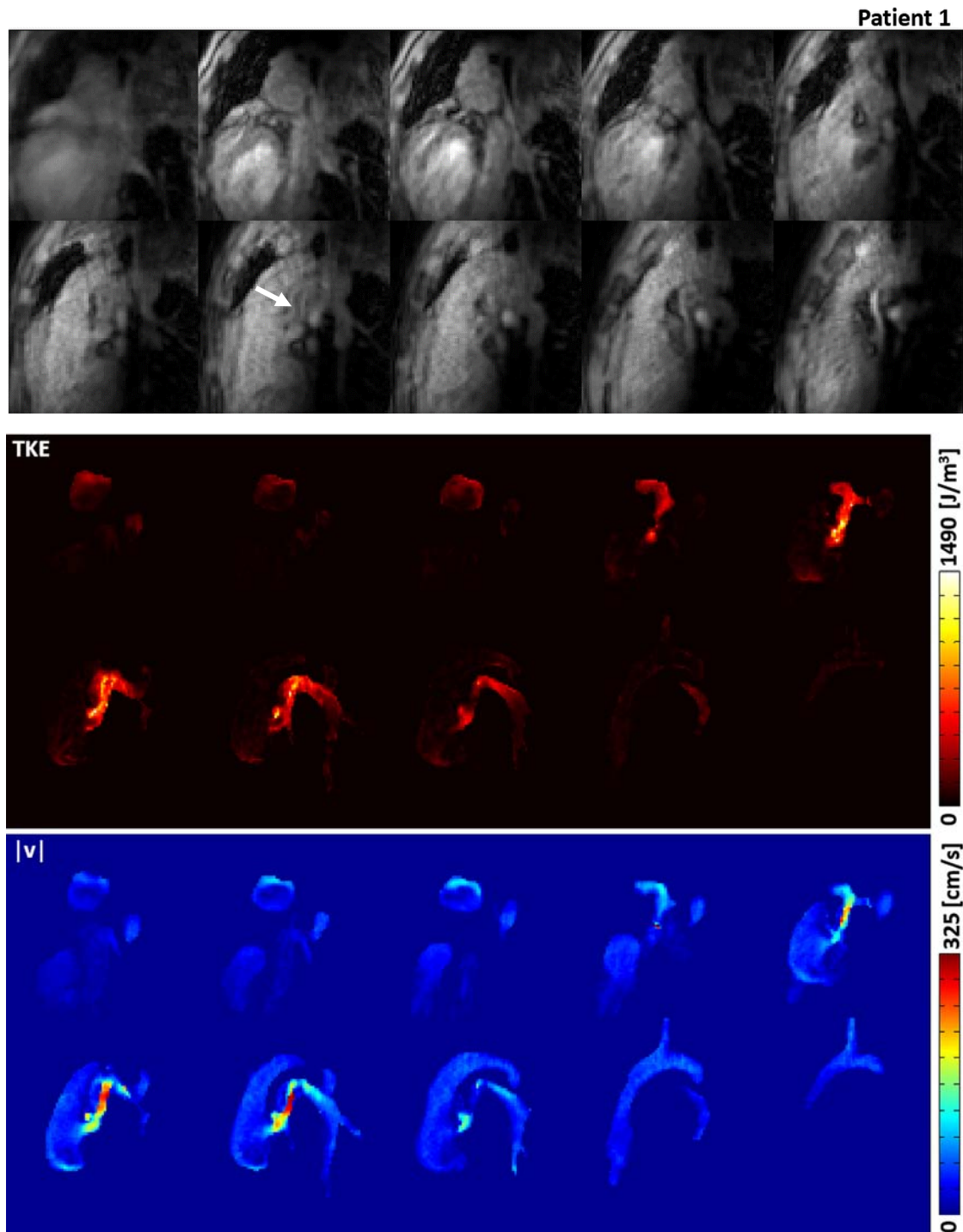


Figure 7.1 Systolic magnitude (top), TKE (middle) and velocity magnitude (bottom) volumes of CHD patient 1.

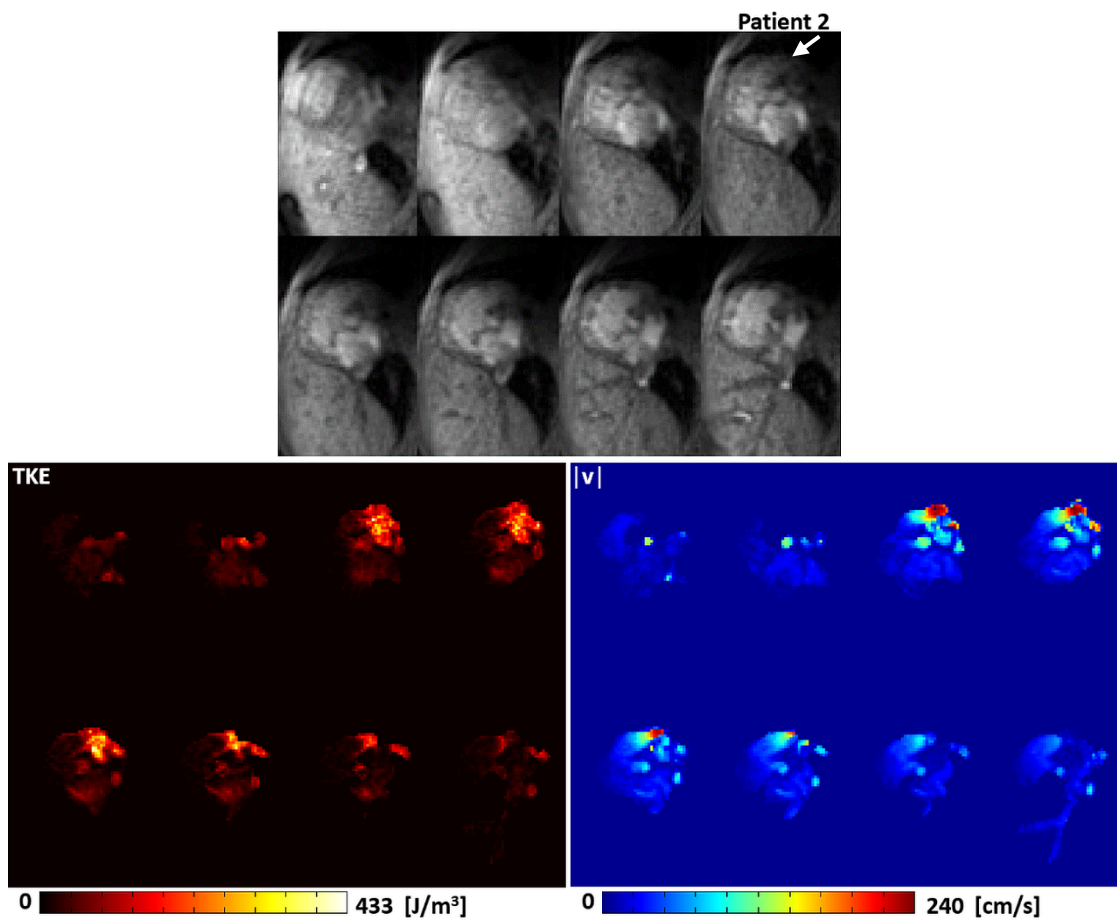


Figure 7.2 Systolic magnitude (top), TKE (bottom left) and velocity magnitude (bottom right) images of CHD patient 2.

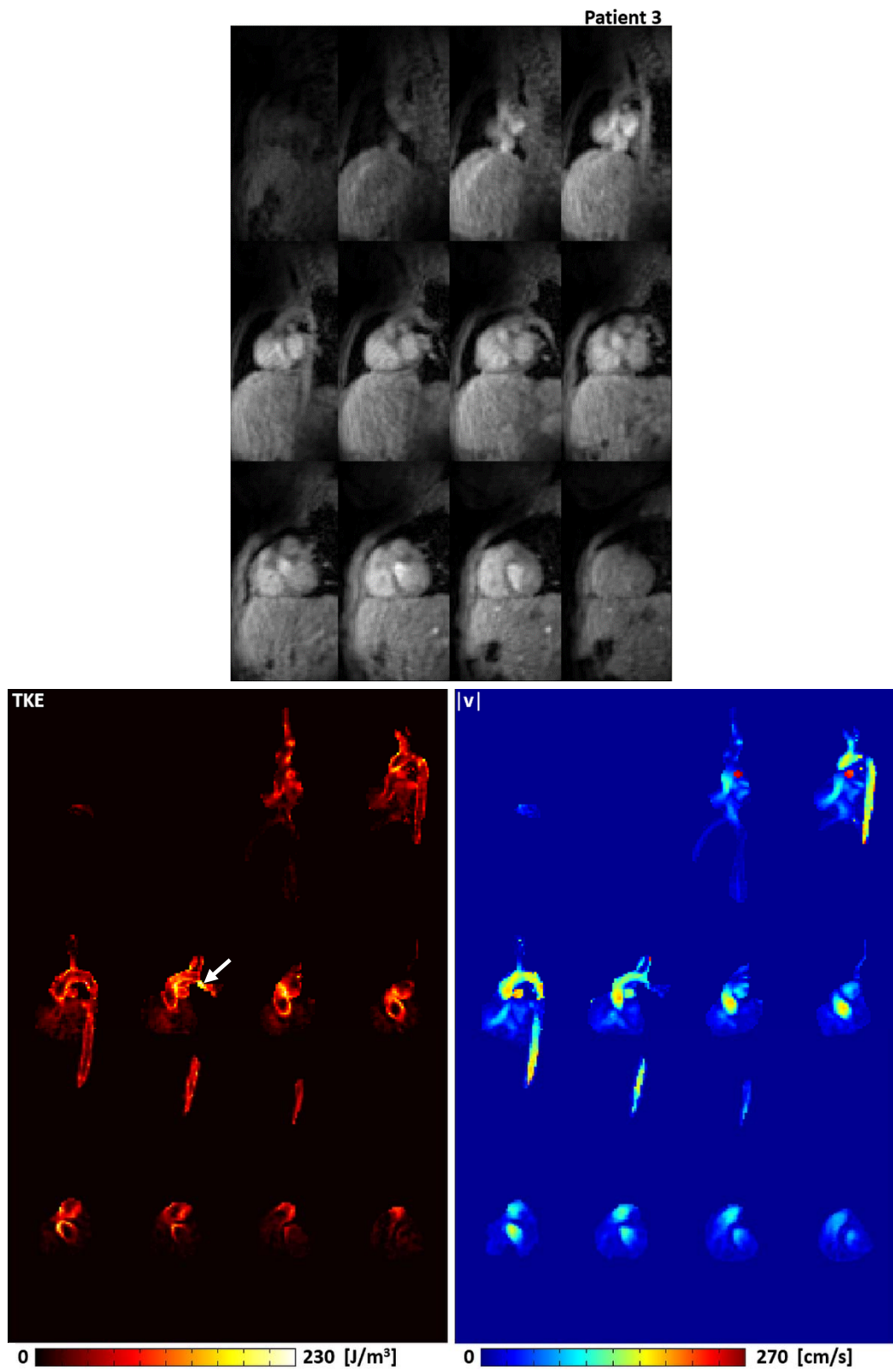


Figure 7.3 Systolic magnitude (top), TKE (bottom left) and velocity magnitude (bottom right) images of CHD patient 3.

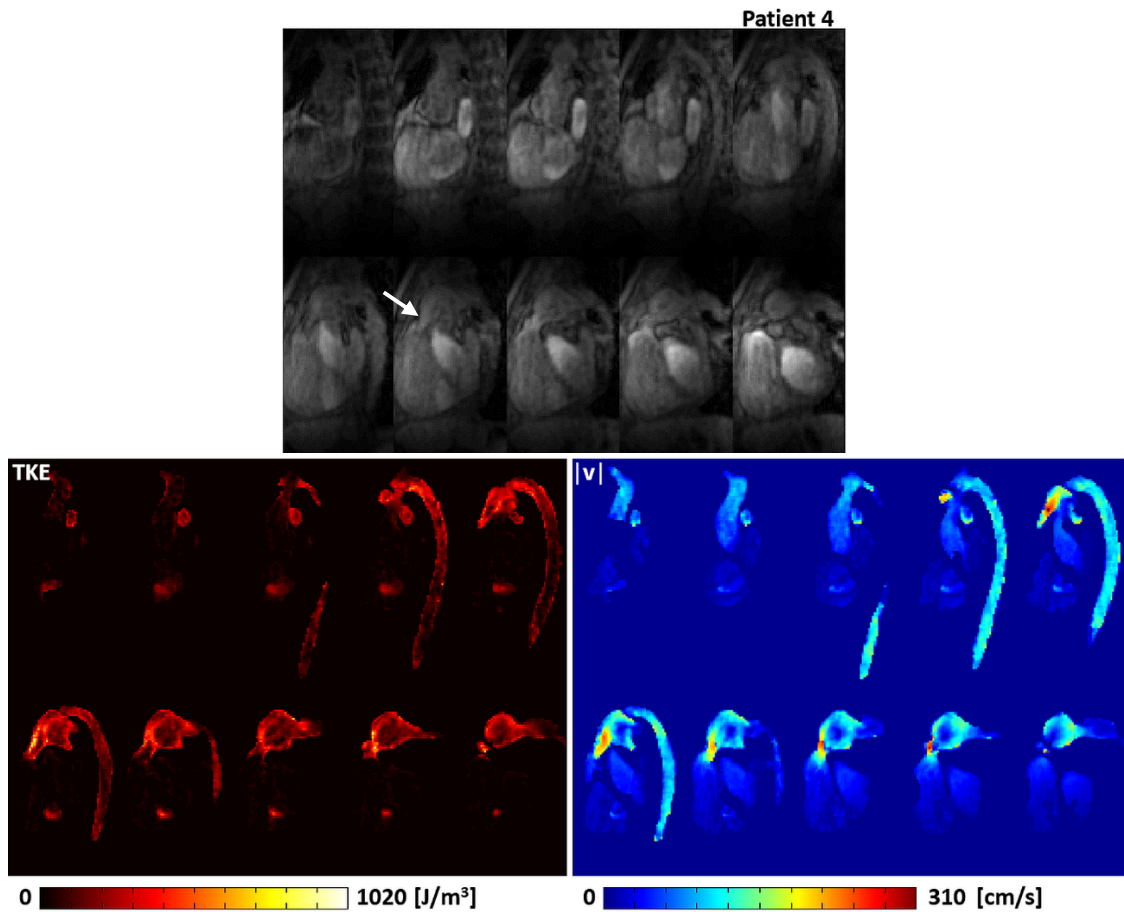


Figure 7.4 *Systolic magnitude (top), TKE (bottom left) and velocity magnitude (bottom right) images of CHD patient 4.*

7.4 Discussion

The feasibility of accelerated 3D multi-point PC MRI in clinical routine use has been demonstrated in this preliminary report. The acceleration factor of 8 yielded nominal scan times of 6-8 minutes resulting in net measurement times of 11-17 minutes depending on the NAV efficiency. Qualitative illustrations revealed TKE formation around jet areas, but turbulence formation was also associated with low velocities in dilated vessel structures. Correlation plots between maximum velocity magnitude and total and maximum TKE showed no strong correlation indicating the potential of TKE quantification to provide additional information besides directional flow measures. However, the data were acquired from six CHD patients with different ages, body sizes and pathologies. Therefore, TKE parameters should be related to these numbers. For instance, normalization with stroke volume should be investigated [204]. Spatial resolutions are

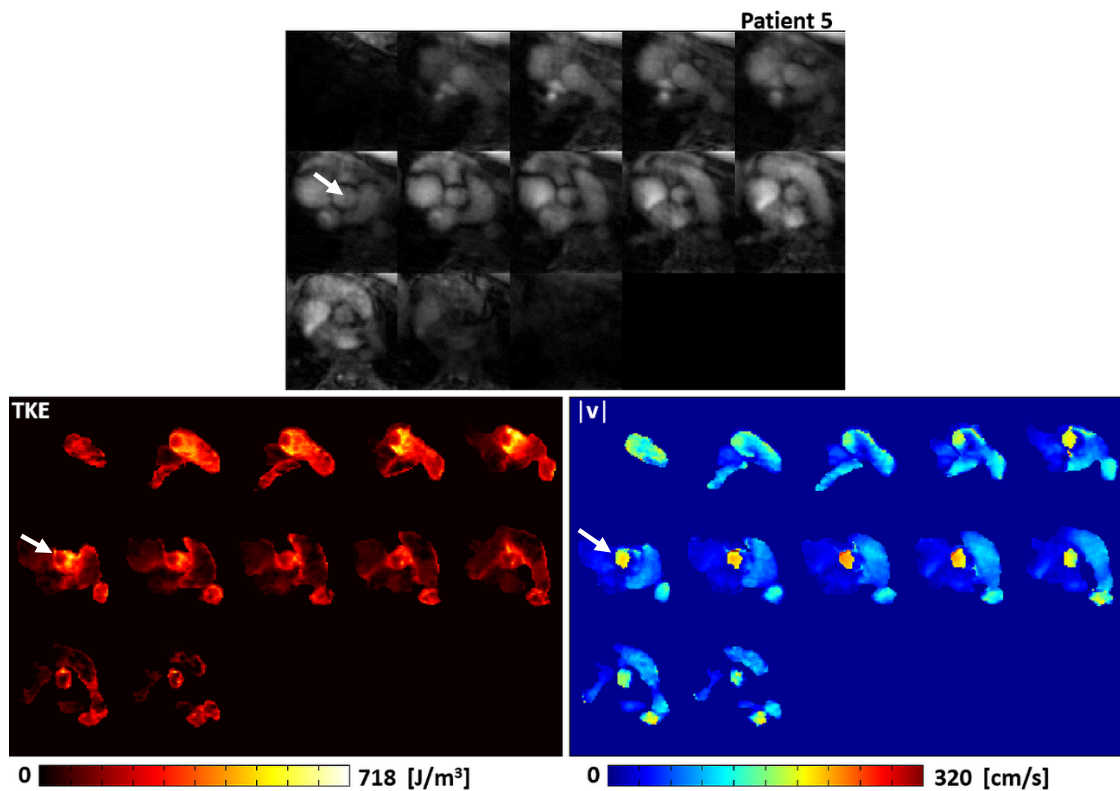


Figure 7.5 Systolic magnitude (top), TKE (bottom left) and velocity magnitude (bottom right) images of CHD patient 5.

relatively low compared to the vessel structures. The signal-to-noise ratio (SNR) decrease with higher resolutions needs to be investigated. Increasing voxel sizes for higher SNR affects the accuracy of standard deviation values and assumption of underlying Gaussian velocity spectra [205]. NAV-gated respiratory motion compensation for anaesthetized subjects resulted in scan efficiencies of around 50%. However, with awake patients, longer net scan times and deeper and stronger varying breathing trajectories need to be considered. Therefore, motion correction and self-gating techniques are required (Sections 3.4 and 6.2). The prospective cardiac triggering scheme used in this study did not cover the full cardiac cycle. Retrospective cardiac triggering is therefore an important concern of future research. Besides variability in constructing heart phases at arbitrary time points, this may bring further insight into energy dissipation effects over the full R-R interval. With large voxels compared to the anatomy sizes, violation of the divergence-free condition becomes another important issue. Divergence-free post-processing [177, 180] or reconstruction (Chapter 5) may be applied. Another limitation of this study is the lack of fully sampled reference data. This was due to the limited amount of research scan time within the patient scan protocols. Standard flow field calculations, for instance peak and total flow measurements, are also part of future work. Additional varying sampling along the slice phase encoding direction in conjunction with non-linear reconstruction methods has the potential to

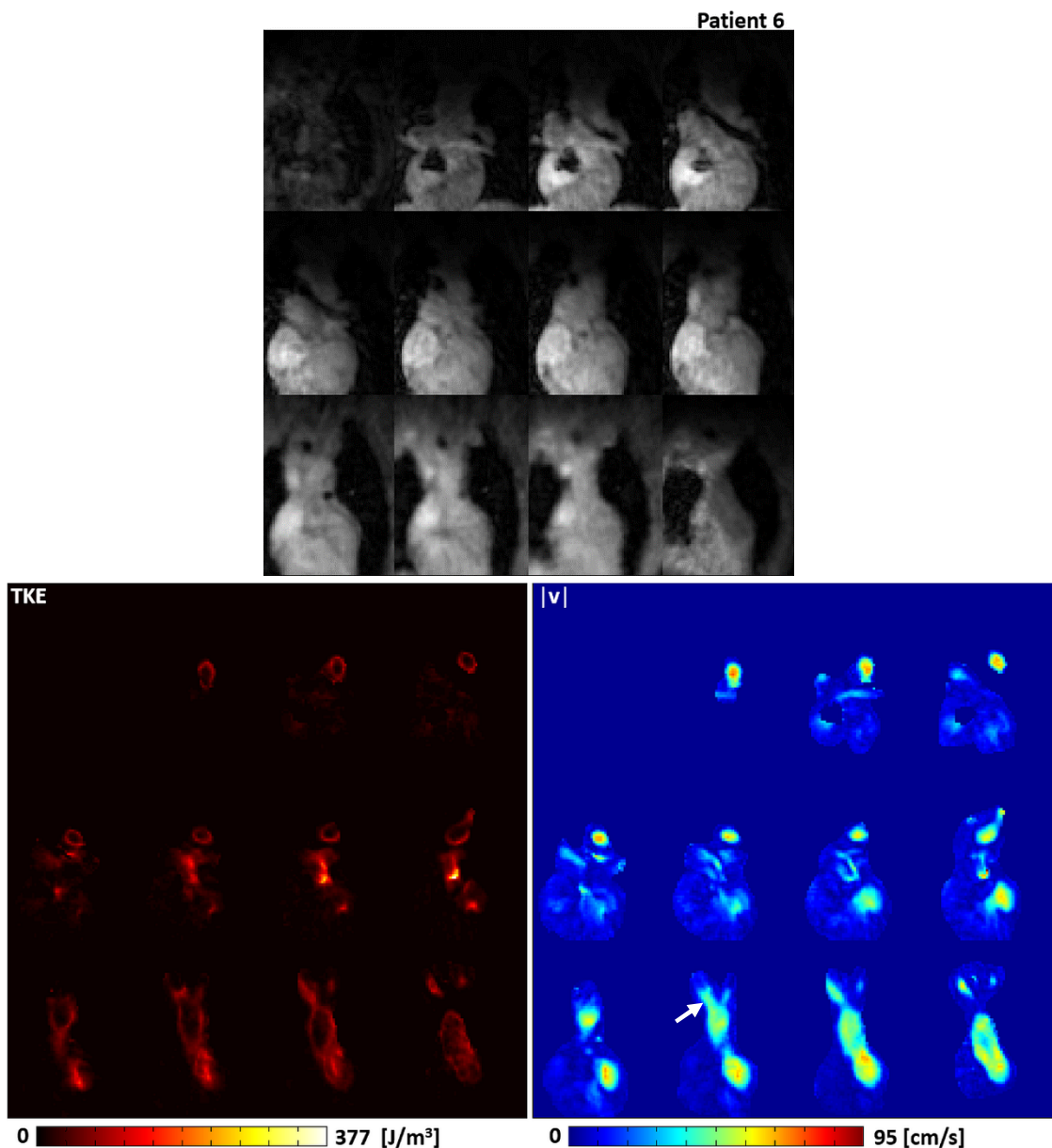


Figure 7.6 Systolic magnitude (top), TKE (bottom left) and velocity magnitude (bottom right) images of CHD patient 6.

further shorten scan times. Only 2- or 5-channel cardiac coils were used in this 1.5 T study. Larger coil arrays or higher field strengths can therefore improve the performance of this auto-calibrated dynamic parallel imaging technique. A major drawback of the presented implementation relates to the very long image reconstruction times when using k - t SPIRiT. Further work is required to provide computationally optimized reconstruction using dedicated computer hardware.

In summary, the potential of radial 3D k - t SPIRiT for highly accelerated CHD measurements in clinical routine use has been demonstrated. At the same time, additional efforts are warranted to address the limited spatial resolution and scan efficiency. Future work should implement

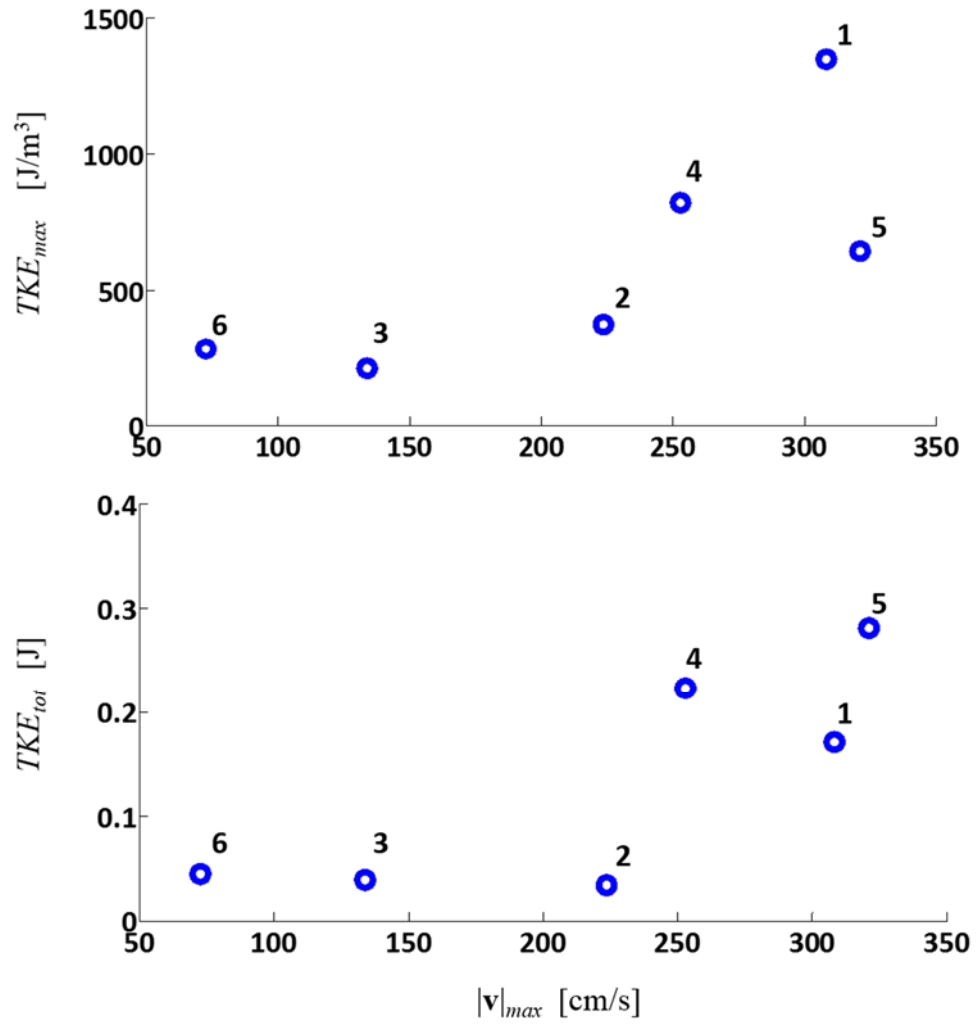


Figure 7.7 Maximum (top) and (total) TKE values are plotted against maximum velocity magnitude. TKE_{tot} was assessed by summation over all voxels within the corresponding dynamic ROIs.

advanced motion compensation techniques as presented in this thesis along with efficient image reconstruction approaches for clinically feasible processing times.

Chapter 8

Discussion and Outlook

Phase-contrast (PC) MRI is a powerful non-invasive imaging tool to quantify and visualize blood flow related physiology and pathophysiology, and thus, has the potential of improving diagnosis and management of Cardiovascular diseases (CVDs). The assessment of multiple velocity encoded images increases the sensitivity to a broader velocity range and allows simultaneous assessment of directional (mean velocity) and incoherent (turbulent) flow. Energy dissipation in the arterial tree due to turbulent flow is associated with complex vascular geometries and the pathogenesis of different CVDs. However, the increased amount of acquired data further aggravates the problem of long measurement times mainly preventing the transfer of the method to clinical routine use. Furthermore, reconstruction accuracy of velocity vector fields is compromised by system imperfections and noise.

A linear auto-calibrated parallel imaging (PI) reconstruction method for dynamic imaging has been proposed, implemented and applied to multi-point PC measurements. Improvements relative to auto-calibrated frame-by-frame and a previously proposed k - t reconstruction have been shown for magnitude and phase reconstruction in the aortic arch. The method does not rely on densely sampled calibration data and can easily be extended to non-linear reconstruction schemes by adding corresponding regularization terms. To further accelerate flow encoded acquisitions, the k - t signal space can be extended with the velocity encoding axis (k - k_v - t space), thereby exploiting spatial-velocity-temporal correlations [206]. However, besides the gain in measurement time and the relaxation of the Gaussian assumption of intra-voxel velocity distributions, reconstruction time and memory load will be further increased. Future work should therefore address these problems and consider efficient implementations on multi-core systems. In this work, computationally optimized iterative reconstruction has also been designed enabling speed-ups by a factor of 1.5-2. The application to k - t reconstructions is straightforward. Instead of multi-coil images, coil-combined dynamic scenes could be calculated using SENSE-like reconstruction where normalized dynamic coil sensitivities are extracted via eigendecomposition of the k - t PI operator following the principles in [65]. A motion correction algorithm has been

developed combining PI and non-rigid motion correction. While similar methods with a 100% acceptance window still use retrospective gating [120] or reconstruction from reduced data is primarily used for motion state image calculations [25], this work has demonstrated the potential of combining scan time reductions from increased gating windows and undersampled data acquisition. Preliminary results show the applicability of the method to PC MRI. However, the detailed effect of using a general linear non-rigid motion operator [128] on non-smooth and motion-corrupted image phase maps needs to be investigated further. Additionally, when using low encoding velocities in multi-point PC schemes, signal magnitude damping due to increased intra-voxel phase dispersion is assumed to complicate data-driven motion information extraction. Non-convex compressed sensing (CS) based reconstruction methods for 3D PC MRI incorporating physical prior knowledge about blood flow have been developed and implemented. Non-divergent field components have been reduced relative to the standard convex method by phase regularization via divergence-free Wavelets or finite difference-based divergence and curl operators. Results from simulated computational fluid dynamics data have revealed decreased directional errors of reconstructed velocity vector fields, and 4D flow in vivo data from the aorta has shown improved streamline statistics. However, the bias of underestimating peak and total flow measures by standard CS has not been removed. This bias is associated with the decreased sampling density with increasing distance from the k-space center. Accordingly, reconstruction of high spatial frequencies progressively relies on spatial gradient-based regularization acting on a coarse resolution relative to the extent of the vessel volume. Therefore, future work should investigate higher spatial resolutions and optimized k-space trajectories with increased sampling density of higher spatial frequencies at the cost of sampling of lower frequency components. A first attempt has been made in this thesis by proposing an optimized k - t sampling pattern for combined PI and CS reconstruction. Improved reconstruction accuracy has been presented for cardiac short-axis data by a separation of coherent and incoherent artifacts via time interleaved regular undersampling of the k-space center with increased random undersampling of higher phase encodes. Using smaller voxel sizes is also expected to better approximate the divergence-free condition and to increase the performance of the discrete velocity operators in smaller vessel structures, respectively.

With the proposed phase regularization approach, divergence has significantly been reduced within the blood pool of the aorta while non-divergent components have been kept at the vessel borders. However, accurate boundary conditions are needed to derive other physical parameters such as wall shear stress. Integrating more comprehensive models inferred from fluid mechanics is thus an essential focus of future work. With increasing complexity of image reconstruction algorithms, the number of regularization and tuning parameters is also increased. Since heuristic

approaches optimizing specific error measures relative to fully sampled data sets are usually used to assign these parameters, automatic allocation schemes for prospectively undersampled data need to be developed.

The feasibility of the developed k - t auto-calibrated PI method for translation into the clinical setting has been demonstrated by applying it to multi-point 4D PC MRI measurements of congenital heart disease patients. A 3D model of the algorithm was used to reconstruct prospective 8-fold radially undersampled data sets. Turbulence and velocity magnitude volumes have been compared and revealed intra-voxel velocity dispersion in jet flow regimes. Assessing 3D volumes instead of single 2D slices clearly simplified scan planning. Since data have been acquired with a small number of coils and has been reconstructed with a linear algorithm, the use of larger coil arrays and non-linear reconstruction schemes are warranted in future work. Furthermore, the assessment and interpretation of patient specific turbulent kinetic energy numbers in terms of energy dissipation over the full cardiac cycle is a remaining issue.

In summary, data-driven reconstruction algorithms for highly accelerated PC MRI have been developed and revealed significant improvements relative to previous techniques. Besides scan time reduction, the methods can also be applied to increase spatio-temporal resolution which is essential to further improve flow quantification (e.g. jet, total and peak flow measurements) and visualization (e.g. stream- and pathlines). Results from computer simulations and retrospectively and prospectively undersampled velocity encoded data have demonstrated the potential of the methods for multi-point PC MRI and further promote the value of flow assessment in clinical routine for diagnosis and monitoring of CVDs.

Bibliography

- [1] S. Mendis, P. Puska, and B. Norrving, "Global Atlas on Cardiovascular Disease Prevention and Control," *Published by the World Health Organization in Collaboration with the World Heart Federation and the World Stroke Organization*, 2011.
- [2] C. Cheng, D. Tempel, R. van Haperen, A. van der Baan, F. Grosveld, M. J. Daemen, *et al.*, "Atherosclerotic lesion size and vulnerability are determined by patterns of fluid shear stress," *Circulation*, vol. 113, pp. 2744-53, 2006.
- [3] P. F. Davies, "Hemodynamic shear stress and the endothelium in cardiovascular pathophysiology," *Nat Clin Pract Cardiovasc Med*, vol. 6, pp. 16-26, 2009.
- [4] M. Markl, A. Frydrychowicz, S. Kozerke, M. Hope, and O. Wieben, "4D flow MRI," *J Magn Reson Imaging*, vol. 36, pp. 1015-36, 2012.
- [5] M. D. Hope, T. A. Hope, A. K. Meadows, K. G. Ordovas, T. H. Urbania, M. T. Alley, *et al.*, "Bicuspid aortic valve: four-dimensional MR evaluation of ascending aortic systolic flow patterns," *Radiology*, vol. 255, pp. 53-61, 2010.
- [6] P. P. Sengupta, G. Pedrizzetti, P. J. Kilner, A. Kheradvar, T. Ebbers, G. Tonti, *et al.*, "Emerging trends in CV flow visualization," *JACC Cardiovasc Imaging*, vol. 5, pp. 305-16, 2012.
- [7] S. D. Shpilfoygel, R. A. Close, D. J. Valentino, and G. R. Duckwiler, "X-ray videodensitometric methods for blood flow and velocity measurement: a critical review of literature," *Med Phys*, vol. 27, pp. 2008-23, 2000.
- [8] P. R. Moran, "A flow velocity zeugmatographic interlace for NMR imaging in humans," *Magn Reson Imaging*, vol. 1, pp. 197-203, 1982.
- [9] P. Thunberg, M. Karlsson, and L. Wigstrom, "Accuracy and reproducibility in phase contrast imaging using SENSE," *Magn Reson Med*, vol. 50, pp. 1061-8, 2003.
- [10] C. Baltés, S. Kozerke, M. S. Hansen, K. P. Pruessmann, J. Tsao, and P. Boesiger, "Accelerating cine phase-contrast flow measurements using k-t BLAST and k-t SENSE," *Magn Reson Med*, vol. 54, pp. 1430-8, 2005.
- [11] D. Kim, H. A. Dyvorne, R. Otazo, L. Feng, D. K. Sodickson, and V. S. Lee, "Accelerated phase-contrast cine MRI using k-t SPARSE-SENSE," *Magn Reson Med*, vol. 67, pp. 1054-64, 2012.
- [12] P. Dyverfeldt, A. Sigfridsson, J. P. Kvitting, and T. Ebbers, "Quantification of intravoxel velocity standard deviation and turbulence intensity by generalizing phase-contrast MRI," *Magn Reson Med*, vol. 56, pp. 850-8, 2006.
- [13] F. Bloch, "Nuclear Induction," *Physical Review*, vol. 70, pp. 460-474, 1946.
- [14] P. C. Lauterbur, "Image Formation by Induced Local Interactions - Examples Employing Nuclear Magnetic-Resonance," *Nature*, vol. 242, pp. 190-191, 1973.
- [15] R. R. Ernst, *Principles of Nuclear Magnetic Resonance in One and Two Dimensions*: Oxford University Press, 1987.
- [16] E. M. Haacke, R. W. Brown, M. R. Thompson, and R. Venkatesan, *Magnetic Resonance Imaging: Physical Principles and Sequence Design*, 1st ed.: Wiley-Liss, 1999.
- [17] M. A. Bernstein, F. K. King, and X. J. Zhou, *Handbook of MRI Pulse Sequences*: Elsevier Academic Press, 2004.
- [18] J. A. Fessler, "Model-Based Image Reconstruction for MRI," *IEEE Signal Processing Magazine*, vol. 27, pp. 81-89, 2010.
- [19] P. C. Lauterbur, D. N. Levin, and R. B. Marr, "Theory and Simulation of NMR Spectroscopic Imaging and Field Plotting by Projection Reconstruction Involving an Intrinsic Frequency Dimension," *Journal of Magnetic Resonance*, vol. 59, pp. 536-541, 1984.

- [20] H. T. C. Nielsen, G. E. Gold, E. W. Olcott, J. M. Pauly, and D. G. Nishimura, "Ultra-short echo-time 2D time-of-flight MR angiography using a half-pulse excitation," *Magnetic Resonance in Medicine*, vol. 41, pp. 591-599, 1999.
- [21] M. S. Hansen, C. Baltes, J. Tsao, S. Kozerke, K. P. Pruessmann, and H. Eggers, "k-t BLAST reconstruction from non-Cartesian k-t space sampling," *Magn Reson Med*, vol. 55, pp. 85-91, 2006.
- [22] F. Huang, S. Vijayakumar, Y. Li, S. Hertel, S. Reza, and G. R. Duensing, "Self-calibration method for radial GRAPPA/k-t GRAPPA," *Magn Reson Med*, vol. 57, pp. 1075-85, 2007.
- [23] M. Lustig and J. M. Pauly, "SPIRiT: Iterative self-consistent parallel imaging reconstruction from arbitrary k-space," *Magn Reson Med*, vol. 64, pp. 457-71, 2010.
- [24] M. S. Hansen, T. S. Sorensen, A. E. Arai, and P. Kellman, "Retrospective reconstruction of high temporal resolution cine images from real-time MRI using iterative motion correction," *Magn Reson Med*, vol. 68, pp. 741-50, 2012.
- [25] M. Usman, D. Atkinson, F. Odille, C. Kolbitsch, G. Vaillant, T. Schaeffter, *et al.*, "Motion corrected compressed sensing for free-breathing dynamic cardiac MRI," *Magn Reson Med*, vol. 70, pp. 504-16, 2013.
- [26] G. H. Glover and J. M. Pauly, "Projection reconstruction techniques for reduction of motion effects in MRI," *Magn Reson Med*, vol. 28, pp. 275-89, 1992.
- [27] A. C. Larson, R. D. White, G. Laub, E. R. McVeigh, D. Li, and O. P. Simonetti, "Self-gated cardiac cine MRI," *Magn Reson Med*, vol. 51, pp. 93-102, 2004.
- [28] Z. P. Liang and P. C. Lauterbur, *Principles of Magnetic Resonance Imaging: A Signal Processing Perspective*: IEEE Press, 2000.
- [29] J. D. O'Sullivan, "A fast sinc function gridding algorithm for fourier inversion in computer tomography," *IEEE Trans Med Imaging*, vol. 4, pp. 200-7, 1985.
- [30] J. I. Jackson, C. H. Meyer, D. G. Nishimura, and A. Macovski, "Selection of a convolution function for Fourier inversion using gridding [computerised tomography application]," *IEEE Trans Med Imaging*, vol. 10, pp. 473-8, 1991.
- [31] H. Schomberg and J. Timmer, "The gridding method for image reconstruction by Fourier transformation," *IEEE Trans Med Imaging*, vol. 14, pp. 596-607, 1995.
- [32] V. Rasche, R. Proksa, R. Sinkus, P. Bornert, and H. Eggers, "Resampling of data between arbitrary grids using convolution interpolation," *IEEE Transactions on Medical Imaging*, vol. 18, pp. 385-392, 1999.
- [33] J. I. Jackson, C. H. Meyer, D. G. Nishimura, and A. Macovski, "Selection of a Convolution Function for Fourier Inversion Using Gridding," *IEEE Transactions on Medical Imaging*, vol. 10, pp. 473-478, 1991.
- [34] P. J. Beatty, D. G. Nishimura, and J. M. Pauly, "Rapid gridding reconstruction with a minimal oversampling ratio," *IEEE Transactions on Medical Imaging*, vol. 24, pp. 799-808, 2005.
- [35] J. A. Fessler and B. P. Sutton, "Nonuniform fast Fourier transforms using min-max interpolation," *IEEE Transactions on Signal Processing*, vol. 51, pp. 560-574, 2003.
- [36] P. G. Anderson, "Multidimensional Golden Means," *Applications of Fibonacci Numbers, Vol 5*, pp. 1-9, 1993.
- [37] R. W. Chan, E. A. Ramsay, C. H. Cunningham, and D. B. Plewes, "Temporal stability of adaptive 3D radial MRI using multidimensional golden means," *Magn Reson Med*, vol. 61, pp. 354-63, 2009.
- [38] S. Winkelmann, T. Schaeffter, T. Koehler, H. Eggers, and O. Doessel, "An optimal radial profile order based on the Golden Ratio for time-resolved MRI," *IEEE Trans Med Imaging*, vol. 26, pp. 68-76, 2007.
- [39] D. B. Twieg, J. Katz, and R. M. Peshock, "A general treatment of NMR imaging with chemical shifts and motion," *Magn Reson Med*, vol. 5, pp. 32-46, 1987.
- [40] M. A. Bernstein, A. Shimakawa, and N. J. Pelc, "Minimizing T_e in Moment-Nullled or Flow-Encoded 2-Dimensional and 3-Dimensional Gradient-Echo Imaging," *JMRI-Journal of Magnetic Resonance Imaging*, vol. 2, pp. 583-588, 1992.

- [41] J. L. Prince, "Convolution backprojection formulas for 3-D vector tomography with application to MRI," *IEEE Transactions on Image Processing*, vol. 5, pp. 1462-1472, 1996.
- [42] N. J. Pelc, M. A. Bernstein, A. Shimakawa, and G. H. Glover, "Encoding strategies for three-direction phase-contrast MR imaging of flow," *J Magn Reson Imaging*, vol. 1, pp. 405-13, 1991.
- [43] T. E. Conturo and G. D. Smith, "Signal-to-Noise in Phase-Angle Reconstruction - Dynamic-Range Extension Using Phase Reference Offsets," *Magnetic Resonance in Medicine*, vol. 15, pp. 420-437, 1990.
- [44] A. Macovski, "Noise in MRI," *Magnetic Resonance in Medicine*, vol. 36, pp. 494-497, 1996.
- [45] C. M. Tsai and D. G. Nishimura, "Reduced aliasing artifacts using variable-density k-space sampling trajectories," *Magnetic Resonance in Medicine*, vol. 43, pp. 452-458, 2000.
- [46] M. Markl, R. Bammer, M. T. Alley, C. J. Elkins, M. T. Draney, A. Barnett, *et al.*, "Generalized reconstruction of phase contrast MRI: analysis and correction of the effect of gradient field distortions," *Magn Reson Med*, vol. 50, pp. 791-801, 2003.
- [47] M. A. Bernstein, X. J. Zhou, J. A. Polzin, K. F. King, A. Ganin, N. J. Pelc, *et al.*, "Concomitant gradient terms in phase contrast MR: analysis and correction," *Magn Reson Med*, vol. 39, pp. 300-8, 1998.
- [48] P. Mansfield and B. Chapman, "Active Magnetic Screening of Coils for Static and Time-Dependent Magnetic-Field Generation in NMR Imaging," *Journal of Physics E-Scientific Instruments*, vol. 19, pp. 540-545, 1986.
- [49] P. Jehenson, M. Westphal, and N. Schuff, "Analytical Method for the Compensation of Eddy-Current Effects Induced by Pulsed Magnetic-Field Gradients in NMR Systems," *Journal of Magnetic Resonance*, vol. 90, pp. 264-278, 1990.
- [50] P. G. Walker, G. B. Cranney, M. B. Scheidegger, G. Waseleski, G. M. Pohost, and A. P. Yoganathan, "Semiautomated Method for Noise-Reduction and Background Phase Error Correction in MR Phase-Velocity Data," *JMRI-Journal of Magnetic Resonance Imaging*, vol. 3, pp. 521-530, 1993.
- [51] J. W. Lankhaar, M. B. M. Hofman, J. T. Marcus, J. J. M. Zwanenburg, T. J. C. Faes, and A. Vonk-Noordegraaf, "Correction of phase offset errors in main pulmonary artery flow quantification," *Journal of Magnetic Resonance Imaging*, vol. 22, pp. 73-79, 2005.
- [52] A. Chernobelsky, O. Shubayev, C. R. Comeau, and S. D. Wolff, "Baseline correction of phase contrast images improves quantification of blood flow in the great vessels," *Journal of Cardiovascular Magnetic Resonance*, vol. 9, pp. 681-685, 2007.
- [53] D. Giese, M. Haerberlin, C. Barmet, K. P. Pruessmann, T. Schaeffter, and S. Kozerke, "Analysis and correction of background velocity offsets in phase-contrast flow measurements using magnetic field monitoring," *Magnetic Resonance in Medicine*, vol. 67, pp. 1294-1302, 2012.
- [54] S. J. Vannesjo, M. Haerberlin, L. Kasper, M. Pavan, B. J. Wilm, C. Barmet, *et al.*, "Gradient system characterization by impulse response measurements with a dynamic field camera," *Magnetic Resonance in Medicine*, vol. 69, pp. 583-593, 2013.
- [55] A. Cardenas-Blanco, C. Tejos, P. Irarrazaval, and I. Cameron, "Noise in Magnitude Magnetic Resonance Images," *Concepts in Magnetic Resonance Part A*, vol. 32A, pp. 409-416, 2008.
- [56] K. P. Pruessmann, M. Weiger, M. B. Scheidegger, and P. Boesiger, "SENSE: sensitivity encoding for fast MRI," *Magn Reson Med*, vol. 42, pp. 952-62, 1999.
- [57] A. Ribes and F. Schmitt, "Linear inverse problems in imaging," *IEEE Signal Processing Magazine*, vol. 25, pp. 84-99, 2008.
- [58] H. V. Henderson and S. R. Searle, "On Deriving the Inverse of a Sum of Matrices," *SIAM Review*, vol. 23, pp. 53-60, 1981.
- [59] K. P. Pruessmann, M. Weiger, P. Bornert, and P. Boesiger, "Advances in sensitivity encoding with arbitrary k-space trajectories," *Magn Reson Med*, vol. 46, pp. 638-51, 2001.

- [60] J. W. Goldfarb, "The SENSE ghost: field-of-view restrictions for SENSE imaging," *J Magn Reson Imaging*, vol. 20, pp. 1046-51, 2004.
- [61] M. A. Griswold, S. Kannengiesser, R. M. Heidemann, J. Wang, and P. M. Jakob, "Field-of-view limitations in parallel imaging," *Magn Reson Med*, vol. 52, pp. 1118-26, 2004.
- [62] M. Blaimer, F. Breuer, M. Mueller, R. M. Heidemann, M. A. Griswold, and P. M. Jakob, "SMASH, SENSE, PILS, GRAPPA: how to choose the optimal method," *Top Magn Reson Imaging*, vol. 15, pp. 223-36, 2004.
- [63] M. A. Griswold, P. M. Jakob, R. M. Heidemann, M. Nittka, V. Jellus, J. Wang, *et al.*, "Generalized autocalibrating partially parallel acquisitions (GRAPPA)," *Magn Reson Med*, vol. 47, pp. 1202-10, 2002.
- [64] P. B. Roemer, W. A. Edelstein, C. E. Hayes, S. P. Souza, and O. M. Mueller, "The NMR Phased-Array," *Magnetic Resonance in Medicine*, vol. 16, pp. 192-225, 1990.
- [65] M. Uecker, P. Lai, M. J. Murphy, P. Virtue, M. Elad, J. M. Pauly, *et al.*, "ESPIRiT-an eigenvalue approach to autocalibrating parallel MRI: Where SENSE meets GRAPPA," *Magn Reson Med*, vol. 71, pp. 990-1001, 2014.
- [66] M. A. Griswold, M. Blaimer, R. M. Heidemann, P. Speier, S. Kannengiesser, M. Nittka, *et al.*, "Rapid Evaluation of Cardiac Function Using Undersampled Radial TrueFISP with GRAPPA," *Proceedings of the 12th Annual Meeting of ISMRM*, Kyoto, Japan, 2004.
- [67] N. Seiberlich, F. A. Breuer, M. Blaimer, K. Barkauskas, P. M. Jakob, and M. A. Griswold, "Non-Cartesian data reconstruction using GRAPPA operator gridding (GROG)," *Magnetic Resonance in Medicine*, vol. 58, pp. 1257-1265, 2007.
- [68] R. M. Heidemann, M. A. Griswold, N. Seiberlich, G. Kruger, S. A. R. Kannengiesser, B. Kiefer, *et al.*, "Direct parallel image reconstructions for spiral trajectories using GRAPPA," *Magnetic Resonance in Medicine*, vol. 56, pp. 317-326, 2006.
- [69] P. Lai, M. Lustig, A. C. Brau, S. Vasanawala, P. J. Beatty, and M. Alley, "Efficient L1SPIRiT Reconstruction (ESPIRiT) for Highly Accelerated 3D Volumetric MRI with Parallel Imaging and Compressed Sensing," *Proceedings of the 18th Annual Meeting of ISMRM*, Stockholm, Sweden, 2010.
- [70] A. M. Bruckstein, D. L. Donoho, and M. Elad, "From Sparse Solutions of Systems of Equations to Sparse Modeling of Signals and Images," *SIAM Review*, vol. 51, pp. 34-81, 2009.
- [71] D. L. Donoho, "Compressed sensing," *IEEE Transactions on Information Theory*, vol. 52, pp. 1289-1306, 2006.
- [72] E. J. Candes, J. Romberg, and T. Tao, "Robust uncertainty principles: Exact signal reconstruction from highly incomplete frequency information," *IEEE Transactions on Information Theory*, vol. 52, pp. 489-509, 2006.
- [73] M. Lustig, D. Donoho, and J. M. Pauly, "Sparse MRI: The application of compressed sensing for rapid MR imaging," *Magn Reson Med*, vol. 58, pp. 1182-95, 2007.
- [74] S. Ramani and J. A. Fessler, "An Accelerated Iterative Reweighted Least Squares Algorithm for Compressed Sensing MRI," *IEEE International Symposium on Biomedical Imaging: From Nano to Macro*, pp. 257-260, 2010.
- [75] M. A. T. Figueiredo and R. D. Nowak, "An EM algorithm for wavelet-based image restoration," *IEEE Transactions on Image Processing*, vol. 12, pp. 906-916, 2003.
- [76] I. Daubechies, M. Defrise, and C. De Mol, "An iterative thresholding algorithm for linear inverse problems with a sparsity constraint," *Communications on Pure and Applied Mathematics*, vol. 57, pp. 1413-1457, 2004.
- [77] A. Beck and M. Teboulle, "A Fast Iterative Shrinkage-Thresholding Algorithm for Linear Inverse Problems," *SIAM Journal on Imaging Sciences*, vol. 2, pp. 183-202, 2009.
- [78] M. Lustig, J. M. Santos, D. L. Donoho, and J. M. Pauly, "k-t SPARSE: High frame rate dynamic MRI exploiting spatio-temporal sparsity," *Proceedings of the 14th Annual Meeting of ISMRM*, Seattle, USA, 2006.

- [79] R. Otazo, D. Kim, L. Axel, and D. K. Sodickson, "Combination of Compressed Sensing and Parallel Imaging for Highly Accelerated First-Pass Cardiac Perfusion MRI," *Magnetic Resonance in Medicine*, vol. 64, pp. 767-776, 2010.
- [80] K. Dabov, A. Foi, V. Katkovnik, and K. Egiazarian, "Image denoising by sparse 3-D transform-domain collaborative filtering," *IEEE Transactions on Image Processing*, vol. 16, pp. 2080-2095, 2007.
- [81] M. Akcakaya, T. A. Basha, B. Goddu, L. A. Goepfert, K. V. Kissinger, V. Tarokh, *et al.*, "Low-dimensional-structure self-learning and thresholding: regularization beyond compressed sensing for MRI reconstruction," *Magn Reson Med*, vol. 66, pp. 756-67, 2011.
- [82] M. Akcakaya, S. Nam, P. Hu, M. H. Moghari, L. H. Ngo, V. Tarokh, *et al.*, "Compressed Sensing With Wavelet Domain Dependencies for Coronary MRI: A Retrospective Study," *IEEE Transactions on Medical Imaging*, vol. 30, pp. 1090-1099, 2011.
- [83] S. Ravishankar and Y. Bresler, "MR image reconstruction from highly undersampled k-space data by dictionary learning," *IEEE Trans Med Imaging*, vol. 30, pp. 1028-41, 2011.
- [84] J. Tsao, P. Boesiger, and K. P. Pruessmann, "k-t BLAST and k-t SENSE: dynamic MRI with high frame rate exploiting spatiotemporal correlations," *Magn Reson Med*, vol. 50, pp. 1031-42, 2003.
- [85] F. Huang, J. Akao, S. Vijayakumar, G. R. Duensing, and M. Limkeman, "k-t GRAPPA: a k-space implementation for dynamic MRI with high reduction factor," *Magn Reson Med*, vol. 54, pp. 1172-84, 2005.
- [86] H. Pedersen, S. Kozerke, S. Ringgaard, K. Nehrke, and W. Y. Kim, "k-t PCA: temporally constrained k-t BLAST reconstruction using principal component analysis," *Magn Reson Med*, vol. 62, pp. 706-16, 2009.
- [87] G. Adluru, R. T. Whitaker, and E. V. R. DiBella, "Spatio-temporal constrained reconstruction of sparse dynamic contrast enhanced radial MRI data," *IEEE International Symposium on Biomedical Imaging : Macro to Nano, Vols 1-3*, pp. 109-112, 2007.
- [88] J. V. Velikina, K. M. Johnson, W. F. Block, and A. A. Samsonov, "Design of Temporally Constrained Compressed Sensing Methods for Accelerated Dynamic MRI," *Proceedings of the 18th Annual Meeting of ISMRM*, Stockholm, Sweden, 2010.
- [89] L. Feng, R. Otazo, H. Jung, J. H. Jensen, J. C. Ye, D. K. Sodickson, *et al.*, "Accelerated cardiac T2 mapping using breath-hold multiecho fast spin-echo pulse sequence with k-t FOCUSS," *Magn Reson Med*, vol. 65, pp. 1661-9, 2011.
- [90] M. Akcakaya, T. A. Basha, S. Pflugli, M. Foppa, K. V. Kissinger, T. H. Hauser, *et al.*, "Localized spatio-temporal constraints for accelerated CMR perfusion," *Magn Reson Med*, vol. 72, pp. 629-39, 2014.
- [91] G. Adluru and E. V. DiBella, "Reordering for improved constrained reconstruction from undersampled k-space data," *Int J Biomed Imaging*, vol. 2008, p. 341684, 2008.
- [92] P. Lai, M. Lustig, A. C. Brau, and S. Vasanawala, "kt SPIRiT for Ultra-Fast Cardiac Cine Imaging with Prospective or Retrospective Cardiac Gating," *Proceedings of the 18th Annual Meeting of ISMRM*, Stockholm, Sweden, 2010.
- [93] S. G. Lingala, Y. Hu, E. DiBella, and M. Jacob, "Accelerated dynamic MRI exploiting sparsity and low-rank structure: k-t SLR," *IEEE Trans Med Imaging*, vol. 30, pp. 1042-54, 2011.
- [94] R. Otazo, E. Candes, and D. K. Sodickson, "Low-rank plus sparse matrix decomposition for accelerated dynamic MRI with separation of background and dynamic components," *Magn Reson Med*, vol. 73, pp. 1125-36, 2015.
- [95] T. Zhang, J. M. Pauly, and I. R. Levesque, "Accelerating parameter mapping with a locally low rank constraint," *Magn Reson Med*, vol. 73, pp. 655-61, 2015.
- [96] M. Usman, C. Prieto, T. Schaeffter, and P. G. Batchelor, "k-t Group sparse: a method for accelerating dynamic MRI," *Magn Reson Med*, vol. 66, pp. 1163-76, 2011.
- [97] J. Caballero, A. N. Price, D. Rueckert, and J. V. Hajnal, "Dictionary Learning and Time Sparsity for Dynamic MR Data Reconstruction," *IEEE Transactions on Medical Imaging*, vol. 33, pp. 979-994, 2014.

- [98] M. L. Wood and R. M. Henkelman, "MR Image Artifacts from Periodic Motion," *Medical Physics*, vol. 12, pp. 143-151, 1985.
- [99] A. D. Scott, J. Keegan, and D. N. Firmin, "Motion in Cardiovascular MR Imaging," *Radiology*, vol. 250, pp. 331-351, 2009.
- [100] J. A. Feinstein, F. H. Epstein, A. E. Arai, T. K. F. Foo, M. R. Hartley, R. S. Balaban, *et al.*, "Using cardiac phase to order reconstruction [CAPTOR]: A method to improve diastolic images," *JMRI-Journal of Magnetic Resonance Imaging*, vol. 7, pp. 794-798, 1997.
- [101] M. Buehrer, J. Curcic, P. Boesiger, and S. Kozerke, "Prospective self-gating for simultaneous compensation of cardiac and respiratory motion," *Magnetic Resonance in Medicine*, vol. 60, pp. 683-690, 2008.
- [102] Y. Wang, S. J. Riederer, and R. L. Ehman, "Respiratory motion of the heart: kinematics and the implications for the spatial resolution in coronary imaging," *Magn Reson Med*, vol. 33, pp. 713-9, 1995.
- [103] C. Plathow, S. Ley, J. Zaporozhan, M. Schobinger, E. Gruenig, M. Puderbach, *et al.*, "Assessment of reproducibility and stability of different breath-hold maneuvers by dynamic MRI: comparison between healthy adults and patients with pulmonary hypertension," *Eur Radiol*, vol. 16, pp. 173-9, 2006.
- [104] M. Weiger, P. Bornert, R. Proksa, T. Schaffter, and A. Haase, "Motion-adapted gating based on k-space weighting for reduction of respiratory motion artifacts," *Magnetic Resonance in Medicine*, vol. 38, pp. 322-333, 1997.
- [105] P. Jhooti, F. Wiesmann, A. M. Taylor, P. D. Gatehouse, G. Z. Yang, J. Keegan, *et al.*, "Hybrid ordered phase encoding (HOPE): An improved approach for respiratory artifact reduction," *JMRI-Journal of Magnetic Resonance Imaging*, vol. 8, pp. 968-980, 1998.
- [106] M. Stuber, R. M. Botnar, S. E. Fischer, R. Lamerichs, J. Smink, P. Harvey, *et al.*, "Preliminary report on in vivo coronary MRA at 3 Tesla in humans," *Magn Reson Med*, vol. 48, pp. 425-9, 2002.
- [107] R. L. Ehman, M. T. McNamara, M. Pallack, H. Hricak, and C. B. Higgins, "Magnetic resonance imaging with respiratory gating: techniques and advantages," *AJR Am J Roentgenol*, vol. 143, pp. 1175-82, 1984.
- [108] B. Madore, G. Farneback, C. F. Westin, and A. Duran-Mendicuti, "A new strategy for respiration compensation, applied toward 3D free-breathing cardiac MRI," *Magn Reson Imaging*, vol. 24, pp. 727-37, 2006.
- [109] C. Santelli, R. Nezafat, B. Goddu, W. J. Manning, J. Smink, S. Kozerke, *et al.*, "Respiratory bellows revisited for motion compensation: preliminary experience for cardiovascular MR," *Magn Reson Med*, vol. 65, pp. 1097-102, 2011.
- [110] S. Uribe, V. Muthurangu, R. Boubertakh, T. Schaeffter, R. Razavi, D. L. G. Hill, *et al.*, "Whole-heart cine MRI using real-time respiratory self-gating," *Magnetic Resonance in Medicine*, vol. 57, pp. 606-613, 2007.
- [111] P. G. Danias, M. Stuber, R. M. Botnar, K. V. Kissinger, R. R. Edelman, and W. J. Manning, "Relationship between motion of coronary arteries and diaphragm during free breathing: Lessons from real-time MR imaging," *American Journal of Roentgenology*, vol. 172, pp. 1061-1065, 1999.
- [112] K. Nehrke, P. Bornert, D. Manke, and J. C. Bock, "Free-breathing cardiac MR imaging: Study of implications of respiratory motion-initial results," *Radiology*, vol. 220, pp. 810-815, 2001.
- [113] D. Manke, K. Nehrke, and P. Bornert, "Novel prospective respiratory motion correction approach for free-breathing coronary MR angiography using a patient-adapted affine motion model," *Magn Reson Med*, vol. 50, pp. 122-31, 2003.
- [114] M. Henningson, J. Smink, R. Razavi, and R. M. Botnar, "Prospective respiratory motion correction for coronary MR angiography using a 2D image navigator," *Magn Reson Med*, vol. 69, pp. 486-94, 2013.
- [115] K. Nehrke and P. Bornert, "Prospective correction of affine motion for arbitrary MR sequences on a clinical scanner," *Magn Reson Med*, vol. 54, pp. 1130-8, 2005.

- [116] C. Stehning, P. Bornert, K. Nehrke, H. Eggers, and M. Stuber, "Free-breathing whole-heart coronary MRA with 3D radial SSFP and self-navigated image reconstruction," *Magnetic Resonance in Medicine*, vol. 54, pp. 476-480, 2005.
- [117] G. Vaillant, C. Prieto, C. Kolbitsch, G. Penney, and T. Schaeffter, "Retrospective Rigid Motion Correction in k-Space for Segmented Radial MRI," *IEEE Transactions on Medical Imaging*, vol. 33, pp. 1-10, 2014.
- [118] M. H. Moghari, S. Roujol, M. Henningsson, K. V. Kissinger, D. Annese, R. Nezafat, *et al.*, "Three-dimensional heart locator for whole-heart coronary magnetic resonance angiography," *Magn Reson Med*, vol. 71, pp. 2118-26, 2014.
- [119] J. G. Pipe, "Motion correction with PROPELLER MRI: application to head motion and free-breathing cardiac imaging," *Magn Reson Med*, vol. 42, pp. 963-9, 1999.
- [120] M. S. Hansen, T. S. Sorensen, A. E. Arai, and P. Kellman, "Retrospective reconstruction of high temporal resolution cine images from real-time MRI using iterative motion correction," *Magnetic Resonance in Medicine*, vol. 68, pp. 741-750, 2012.
- [121] C. Buerger, C. Prieto, and T. Schaeffter, "Highly efficient 3D motion-compensated abdomen MRI from undersampled golden-RPE acquisitions," *Magnetic Resonance Materials in Physics Biology and Medicine*, vol. 26, pp. 419-429, 2013.
- [122] C. Prieto, M. Doneva, M. Usman, M. Henningsson, G. Greil, T. Schaeffter, *et al.*, "Highly efficient respiratory motion compensated free-breathing coronary MRA using golden-step Cartesian acquisition," *J Magn Reson Imaging*, vol. 41, pp. 738-46, 2015.
- [123] M. Henningsson, C. Prieto, A. Chiribiri, G. Vaillant, R. Razavi, and R. M. Botnar, "Whole-Heart Coronary MRA with 3D Affine Motion Correction Using 3D Image-Based Navigation," *Magnetic Resonance in Medicine*, vol. 71, pp. 173-181, 2014.
- [124] P. Hu, S. Hong, M. H. Moghari, B. Goddu, L. Goepfert, K. V. Kissinger, *et al.*, "Motion Correction Using Coil Arrays (MOCCA) for Free-Breathing Cardiac Cine MRI," *Magnetic Resonance in Medicine*, vol. 66, pp. 467-475, 2011.
- [125] C. Buerger, T. Schaeffter, and A. P. King, "Hierarchical adaptive local affine registration for fast and robust respiratory motion estimation," *Medical Image Analysis*, vol. 15, pp. 551-564, 2011.
- [126] G. Vaillant, C. Buerger, G. Penney, C. Prieto, and T. Schaeffter, "Multiple-region affine motion correction using localized coil sensitivities," *Proceedings of the 19th Annual Meeting of ISMRM*, Montréal, Canada, 2011.
- [127] J. Y. Cheng, M. T. Alley, C. H. Cunningham, S. S. Vasanawala, J. M. Pauly, and M. Lustig, "Nonrigid motion correction in 3D using autofocusing with localized linear translations," *Magn Reson Med*, vol. 68, pp. 1785-97, 2012.
- [128] P. G. Batchelor, D. Atkinson, P. Irarrazaval, D. L. Hill, J. Hajnal, and D. Larkman, "Matrix description of general motion correction applied to multishot images," *Magn Reson Med*, vol. 54, pp. 1273-80, 2005.
- [129] F. Odille, N. Cindea, D. Mandry, C. Pasquier, P. A. Vuissoz, and J. Felblinger, "Generalized MRI reconstruction including elastic physiological motion and coil sensitivity encoding," *Magn Reson Med*, vol. 59, pp. 1401-11, 2008.
- [130] F. Odille, P. A. Vuissoz, P. Y. Marie, and J. Felblinger, "Generalized reconstruction by inversion of coupled systems (GRICS) applied to free-breathing MRI," *Magn Reson Med*, vol. 60, pp. 146-57, 2008.
- [131] J. F. Schmidt, M. Buehrer, P. Boesiger, and S. Kozerke, "Nonrigid retrospective respiratory motion correction in whole-heart coronary MRA," *Magn Reson Med*, vol. 66, pp. 1541-9, 2011.
- [132] J. F. M. Schmidt, L. Wissmann, R. Manka, and S. Kozerke, "Iterative k-t Principal Component Analysis with Nonrigid Motion Correction for Dynamic Three-Dimensional Cardiac Perfusion Imaging," *Magnetic Resonance in Medicine*, vol. 72, pp. 68-79, 2014.
- [133] D. K. Sodickson and W. J. Manning, "Simultaneous acquisition of spatial harmonics (SMASH): fast imaging with radiofrequency coil arrays," *Magn Reson Med*, vol. 38, pp. 591-603, 1997.

- [134] P. M. Jakob, M. A. Griswold, R. R. Edelman, and D. K. Sodickson, "AUTO-SMASH: a self-calibrating technique for SMASH imaging. SiMultaneous Acquisition of Spatial Harmonics," *MAGMA*, vol. 7, pp. 42-54, 1998.
- [135] W. E. Kyriakos, L. P. Panych, D. F. Kacher, C. F. Westin, S. M. Bao, R. V. Mulkern, *et al.*, "Sensitivity profiles from an array of coils for encoding and reconstruction in parallel (SPACE RIP)," *Magn Reson Med*, vol. 44, pp. 301-8, 2000.
- [136] M. A. Griswold, P. M. Jakob, M. Nittka, J. W. Goldfarb, and A. Haase, "Partially parallel imaging with localized sensitivities (PILS)," *Magn Reson Med*, vol. 44, pp. 602-9, 2000.
- [137] R. M. Heidemann, M. A. Griswold, A. Haase, and P. M. Jakob, "VD-AUTO-SMASH imaging," *Magn Reson Med*, vol. 45, pp. 1066-74, 2001.
- [138] E. N. Yeh, C. A. McKenzie, M. A. Ohliger, and D. K. Sodickson, "Parallel magnetic resonance imaging with adaptive radius in k-space (PARS): constrained image reconstruction using k-space locality in radiofrequency coil encoded data," *Magn Reson Med*, vol. 53, pp. 1383-92, 2005.
- [139] C. Liu, R. Bammer, and M. E. Moseley, "Parallel imaging reconstruction for arbitrary trajectories using k-space sparse matrices (kSPA)," *Magn Reson Med*, vol. 58, pp. 1171-81, 2007.
- [140] K. Heberlein and X. Hu, "Auto-calibrated parallel spiral imaging," *Magn Reson Med*, vol. 55, pp. 619-25, 2006.
- [141] N. Seiberlich, F. Breuer, R. Heidemann, M. Blaimer, M. Griswold, and P. Jakob, "Reconstruction of undersampled non-Cartesian data sets using pseudo-Cartesian GRAPPA in conjunction with GROG," *Magn Reson Med*, vol. 59, pp. 1127-37, 2008.
- [142] P. Kellman, F. H. Epstein, and E. R. McVeigh, "Adaptive sensitivity encoding incorporating temporal filtering (TSENSE)," *Magn Reson Med*, vol. 45, pp. 846-52, 2001.
- [143] F. A. Breuer, P. Kellman, M. A. Griswold, and P. M. Jakob, "Dynamic autocalibrated parallel imaging using temporal GRAPPA (TGRAPPA)," *Magn Reson Med*, vol. 53, pp. 981-5, 2005.
- [144] M. Blaimer, I. P. Ponce, F. A. Breuer, P. M. Jakob, M. A. Griswold, and P. Kellman, "Temporal filtering effects in dynamic parallel MRI," *Magn Reson Med*, vol. 66, pp. 192-8, 2011.
- [145] M. Lustig, M. Elad, and J. M. Pauly, "Calibrationless Parallel Imaging Reconstruction by Structured Low-Rank Matrix Completion," *Proceedings of the 18th Annual Meeting of ISMRM*, Stockholm, Sweden, 2010.
- [146] M. Lustig, "Post-Cartesian Calibrationless Parallel Imaging Reconstruction by Structured Low-Rank Matrix Completion," *Proceedings of the 19th Annual Meeting of ISMRM*, Montréal, Canada, 2011.
- [147] P. Beerbaum, H. Korperich, J. Gieseke, P. Barth, M. Peuster, and H. Meyer, "Rapid left-to-right shunt quantification in children by phase-contrast magnetic resonance imaging combined with sensitivity encoding (SENSE)," *Circulation*, vol. 108, pp. 1355-61, 2003.
- [148] T. Gu, F. R. Korosec, W. F. Block, S. B. Fain, Q. Turk, D. Lum, *et al.*, "PC VIPR: a high-speed 3D phase-contrast method for flow quantification and high-resolution angiography," *AJNR Am J Neuroradiol*, vol. 26, pp. 743-9, 2005.
- [149] B. Jung, M. Honal, P. Ullmann, J. Hennig, and M. Markl, "Highly k-t-space-accelerated phase-contrast MRI," *Magn Reson Med*, vol. 60, pp. 1169-77, 2008.
- [150] J. V. Velikina, K. M. Johnson, Y. Wu, A. A. Samsonov, P. Turski, and C. A. Mistretta, "PC HYPR flow: a technique for rapid imaging of contrast dynamics," *J Magn Reson Imaging*, vol. 31, pp. 447-56, 2010.
- [151] D. J. Holland, D. M. Malioutov, A. Blake, A. J. Sederman, and L. F. Gladden, "Reducing data acquisition times in phase-encoded velocity imaging using compressed sensing," *J Magn Reson*, vol. 203, pp. 236-46, 2010.
- [152] B. Jung, A. F. Stalder, S. Bauer, and M. Markl, "On the undersampling strategies to accelerate time-resolved 3D imaging using k-t-GRAPPA," *Magn Reson Med*, vol. 66, pp. 966-75, 2011.

- [153] A. Sigfridsson, S. Petersson, C. J. Carlhall, and T. Ebbers, "Four-dimensional flow MRI using spiral acquisition," *Magn Reson Med*, vol. 68, pp. 1065-73, 2012.
- [154] D. Giese, T. Schaeffter, and S. Kozerke, "Highly undersampled phase-contrast flow measurements using compartment-based k-t principal component analysis," *Magn Reson Med*, vol. 69, pp. 434-43, 2013.
- [155] V. Knobloch, P. Boesiger, and S. Kozerke, "Sparsity transform k-t principal component analysis for accelerating cine three-dimensional flow measurements," *Magn Reson Med*, vol. 70, pp. 53-63, 2013.
- [156] Y. Kwak, S. Nam, M. Akcakaya, T. A. Basha, B. Goddu, W. J. Manning, *et al.*, "Accelerated aortic flow assessment with compressed sensing with and without use of the sparsity of the complex difference image," *Magn Reson Med*, vol. 70, pp. 851-8, 2013.
- [157] J. P. Hulet, A. Greiser, J. K. Mendes, C. McGann, G. Treiman, and D. L. Parker, "Highly accelerated cardiac cine phase-contrast MRI using an undersampled radial acquisition and temporally constrained reconstruction," *J Magn Reson Imaging*, vol. 39, pp. 455-62, 2014.
- [158] R. H. Mohiaddin, P. D. Gatehouse, M. Henien, and D. N. Firmin, "Cine MR Fourier velocimetry of blood flow through cardiac valves: comparison with Doppler echocardiography," *J Magn Reson Imaging*, vol. 7, pp. 657-63, 1997.
- [159] P. Dyverfeldt, R. Gardhagen, A. Sigfridsson, M. Karlsson, and T. Ebbers, "On MRI turbulence quantification," *Magn Reson Imaging*, vol. 27, pp. 913-22, 2009.
- [160] C. Binter, V. Knobloch, R. Manka, A. Sigfridsson, and S. Kozerke, "Bayesian multipoint velocity encoding for concurrent flow and turbulence mapping," *Magn Reson Med*, vol. 69, pp. 1337-45, 2013.
- [161] P. R. Johnston and R. M. Gulrajani, "Selecting the corner in the L-curve approach to Tikhonov regularization," *IEEE Trans Biomed Eng*, vol. 47, pp. 1293-6, 2000.
- [162] M. A. Bernstein, M. Grgic, T. J. Brosnan, and N. J. Pelc, "Reconstructions of phase contrast, phased array multicoil data," *Magn Reson Med*, vol. 32, pp. 330-4, 1994.
- [163] P. Dyverfeldt, J. P. Kvitting, A. Sigfridsson, J. Engvall, A. F. Bolger, and T. Ebbers, "Assessment of fluctuating velocities in disturbed cardiovascular blood flow: in vivo feasibility of generalized phase-contrast MRI," *J Magn Reson Imaging*, vol. 28, pp. 655-63, 2008.
- [164] A. T. Lee, G. B. Pike, and N. J. Pelc, "Three-point phase-contrast velocity measurements with increased velocity-to-noise ratio," *Magn Reson Med*, vol. 33, pp. 122-6, 1995.
- [165] M. Murphy, M. Alley, J. Demmel, K. Keutzer, S. Vasanawala, and M. Lustig, "Fast l(1)-SPIRiT compressed sensing parallel imaging MRI: scalable parallel implementation and clinically feasible runtime," *IEEE Trans Med Imaging*, vol. 31, pp. 1250-62, 2012.
- [166] M. Markl, P. J. Kilner, and T. Ebbers, "Comprehensive 4D velocity mapping of the heart and great vessels by cardiovascular magnetic resonance," *J Cardiovasc Magn Reson*, vol. 13:7, 2011.
- [167] N. J. Pelc, R. J. Herfkens, A. Shimakawa, and D. R. Enzmann, "Phase contrast cine magnetic resonance imaging," *Magn Reson Q*, vol. 7, pp. 229-54, 1991.
- [168] P. J. Kilner, P. D. Gatehouse, and D. N. Firmin, "Flow measurement by magnetic resonance: a unique asset worth optimising," *J Cardiovasc Magn Reson*, vol. 9, pp. 723-8, 2007.
- [169] Z. P. Liang, "Spatiotemporal imaging with partially separable functions," *IEEE International Symposium on Biomedical Imaging : Macro to Nano, Vols 1-3*, pp. 988-991, 2007.
- [170] A. V. Barger, W. F. Block, Y. Toropov, T. M. Grist, and C. A. Mistretta, "Time-resolved contrast-enhanced imaging with isotropic resolution and broad coverage using an undersampled 3D projection trajectory," *Magn Reson Med*, vol. 48, pp. 297-305, 2002.
- [171] C. A. Mistretta, O. Wieben, J. Velikina, W. Block, J. Perry, Y. Wu, *et al.*, "Highly constrained backprojection for time-resolved MRI," *Magn Reson Med*, vol. 55, pp. 30-40, 2006.

- [172] U. Tariq, A. Hsiao, M. Alley, T. Zhang, M. Lustig, and S. S. Vasanawala, "Venous and arterial flow quantification are equally accurate and precise with parallel imaging compressed sensing 4D phase contrast MRI," *J Magn Reson Imaging*, vol. 37, pp. 1419-26, 2013.
- [173] S. M. Song, S. Napel, G. H. Glover, and N. J. Pelc, "Noise reduction in three-dimensional phase-contrast MR velocity measurements," *J Magn Reson Imaging*, vol. 3, pp. 587-96, 1993.
- [174] N. Fatouraee and A. A. Amini, "Regularization of flow streamlines in multislice phase-contrast MR imaging," *IEEE Trans Med Imaging*, vol. 22, pp. 699-709, 2003.
- [175] O. Skrinjar, A. Bistoquet, J. Oshinski, K. Sundareswaran, D. Frakes, and A. Yoganathan, "A divergence-free vector field model for imaging applications," *IEEE International Symposium on Biomedical Imaging: From Nano to Macro*, Boston, USA, 2009.
- [176] P. D. Tafti, R. Delgado-Gonzalo, A. F. Stalder, and M. Unser, "Variational enhancement and denoising of flow field images," *IEEE International Symposium on Biomedical Imaging: From Nano to Macro*, Chicago, USA, 2011.
- [177] J. Busch, D. Giese, L. Wissmann, and S. Kozerke, "Reconstruction of divergence-free velocity fields from cine 3D phase-contrast flow measurements," *Magn Reson Med*, vol. 69, pp. 200-10, 2013.
- [178] M. Loecher, S. Kecskemeti, K. M. Johnson, P. Turski, and O. Wieben, "Evaluation of divergence-free correction algorithms in high resolution 4-D flow images of cranial vasculature," *Proceedings of the 20th Annual Meeting of ISMRM*, Melbourne, Australia, 2012.
- [179] E. Deriaz and V. Perrier, "Divergence-free and curl-free wavelets in two dimensions and three dimensions: application to turbulent flows," *Journal of Turbulence*, vol. 7, pp. 1-37, 2006.
- [180] F. Ong, M. Uecker, U. Tariq, A. Hsiao, M. T. Alley, S. S. Vasanawala, *et al.*, "Robust 4D flow denoising using divergence-free wavelet transform," *Magn Reson Med*, vol. 73, pp. 828-42, 2015.
- [181] F. Zhao, D. C. Noll, J. F. Nielsen, and J. A. Fessler, "Separate magnitude and phase regularization via compressed sensing," *IEEE Trans Med Imaging*, vol. 31, pp. 1713-23, 2012.
- [182] M. Loecher, C. Santelli, O. Wieben, and S. Kozerke, "Improved L1-SPIRiT Reconstruction with a Phase Divergence Penalty for 3D Phase-Contrast Flow Measurements," *Proceedings of the 21st Annual Meeting of ISMRM*, Salt Lake City, Utah, USA, 2013.
- [183] F. Ong, M. Uecker, T. Umar, A. Hsiao, M. Alley, S. Vasanawala, *et al.*, "Compressed Sensing 4D Flow Reconstruction using Divergence-Free Wavelet Transform," *Proceedings of the 22nd Annual Meeting of ISMRM*, Milan, Italy, 2014.
- [184] S. Ramani and J. A. Fessler, "Parallel MR image reconstruction using augmented Lagrangian methods," *IEEE Trans Med Imaging*, vol. 30, pp. 694-706, 2011.
- [185] A. A. Samsonov, E. G. Kholmovski, D. L. Parker, and C. R. Johnson, "POCSENSE: POCS-based reconstruction for sensitivity encoded magnetic resonance imaging," *Magnetic Resonance in Medicine*, vol. 52, pp. 1397-1406, 2004.
- [186] F. T. A. W. Wajer and K. P. Pruessmann, "Major Speedup of Reconstruction for Sensitivity Encoding with Arbitrary Trajectories," *Proceedings of the 9th Annual Meeting of ISMRM*, Glasgow, Scotland, 2001.
- [187] M. Akcakaya, S. Nam, T. A. Basha, K. Kawaji, V. Tarokh, and R. Nezafat, "An augmented Lagrangian based compressed sensing reconstruction for non-Cartesian magnetic resonance imaging without gridding and regridding at every iteration," *PLoS One*, vol. 9, p. e107107, 2014.
- [188] M. Buehrer, K. P. Pruessmann, P. Boesiger, and S. Kozerke, "Array compression for MRI with large coil arrays," *Magn Reson Med*, vol. 57, pp. 1131-9, 2007.
- [189] P. J. Shin, P. E. Larson, M. A. Ohliger, M. Elad, J. M. Pauly, D. B. Vigneron, *et al.*, "Calibrationless parallel imaging reconstruction based on structured low-rank matrix completion," *Magn Reson Med*, vol. 72, pp. 959-70, 2014.

- [190] L. Wissmann, C. Santelli, W. P. Segars, and S. Kozerke, "MRXCAT: Realistic numerical phantoms for cardiovascular magnetic resonance," *J Cardiovasc Magn Reson*, vol. 16:63, 2014.
- [191] S. Klein, M. Staring, K. Murphy, M. A. Viergever, and J. P. W. Pluim, "elastix: A Toolbox for Intensity-Based Medical Image Registration," *IEEE Transactions on Medical Imaging*, vol. 29, pp. 196-205, 2010.
- [192] J. Hutter, R. Grimm, C. Forman, J. Hornegger, and P. Schmitt, "Inverse root sampling pattern for iterative reconstruction in non-CE MR angiography," *Proceedings of the Annual Scientific Meeting of ESMRMB*, Leipzig, Germany, 2011.
- [193] K. Sung and B. A. Hargreaves, "High-Frequency Subband Compressed Sensing MRI Using Quadruplet Sampling," *Magnetic Resonance in Medicine*, vol. 70, pp. 1306-1318, 2013.
- [194] B. Madore, G. H. Glover, and N. J. Pelc, "Unaliasing by fourier-encoding the overlaps using the temporal dimension (UNFOLD), applied to cardiac imaging and fMRI," *Magn Reson Med*, vol. 42, pp. 813-28, 1999.
- [195] D. S. Weller, S. Ramani, and J. A. Fessler, "Augmented Lagrangian with variable splitting for faster non-Cartesian L1-SPIRiT MR image reconstruction," *IEEE Trans Med Imaging*, vol. 33, pp. 351-61, 2014.
- [196] S. Wundrak, J. Paul, J. Ulrici, E. Hell, and V. Rasche, "A Small Surrogate for the Golden Angle in Time-Resolved Radial MRI Based on Generalized Fibonacci Sequences," *IEEE Trans Med Imaging*, doi 10.1109/TMI.2014.2382572, 2014.
- [197] C. Barmet, N. De Zanche, and K. P. Pruessmann, "Spatiotemporal magnetic field monitoring for MR," *Magn Reson Med*, vol. 60, pp. 187-97, 2008.
- [198] A. Goldberg and S. Jha, "Phase-contrast MRI and applications in congenital heart disease," *Clin Radiol*, vol. 67, pp. 399-410, 2012.
- [199] V. Knobloch, C. Binter, V. Kurtcuoglu, and S. Kozerke, "Arterial, venous, and cerebrospinal fluid flow: simultaneous assessment with Bayesian multipoint velocity-encoded MR imaging," *Radiology*, vol. 270, pp. 566-73, 2014.
- [200] S. Nordmeyer, E. Riesenkampff, G. Crelier, A. Khasheei, B. Schnackenburg, F. Berger, *et al.*, "Flow-sensitive four-dimensional cine magnetic resonance imaging for offline blood flow quantification in multiple vessels: a validation study," *J Magn Reson Imaging*, vol. 32, pp. 677-83, 2010.
- [201] M. Carlsson, J. Toger, M. Kanski, K. M. Bloch, F. Stahlberg, E. Heiberg, *et al.*, "Quantification and visualization of cardiovascular 4D velocity mapping accelerated with parallel imaging or k-t BLAST: head to head comparison and validation at 1.5 T and 3 T," *J Cardiovasc Magn Reson*, vol. 13:55, 2011.
- [202] A. Stadlbauer, W. van der Riet, G. Crelier, and E. Salomonowitz, "Accelerated time-resolved three-dimensional MR velocity mapping of blood flow patterns in the aorta using SENSE and k-t BLAST," *Eur J Radiol*, vol. 75, pp. e15-21, 2010.
- [203] D. Giese, J. Wong, G. F. Greil, M. Buehrer, T. Schaeffter, and S. Kozerke, "Towards highly accelerated Cartesian time-resolved 3D flow cardiovascular magnetic resonance in the clinical setting," *J Cardiovasc Magn Reson*, vol. 16:42, 2014.
- [204] C. Binter, A. Gotschy, R. Manka, S. H. Suendermann, and S. Kozerke, "Assessment of Aortic Stenosis Severity using Bayesian Multipoint Phase-Contrast MRI," *Proceedings of the 22nd Annual Meeting of ISMRM*, Milan, Italy, 2014.
- [205] C. Binter, U. Gulan, V. Knobloch, M. Holzner, and S. Kozerke, "On the Quantification of Turbulent Kinetic Energy using Phase-Contrast MRI," *Proceeding fo the 22nd Annual Meeting of ISMRM*, Milan, Italy, 2014.
- [206] M. S. Hansen, C. Baltes, J. Tsao, S. Kozerke, K. P. Pruessmann, P. Boesiger, *et al.*, "Accelerated dynamic Fourier velocity encoding by exploiting velocity-spatio-temporal correlations," *MAGMA*, vol. 17, pp. 86-94, 2004.

List of Publications

Journal Articles

- 2015 **C. Santelli**, M. Loecher, J. Busch, O. Wieben, T. Schaeffter and S. Kozerke
“Accelerating 4D Flow MRI by Exploiting Vector Field Divergence Regularization”
Magnetic Resonance in Medicine, DOI 10.1002/mrm.25563.
- 2014 L. Wissmann, **C. Santelli**, W. P. Segars and S. Kozerke
“MRXCAT: Realistic Numerical Phantoms for Cardiovascular Magnetic Resonance”
Journal of Cardiovascular Magnetic Resonance, vol. 16:63.
- 2014 **C. Santelli**, T. Schaeffter and S. Kozerke
“Radial k-t SPIRiT: Autocalibrated Parallel Imaging for Generalized Phase-Contrast MRI”
Magnetic Resonance in Medicine, vol. 72(5), pp. 1233-1245.
- 2011 **C. Santelli**, R. Nezafat, B. Goddu, W. J. Manning, J. Smink, S. Kozerke and D. C. Peters
“Respiratory Bellows Revisited for Motion Compensation: Preliminary Experience for Cardiovascular MR”
Magnetic Resonance in Medicine, vol. 65(4), pp. 1097-1102.
- 2009 R. Banz, M. Bolliger, S. Müller, **C. Santelli** and R. Riener
“A Method of Estimating the Degree of Active Participation During Stepping in a Driven Gait Orthosis Based on Actuator Force Profile Matching”
IEEE Transactions on Neural Systems and Rehabilitation Engineering, vol. 17(1), pp. 15-22.

Conference Abstracts and Proceedings

- 2015 **C. Santelli**, M. Loecher, J. Busch, O. Wieben, T. Schaeffter and S. Kozerke
“Accelerating Flow Encoded MRI by Exploiting Vector Field Divergence Regularization”
Proceedings of the 23rd Meeting of ISMRM, Toronto, ON, Canada, accepted for e-poster presentation.
- 2014 J. F. M. Schmidt*, **C. Santelli*** and S. Kozerke
“Optimized k-t Sampling for Combined Parallel Imaging and Compressed Sensing Reconstruction”
Proceedings of the 22nd Meeting of ISMRM, Milan, Italy, e-poster presentation, p. 4377 (* denotes shared first authorship)
- 2013 **C. Santelli**, T. Schaeffter and S. Kozerke
“SPIRiT^{mc} – Autocalibrating Parallel Imaging with Non-Rigid Motion Correction”
Proceedings of the 21st Meeting of ISMRM, Salt Lake City, UT, USA, e-poster presentation, p. 3748.
- 2013 **C. Santelli**, T. Schaeffter and S. Kozerke
“Efficient Non-Cartesian SPIRiT without Explicit Consecutive Re-gridding and Gridding”
Proceedings of the 21st Meeting of ISMRM, Salt Lake City, UT, USA, poster presentation, p. 2643.
- 2013 M. Loecher, **C. Santelli**, O. Wieben and S. Kozerke
“Improved L1-SPIRiT Reconstruction with a Phase Divergence Penalty for 3D Phase-Contrast Flow Measurements”
Proceedings of the 21st Meeting of ISMRM, Salt Lake City, UT, USA, poster presentation, p. 1355.
- 2013 **C. Santelli**, T. Schaeffter and S. Kozerke
“SPIRiT^{mc} – Autocalibrating Parallel Imaging with Non-Rigid Motion Correction”
ISMRM Workshop on Data Sampling & Image Reconstruction, Sedona, AZ, USA, oral presentation.
Awarded with 2nd place in young presenter category.
- 2013 N. Arvanitopoulos, **C. Santelli**, Matthias Seeger and S. Kozerke
“Divergence-Free Phase-Contrast MRI”
Proceedings of the International Workshop on Biomedical and Astronomical Signal Processing (BASP) Frontiers, Villars-sur-Ollon, VD, Switzerland, oral presentation, p. 53.

- 2012 **C. Santelli**, T. Schaeffter and S. Kozerke
"Radial Fourier Velocity Encoding (rFVE) with SPIRiT Exploiting Temporal Correlations in k-t Space"
 Proceedings of the 20th Meeting of ISMRM, Melbourne, Australia, oral presentation, p. 670.
 Summa cum laude ISMRM merit award.
- 2012 **C. Santelli**, T. Schaeffter and S. Kozerke
"On Compressed Sensing for Phase-Contrast Velocity Mapping"
 Proceedings of the 20th Meeting of ISMRM, Melbourne, Australia, e-poster presentation, p. 4204.
- 2012 **C. Santelli**, T. Schaeffter and S. Kozerke
"Velocity Spectrum Imaging Using Radial k-t SPIRiT"
 SCMR/ISMRM Workshop on Exploring New Dimensions of Cardiovascular Flow & Motion, Orlando, FL, USA, poster presentation.
- 2011 **C. Santelli** and S. Kozerke
"Performance of L1-Norm Minimizing Regularizers on Phase/Magnitude Reconstruction in Flow Encoded MRI"
 International Workshop on Biomedical and Astronomical Signal Processing (BASP) Frontiers, Villars-sur-Ollon, VD, Switzerland, oral presentation.
- 2011 **C. Santelli** and S. Kozerke
"Dynamic Radial Fourier Velocity Encoding (rFVE) with Autocalibrating Parallel Imaging exploiting Temporal Correlations in k-t Space (k-t rFVE)"
 Book of Abstracts ESMRMB Congress, Leipzig, Germany, oral presentation, p. 246.
- 2010 **C. Santelli**, R. Nezafat, W. J. Manning, S. Kozerke and D. C. Peters
"Retrospective Bellows-Based Reconstruction for Cardiac MRI: Preliminary Experience"
 Proceedings of the 18th Meeting of ISMRM, Stockholm, Sweden, e-poster presentation, p. 5012.

Curriculum Vitae

Personal Information

Name	Claudio Santelli
Date of birth	7 February 1983
Citizenship	Swiss

Education

Oct 2010 – Jan 2015	Ph.D. Candidate <i>Thesis “Accelerating Multi-Dimensional Magnetic Resonance Imaging of Blood Flow and Turbulence in the Cardiovascular System” supervised by Prof. Sebastian Kozerke.</i> Division of Imaging Sciences and Biomedical Engineering, School of Medicine, King’s College London, UK (jointly with the Institute for Biomedical Engineering (IBT), Swiss Federal Institute of Technology (ETH Zurich) and University of Zurich, CH)
Oct 2002 – Jun 2009	M.Sc. in Electrical and Information Technology <i>Master thesis “Solving Crossing Fibers with Advanced Diffusion-Weighted Imaging Techniques” supervised by Carolin Reischauer and Robert Vorburger.</i> IBT, Department of Information Technology and Electrical Engineering (D-ITET), ETH Zurich, CH
Aug 1997 – Jan 2002	Matura, Typus E (High School Degree in Economics and Law) Kantonsschule Enge, Zurich, CH

Work and Research Experience

- Sept 2009 – Feb 2010 **Beth Israel Deaconess Medical Center (BIDMC), Cardiovascular MR Center, Harvard Medical School, Boston, MA, USA**
Research assistant in the field of motion compensation techniques for cardiac MRI.
- Nov 2007 – May 2008 **Varian Medical Systems, Imaging Laboratory GmbH, Baden-Dättwil, AG, CH**
Internship: development of a software tool for automated quality assessment of digital X-ray images.
- May 2007 **Hocoma AG, Volketswil, ZH, CH**
Evaluation of signal processing methods for Hocoma's robotic gait orthosis "Lokomat".
- 2002 - 2010 **Private, Zurich, CH**
Private teaching in Mathematics up to high school level.